

THEORY AND APPLICATION OF MICROWAVE JOINING

By

ALEX DOUGLAS COZZI

A DISSERTATION PRESENTED TO THE GRADUATE SCHOOL OF THE
UNIVERSITY OF FLORIDA IN PARTIAL FULFILLMENT OF THE REQUIREMENTS
FOR THE DEGREE OF DOCTOR OF PHILOSOPHY

UNIVERSITY OF FLORIDA

1996

UNIVERSITY OF FLORIDA LIBRARIES

Copyright 1996

by

Alex Douglas Cozzi

I would like to dedicate this dissertation to my father, Thomas. My only regret is that you could not see me graduate.

ACKNOWLEDGEMENTS

The author would like to thank a number of people for their professional suggestions and personal support towards this study. First I would like to thank Dr. David Clark who not only showed me how to be a better scientist, but how to be a better person. His guidance and constant reassurance allowed me to complete the graduate program. I would like to express special thanks to Dr. Matt Ferber of Oak Ridge National Labs for taking the time to provide assistance and guidance even though he is extremely busy with many other projects.

I would like to also thank Drs. J.J. Mecholsky, B.V. Sankar, R.J. Singh, E. D. Whitney and V.J. Tennery for their comments and suggestions that increased the technical value of this study. I wish to thank Dr. Ron Hutcheon of the Atomic Energy of Canada Ltd., Chalk River Laboratories for providing essential dielectric data and insight into the meaning of that data.

The author appreciates the assistance of the administrative and technical staff of the High Temperature Materials Laboratory at Oak Ridge National Labs, especially Arvid Pasto and Billie Russell, the ringleaders of the HTML Fellowship program. I would like to thank the members of Dr. Ferber's research group, Kristin Breder, Jason Canon, Dana Green, Allen Haynes, Tim Kirkland, Edgar Lara-Curzio, Ron Ott, Laura Riester and Andy Wereszczak. I would like to also thank Mark Janney and Jim Kiggans for providing me with all the materials and assistance they could spare.

I would like to convey special thanks to Diane Folz and Rebecca Lynn Shulz for both their professional help and friendship throughout my stay at the University of Florida. I would like to also thank all of the past and present members in Dr. Clark's research

group, my peers in the Department of Materials Science and Engineering, Iftikhar Ahmad, Salwan Al-Assafi, Attapon Boonyapiwat, Robert Dalton, Arindam Dé, Robert DiFiore, Zak Fathi, Carl Jones, Don Jones, Michelle Lococo, Edmund Moore, Lorie Stapler and Bruce Zito. I would like to convey special thanks to my friends, especially Philip McCluskey, Andrew Duncan, Mark Weaver, Chris O'Gara, Lisa Demmy and George Demmy.

I would like to express particular thanks to my family, my parent's Thomas and Lillian, my sister Dianne, my brothers Tommy and Alan as well as their families for their emotional and financial support through eight long years of graduate school. Finally, I would like to acknowledge my wife, Sunday, who along with my family believed in me when even I wasn't so sure. She watched me through the highs and lows of this study, tried tirelessly to keep me focused on the goal and provided love and support without which this study could not have been performed.

This research was sponsored by the Assistant Secretary for Energy Efficiency and Renewable Energy, Office of Transportation Technologies, as part of the High Temperature Materials Laboratory Fellowship Program, Oak Ridge National Laboratory, managed by Lockheed Martin Energy Research Corp. for the U.S. Department of Energy under contract number DE-AC05-96OR22464.

TABLE OF CONTENTS

ACKNOWLEDGEMENTS	iv
LIST OF TABLES	ix
LIST OF FIGURES	xi
ABSTRACT	xix
CHAPTERS	
1 INTRODUCTION	1
2 SURVEY OF THE LITERATURE	7
Microwaves	7
Background	7
Microwave Applicators	12
Microwave Processing of Materials	16
Numerical Modeling of Microwave/Material Interactions	17
Evidence of Microwave Enhancements	26
Joining	28
Joining Methods	28
Joining processes	32
Criteria for Joining	35
Effect of Process Variables on Joining	38
Temperature	38
Pressure	41
Time	41
Reactions	44
Scales of Joining	44
Atomic	44
Nano	46
Micro	49
Macro	50
Materials Joining	50
Metal/ceramic joining	51
Ceramic/ceramic	52
Microwave Joining	53
Summary	60
3 MATERIALS AND METHODS	62
Phase One	63

	Sol-Gel	64
	Base gel	64
	Doped gel	65
	Sol-Gel Characterization	68
	Stand alone heating	68
	Differential scanning calorimetry	70
	X-ray diffraction analysis	70
	Dielectric properties	71
	Alumina	71
	Nickel Oxide	72
	Surface roughness	73
	Phase Two	74
	Microwave Joining Apparatus	75
	Microwave Susceptors	77
	Specimen Preparation	86
	Mechanical Testing	87
	Phase Three	90
	Microwave Joining	91
	Conventional Joining	93
	Optical Inspection	93
	Statistical Analysis	94
	Phase Four	95
4	NUMERICAL MODELING	96
	Heat Transfer	97
	Transient Heat Conduction	101
	Boundary Conditions	103
	The Physical Model	105
	Case Title	105
	General Problem Parameters	106
	Region Data	106
	Materials	107
	Initial Temperature	109
	Heat Generation	109
	Boundary Conditions	110
	Grids	112
	Analytical Functions	113
	Specific heat	114
	Thermal conductivity	114
	Power generation	114
	Boundary condition	123
	Tabular Functions	123
	Thermal conductivity	126
	Printout Times	127
	Nodes Monitored	128
	Transient Data	128
5	RESULTS	137
	Machined Surfaces	137
	Sol-Gel Interlayers	137
	Stand Alone Heating	137

	Differential Scanning Calorimetry	143
	X-ray Diffraction Analysis	145
	Dielectric Measurements	147
	Microwave Susceptors	153
	Joining	160
	Joining Conditions	160
	Visual Inspection	160
	Flexure Testing	163
	Statistical Analysis	184
	Numerical Modeling	203
6	DISCUSSION	217
	Phase One	217
	Machined Surfaces	217
	Sol-Gel Interlayers	218
	Summary of Phase One	221
	Phase Two	223
	Microwave Susceptors	223
	Microwave Joining Apparatus	224
	Summary of Phase Two	224
	Phase Three	225
	Experimental Design	225
	Joining Experiments and Flexure Tests	226
	Statistical Analysis	229
	Summary of Phase Three	231
	Phase Four	231
	Computer Simulations	232
	Summary of Phase Four	234
7	SUMMARY AND CONCLUSIONS	235
8	FUTURE WORK	241
APPENDICES		
A	SAMPLE CALCULATIONS OF THE PENETRATION DEPTH AND CRITICAL THICKNESS FOR AI-66 CEMENT	243
B	SUMMARY OF INPUT DATA FOR HEATING 7.2	245
C	SAMPLE CALCULATIONS FOR STATISTICAL ANALYSIS	251
REFERENCES		255
BIOGRAPHICAL SKETCH		263

LIST OF TABLES

Table 2-1.	Error Associated with Simplified Equation for Penetration Depth for Several $\epsilon''_{eff}/\epsilon'$ Ratios.	11
Table 3-1.	Manufacturer Reported Properties of Coors Alumina Used in Study.	72
Table 3-2.	Levels of Varied Processing Conditions.	91
Table 3-3.	Experimental Design used to Aid in Determining the Effect of Processing Conditions on the Strength of the Joint.	92
Table 4-1.	Summary of the Parameter Cards Used to Describe the Nine Model Regions.	108
Table 4-2.	Input Parameters for the Four Materials Represented in the Model. ..	109
Table 4-3.	Heat Generation Cards for the Four Materials in the Model.	110
Table 4-4.	Table of the Gross and Fine Grid Lines for Both the r and z Axes. ..	113
Table 4-5.	Thermal Conductivity of Coors AD995 Alumina at Different Temperatures.	126
Table 4-6.	Thermal Conductivity of the Nickel Oxide Used in the Model at Different Temperatures.	126
Table 4-7.	Calculated Values for the Thermal Conductivity of a 30 wt.% SiC/Cement Susceptor.	127
Table 4-8.	Nodes of Interest and Their Placement in the Model.	130
Table 5-1.	Flexure Strength of AD995 Alumina Joined Under Various Conditions Using Several Different Interlayer Materials.	163
Table 5-2.	Mean Strength and Standard Deviation of Bars Joined by either Microwave or Conventional Heating.	169
Table 5-3.	Data Used to Perform ANOVA Analysis.	192
Table 5-4.	Output of Statistical Analysis of Data from Table 5-3.	193

Table 5-5.	Statistical Analysis of the Effect of Bar Position on the Flexure Strength for both Microwave and Conventional Heating.	199
Table 5-6.	Effect of Position/Heating Method Interaction on the Flexure Strength.	203

LIST OF FIGURES

Figure 1-1.	Schematic depicting the intersection of two fields of modeling to form a basis for research.	5
Figure 2-1.	Representation of the lag in the current that determines the loss tangent.	10
Figure 2-2.	Ratio of transmitted to incident field for aperture diameter, $0.05 < d/\lambda < 1$	15
Figure 2-3.	Radial temperature profiles in a cylindrical roast beef.	20
Figure 2-4.	Temperature of bread heated with two different field strengths.	21
Figure 2-5.	Effect of variable (—) versus constant (---) dielectric properties on temperature in a raw beef sample. Depth in sample refers to fraction of whole.	22
Figure 2-6.	Measured and computed temperatures for the specimen and the insulation during a microwave sintering run.	24
Figure 2-7.	The activation energy for ^{18}O diffusion in sapphire measured using both conventional and microwave heating.	27
Figure 2-8.	Diffusion of potassium in sodium aluminosilicate glass using conventional heating and two different microwave power levels at a temperature of 450°C for 30 minutes.	29
Figure 2-9.	Sketches of a) Typical setup used for joining ceramics in a hot press and b) ceramic shapes commonly joined in a hot press.	34
Figure 2-10.	Schematic showing the six mechanisms of mass transfer that can lead to joining; a) surface sources, b) bonding interface sources c) bulk deformation after yield or during creep.	36
Figure 2-11.	Contact area of a) textured surface and b) smooth surface. Contact area in a) is greater than in b) when the external dimension is the same.	37
Figure 2-12.	Effect of surface roughness (as described in equation 3-1 and figure 3-4) on sample strength.	39
Figure 2-13.	Effect of joining temperature on the strength of a joint.	40

Figure 2-14.	The effect of pressure applied during joining on the strength of the joint.	42
Figure 2-15.	The effect of joining time on the strength of the joint.	43
Figure 2-16.	Graphic representation of the four scales of joining discussed in the text.	45
Figure 2-17.	Energy versus separation for two ions in proximity to each other.	47
Figure 2-18.	Force versus separation for the two ions in figure 2-17.	47
Figure 2-19.	Computer derived, relaxed structure of the BaO/NiO interface.	48
Figure 2-20.	Effect of joining temperature on the strength of 92% alumina.	55
Figure 2-21.	The effect of joining time on bend strength of silicon nitride.	56
Figure 2-22.	Knoop hardness across joint for microwave joined alumina.	57
Figure 2-23.	Acoustic emission traces for a mullite joining experiment.	58
Figure 3-1.	Binary $\text{Cr}_2\text{O}_3\text{-Al}_2\text{O}_3$ phase diagram.	67
Figure 3-2.	Binary $\text{Fe}_2\text{O}_3\text{-Al}_2\text{O}_3$ phase diagram.	67
Figure 3-3.	Setup used to measure temperature of gel compositions heated solely by microwaves (setup was placed in a microwave for heating).	69
Figure 3-4.	Simulated material profile depicting the arithmetic mean.	73
Figure 3-5.	Schematic of the microwave joining apparatus.	78
Figure 3-6.	Photograph of the microwave joining apparatus used in all of the microwave joining experiments.	79
Figure 3-7.	Flowchart used to produce susceptors for microwave joining.	81
Figure 3-8.	Cutaway view of the setup used to evaluate the heating ability of susceptors.	82
Figure 3-9.	Schematic of the specimen/susceptor setup used in the microwave joining experiments.	84
Figure 3-10.	Photograph of susceptor set up inside the microwave cavity.	85
Figure 3-11.	Flow diagram of the microwave joining process and specimen preparation.	88

Figure 3-12.	Flexure fixture for room temperature testing of bars using four-point bending. a) schematic of flexure rig and b) labels of relevant dimensions.	89
Figure 4-1.	Grid structure surrounding node o, the node of interest.	99
Figure 4-2.	Two-dimensional grid structure using the r-z coordinate axes.	99
Figure 4-3.	Model used for the simulation of microwave hybrid heating.	100
Figure 4-4.	Time-temperature coordinates involved in the Crank-Nicolson equation. The trapezoid connects the time-position values used to calculate temperature values at the point indicated, ϕ	102
Figure 4-5.	Logarithmic fit to data for the specific heat of alumina.	115
Figure 4-6.	Linear fit for the specific heat of nickel oxide.	116
Figure 4-7.	Polynomial fit to thermal conductivity of insulating fiber board.	117
Figure 4-8.	Temperature of water as a function of time.	119
Figure 4-9.	Power absorbed (calculated) as a function of temperature for AD995 alumina.	121
Figure 4-10.	Power absorbed (calculated) as a function of temperature for nickel oxide.	122
Figure 4-11.	Power absorbed (calculated) as a function of temperature for the 30 vol. % SiC susceptor.	124
Figure 4-12.	Curve fit for the emissivity of alumina as a function of temperature. .	125
Figure 4-13.	Sample input to calculate a heating profile of the model in figure 4-4.	129
Figure 4-14.	Map of node numbers for the input file in figure 4-13. Geometry corresponds to the model in figure 4-3. The nodes that represent thermocouple locations are 328 (interlayer) and 423 (bulk). The pyrometer is represented by node 328.	131
Figure 4-15.	Temperature profiles for simulated microwave hybrid heating generated using the input in figure 4-13. a) 10 minutes; b) 20 minutes; c) 30 minutes; d) 40 minutes; e) 50 minutes.	132
Figure 5-1.	Area of the surface of alumina end member used for roughness analysis.	138

Figure 5-2.	Profile of 5 mm x 5 mm area of alumina from figure 5-1 analyzed using a laser profilometer. Light regions correspond to the area above mean peak height and darker regions correspond to area below mean peak height.	139
Figure 5-3.	Area of the surface of nickel oxide interlayer used for roughness analysis.	140
Figure 5-4.	Profile of 5 mm x 5 mm area of nickel oxide from figure 5-3 analyzed using a laser profilometer. Light regions correspond to the area above mean peak height and darker regions correspond to area below mean peak height.	141
Figure 5-5.	Temperature of the potential interlayer materials heated using stand alone microwave heating.	142
Figure 5-6.	Differential Scanning Calorimetry (DSC) of the base gel, alone and with additives.	144
Figure 5-7.	X-ray Diffraction Analysis (XRD) of powders synthesized during DSC analysis. Specimens containing iron compounds exhibited spectra with reduced intensities. This is most likely due to the fluorescence of iron from Cu k-alpha radiation. Fluorescence tends to reduce peak/background ratios.	146
Figure 5-8.	Dielectric constant versus temperature of potential interlayer materials. Measured at 2.46 GHz.	148
Figure 5-9.	Dielectric constants, measured at 2.46 GHz, plotted without the iron (III) oxide composition.	149
Figure 5-10.	Dielectric loss factor, measured at 2.46 GHz, versus temperature for potential interlayer materials.	150
Figure 5-11.	Dielectric loss factors plotted without the iron (III) oxide and nickel oxide compositions. Measured at 2.46 GHz.	151
Figure 5-12.	Loss tangent, measured at 2.46 GHz, versus temperature for potential interlayer materials.	152
Figure 5-13.	Loss tangents plotted without iron (III) oxide and nickel oxide compositions. Measured at 2.46 GHz.	154
Figure 5-14.	Temperature of alumina load in silicon carbide/alumina cement susceptors heated using 3.2 KW with a 75% duty cycle (% time on).	155
Figure 5-15.	Dielectric constant, measured at 2.46 GHz, versus temperature for several compositions of susceptors.	156

Figure 5-16.	Dielectric loss factor, measured at 2.46 GHz, versus temperature for several compositions of susceptors. The minimum in the loss factor, associated with some types of silicon carbide, has yet to be explained.	157
Figure 5-17.	Loss tangent for several susceptor compositions at 2.46 GHz.	158
Figure 5-18.	Temperature of susceptors as a function of silicon carbide content. ...	159
Figure 5-19.	Microwave processing conditions for trial #6 (1450°C; 45 min; 3 MPa; nickel oxide interlayer).	161
Figure 5-20.	Conventional processing conditions for trial #11 (1550°C; 15 min; 1 MPa; nickel oxide interlayer).	162
Figure 5-21.	Fracture surfaces of specimens from trial #4 (45 min; 1550°C; 1 MPa; nickel oxide interlayer; microwave heated).	164
Figure 5-22.	Fracture surfaces of specimens from trial #6 (45 min; 1450°C; 3 MPa; nickel oxide interlayer; microwave heated).	165
Figure 5-23.	Fracture surfaces of a flexure bar joined using a gel-derived (4 mol% Cr ₂ O ₃) interlayer.	166
Figure 5-24.	Mean flexure strength of bars for each of the trials in the experimental design. Error bars correspond to one standard deviation.	168
Figure 5-25.	Fracture surface of specimen from trial #12, representative of all the specimens joined using AD94 alumina as the interlayer material. ...	170
Figure 5-26.	Joint line between AD94 alumina interlayer and AD995 alumina end member (250x). Trial #14 (45 min/1450°C/3 MPa/C/AD94).	171
Figure 5-27.	Micrograph of joint region in figure 5-26 showing porosity and grain boundary material (20,000x).	172
Figure 5-28.	Intact interlayer material in bar that fractured away from the joint area. Trial #15 (15 min/1550°C/3 MPa/C/AD94).	173
Figure 5-29.	Joint region of bar from trial #15, flexure strength 220 MPa (250x). Trial #8 (45 min/1550°C/3 MPa/M/AD94).	175
Figure 5-30.	Magnified micrograph of the joint line in figure 5-29 (20,000x). ...	176
Figure 5-31.	Joint area of a bar microwave joined in trial #3 (15 min/1550°C/1 MPa/M/AD94) (6,000x). a) micrograph and b) WDS x-ray map of silicon.	177

Figure 5-32.	Joint area of a bar conventionally joined in trial #15 (15 min/1550°C/3 MPa/C/AD94) (6,000x). a) micrograph and b) WDS x-ray map of silicon.	178
Figure 5-33.	Joint area of a bar microwave joined in trial #2 (45 min/1450°C/1 MPa/M/AD94) (6,000x). a) micrograph and b) WDS x-ray map of silicon.	179
Figure 5-34.	Joint area of a bar microwave joined in trial #8 (45 min/1550°C/3 MPa/M/AD94) (6,000x). a) micrograph and b) WDS x-ray map of silicon.	180
Figure 5-35.	Matching fracture surface of bar joined with a nickel oxide interlayer that failed before flexure testing. Compare to Figures 5-36 and 5-37. Trial #11 (15 min/1550°C/1 MPa/C/NiO).	181
Figure 5-36.	Matching fracture surfaces of bar joined with a nickel oxide interlayer with a flexure strength of 38 MPa. Trial #11 (15 min/1550°C/1 MPa/C/NiO).	182
Figure 5-37.	Matching fracture surfaces of bar joined with a nickel oxide interlayer with a flexure strength of 45 MPa. Texture difference is due to slow crack growth from controlled loading (slow rate). Trial #11 (15 min/1550°C/1 MPa/C/NiO).	183
Figure 5-38.	Micrograph of joint region of bar from figure 5-35 joined with a nickel oxide interlayer (2,000x). Flexure strength 0 MPa.	185
Figure 5-39.	Micrograph of joint region of bar from figure 5-35 joined with a nickel oxide interlayer (5,000x). Flexure strength 0 MPa.	186
Figure 5-40.	Micrograph of joint region of bar from figure 5-37 joined with a nickel oxide interlayer (1,000x). Flexure strength 45 MPa.	187
Figure 5-41.	Micrograph of joint region of bar from figure 5-37 joined with a nickel oxide interlayer (5,000x). Flexure strength 45 MPa.	188
Figure 5-42.	Roughness of joined surface (trial #8) calculated from micrograph taken at 500x.	189
Figure 5-43.	Roughness of joined surface (trial #12) calculated from micrograph taken at 500x.	190
Figure 5-44.	Roughness of as-machined surface calculated from micrograph taken at 500x.	191
Figure 5-45.	Effect of time on the flexure strength of joined bars.	194
Figure 5-46.	Effect of temperature on the flexure strength of joined bars.	195
Figure 5-47.	Effect of pressure on the flexure strength of joined bars.	196

Figure 5-48.	Effect of the heating method on the flexure strength of joined bars. . .	197
Figure 5-49.	Effect of the interlayer material on the flexure strength of joined bars.	198
Figure 5-50.	Effect of the heating method on the flexure strength of joined bars plotted with error bars at the 90% confidence interval.	200
Figure 5-51.	Map of original bar positions in the joined cylinder before machining.	201
Figure 5-52.	Interaction chart showing the combined effect of the position of the bar and the heating method on the flexure strength.	202
Figure 5-53.	Temperature of the workpiece measured using a thermocouple and an optical pyrometer.	205
Figure 5-54.	Variation in temperature of the workpiece between the thermocouple and the optical pyrometer.	206
Figure 5-55.	Temperature of the susceptor measured using both a thermocouple and an optical pyrometer.	207
Figure 5-56.	Variation in temperature of the susceptor between the thermocouple and the optical pyrometer.	208
Figure 5-57.	Temperature (calculated and measured) at the surface of the AD94 interlayer.	209
Figure 5-58.	Temperature (calculated and measured) at the surface of the NiO interlayer.	210
Figure 5-59.	Temperature (calculated) at the surface of the joint region for various heating conditions.	211
Figure 5-60.	Temperature (calculated) at the surface of the end member for various heating conditions.	213
Figure 5-61.	Temperature (calculated) at the surface of the joint region (AD94) and end member (AD995).	214
Figure 5-62.	Temperature (calculated) at the surface of the joint region (NiO) and end member (AD995).	215
Figure 5-63.	Comparison of calculated temperatures for specimens heated with nickel oxide interlayers of different thickness.	216
Figure 6-1.	Phase diagram of the FeO-Al ₂ O ₃ system.	220

Figure 6-2.	Qualitative representation of the effect of temperature on the dielectric loss factor of a typical dielectric material. Tc refers to the critical temperature at which the efficiency of the absorption of microwaves increases dramatically.	222
-------------	--	-----

Abstract of Dissertation Presented to the Graduate School of the University of Florida in
Partial Fulfillment of the Requirements for the Degree of Doctor of Philosophy

THEORY AND APPLICATION OF MICROWAVE JOINING

By

ALEX DOUGLAS COZZI

August 1996

Chairperson: Dr. David E. Clark

Major Department: Materials Science and Engineering

Microwave processing of materials is advancing from a novel processing technique into a viable method for processing industrial materials. It has been adopted by several industries for the following reasons. Microwave processing can afford savings in energy or space or, more importantly, it can provide a product with qualities that cannot be achieved through conventional means. Even as the use of microwave processing increases in industry, it is vigorously investigated by researchers attempting to better understand and control the mechanisms that are responsible for microwave heating of materials. These investigators are seeking evidence that can either demonstrate or disprove the concept of enhanced microwave processing. Simultaneously, researchers also are looking for innovative techniques that can provide other industrial applications for microwaves.

Joining has always been an integral component of the manufacturing industry. The joint is often the weakest link of any manufactured item and researchers are continually pursuing means of increasing the strength of the joint. Several ceramics have been joined successfully using microwave energy. However, there are no processing guidelines available so the data that have been generated cannot be easily compared. Furthermore,

much of the previous work reports the condition of the joint qualitatively, making comparisons of joining procedures nearly impossible.

The research performed in this study attempts to address many of the issues discussed above. The main goal of this research is to join alumina using microwave energy and to develop an understanding of the microwave interactions with materials and its relation to the joining process.

An apparatus for the microwave joining of materials was designed and put into use. A procedure for producing susceptors for microwave hybrid heating was developed. Using the microwave joining apparatus and hybrid heating, high-purity alumina was joined using several materials as the interlayer between the alumina end members. An experimental design was used to provide data that then could be analyzed statistically to determine the significance of the processing parameters varied during joining. A numerical model simulated the microwave heating of the joining process. Simulated temperature profiles were compared to experimentally measured temperatures to assess the usefulness of the model.

CHAPTER 1

INTRODUCTION

Joining is an important step in the construction of engineering structures. This may seem obvious when one thinks about the erection of a building or the assembly of an automobile. However, joining is also a vital process in the formation of many of the components that are later joined to produce these buildings and automobiles. The joining process also extends beyond mechanical joints formed through the use of fasteners such as bolts, nails and clamps. A remarkable number of products contain components that are joined through chemical reactions.

While it is often preferable to fabricate the components that are used to assemble products in one piece, it is not always possible or even the prescribed method for manufacturing the desired shape. This is most apparent when the final product consists of more than one material. Some of the newer types of cookware consist of a piece of stainless steel sandwiched between two aluminum sheets. The stainless steel provides a high heat capacity base needed for stove top cooking, while the aluminum contributes a high thermal conductivity for even heating. Another example where joining is the preferred method of manufacture is when the piece consists of a complex shape that would require either a complicated mold or extensive machining. Joining can also be useful when a compressive stress is added to increase the strength of the component. This effect is observed when glaze is fired on a ceramic piece with a lower coefficient of thermal expansion than the glaze. When the product cools, the glaze will contract more and be put under a compressive stress.

All types of materials--ceramics, metals and polymers--have been joined to one another for a multitude of applications. The applications that entail the joining of ceramics are extensive. The most common joint involving ceramics is a ceramic to metal joint. These types of joints are used in light bulbs to connect the metal base to the glass tube, and also in spark plugs, to attach the metal core to the ceramic sheath. Ceramic/metal joints are created in the enameling of household appliances such as washing machines and dishwashers. The enamel coating on the steel housing not only increases the aesthetic value of the appliance, but also serves as a rust-resistant coating on the steel. While the ceramic/ceramic joint is somewhat less prevalent than the ceramic to metal joint, it plays an important role in the traditional ceramic industries. Two of the most widely used examples of ceramic/ceramic joints are joining bricks with mortar and attaching a handle to a ceramic mug. The use of mortar to join bricks relies on the room temperature cementitious reaction. This reaction causes the mortar to harden, thus joining the two bricks. The practice of joining a handle to a ceramic mug is similar to joining bricks with mortar in that the interlayer material contains an appreciable amount of water. When attaching handles to mugs, the interlayer material is usually the same composition as the end members (cup and handle). The joint is formed during the sintering of the interlayer material with the end members at elevated temperatures. While these applications are less glamorous than the heat resistant coating on space shuttle tiles, they make up a much greater share of the ceramic market. In the field of structural ceramics, the greatest motivation to apply joining techniques is the size limitations placed upon the part by the densification apparatus. Large parts such as heat exchanger tubes can exceed fourteen feet in length. This requires the joining of smaller sections to complete the part.

The formation of a ceramic to ceramic joint is not as straightforward as the typical metallic joint. Most metallic joining operations include the formation of a liquid phase. The liquid phase is usually made up of material from both end members and produces a

joint with properties that gradually change from those of one end member to those of the other. The properties of ceramic joints made without liquid phase can change abruptly from one end member to the other. Ceramic to ceramic joints are pursued because they provide an opportunity to improve the final properties of the product. Ceramic to ceramic joints can furnish an increased resistance to operating temperature over metallic alloys. They also are more resistant to oxidation than most metal alloys. The enhanced resistance to degradation and oxidation of ceramics over metals in high-temperature, corrosive applications can be used to increase the efficiency of heat exchangers and turbine engines.

The joint area in this dissertation is considered to be the area that encompasses the interlayer and the portion of the end members that has been altered during the joining process. The joint can be described in three ways: according to its chemical, microstructural or physical properties. In the first description, joining can be described chemically by the mixing of the atoms of the components being joined. The mixing of the atoms of the two components can result in the formation of a third component. When the mixing of atoms is limited to materials that have mutual solubility, the concentration of atoms gradually changes from 100% of the first material to 100% of the second material. Secondly, the joint region may possess a microstructure similar to one or both of the pieces being joined or it may be unique. A third classification would be to define the joint physically. This is the manner in which the end members are macroscopically connected or somehow attached. Although basic in description, this is the definition of "joined" that matters most to consumers.

The definition of "joint" depends on the desired use of the end product. For the ceramic to metal joint of the light bulb described above, hermeticity of the joint is the most important feature with the strength of the joint only having to meet some minimum requirement. For the purpose of this dissertation, "joint" will be referred to as the region between two bulk materials that has a chemical composition or mechanical properties

different from either of the end members or the interlayers used in the joining process. Materials are determined to be "joined" when they do not separate during normal handling.

Until recently, most of the work performed in the joining of materials has used conventional heating. That is, the specimens to be joined were heated in either a resistance or radio frequency (RF) heated furnace. Radio frequency heating is limited to materials that are electrically conductive and capable of supporting an induced current. There has also been some work done using lasers to heat the workpieces. Lately, microwaves have been used to provide the energy necessary to heat the specimens to temperatures suitable for joining. This has brought about a discussion of whether microwave heating can contribute to the joining process in some way besides its use of an alternate heat source. There are many reports of enhanced diffusion and lowered activation energies of transport that will be discussed later. It is certain that if either of the above mentioned phenomena can be shown to occur during the joining process in a microwave field, there could be a definite advantage in the use of microwaves to join ceramics.

The goal of this research then, is to join alumina using microwave energy and to develop an understanding of the joining process. In the literature, there are many models to predict joining behavior between two materials of identical, similar or differing compositions using conventional heating. There is also an abundance of experimental data to support these models. Several models of microwave interactions with materials also can be found in recent publications. These models and the experimental data to support them are not as prevalent. In attaining the goal of this research, it is necessary to identify, and begin to establish, the intersection of these two separate fields of study, figure 1-1.

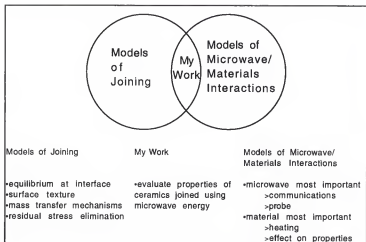


Figure 1-1. Schematic depicting the intersection of two fields of modeling to form a basis for research.

While working toward the stated goal, the following objectives were identified and achieved.

- Review the fundamentals of joining.
- Review the principles of microwave interactions with materials that are relevant to joining.
- Design and construct an apparatus for microwave joining.
- Prepare joined specimens that have strength approaching that of the original material.
- Evaluate the integrity and uniformity of joints based on strength.
- Demonstrate enhancements, if any, achieved during microwave joining.
- Use statistical tools to qualitatively assess the joining parameters used in this study.
- Employ numerical modeling to approximate heat flow during joining.

These objectives form the framework of the research performed. They also acted as guidelines throughout the course of the study.

Several significant achievements have been realized during the course of this study. These achievements either extend beyond the anticipated success of the associated objective or, were accomplished in addition to the objectives. 1) A new generation of microwave susceptors has been developed and characterized. 2) A microwave joining apparatus was designed and constructed using closed loop control of the applied force and temperature. 3) An experimental design to provide the data for a statistical analysis of the effects of joining parameters on flexure strength was constructed. 4) A heat transfer program was manipulated to generate temperature profiles in a model that compares calculated temperatures with experimentally measured temperatures. The calculated values provided results comparable with other microwave heating models available in the current literature.

CHAPTER 2

SURVEY OF THE LITERATURE

Microwaves

Background

Like visible light, radio waves and x-rays, microwaves are a part of the electromagnetic spectrum. Microwaves extend between the frequencies of 300 megahertz (MHz) and 300 gigahertz (GHz)¹. This corresponds to wavelengths ranging from about one meter to less than one millimeter in length.

In the past, microwaves were used almost exclusively in the field of communications². Any electromagnetic losses in the materials used were considered detrimental. The relatively recent introduction of microwave ovens (1960s) to the general public was a result of the realization that electromagnetic losses could be used for the purpose of cooking. This was possible because the interactions of microwaves at 2.45 GHz with the water in foods provided efficient and rapid heating. In 1985, Meek³ exploited the generation of heat due to the electromagnetic losses in materials that do not contain water. He was able to heat a ceramic material to a high enough temperature to induce melting. Shortly thereafter, Meek⁴ proposed a model for the microwave sintering of powders of dielectric materials. He describes the powder compact as a material/porosity (air) composite. Meek then suggests that the higher electric field in the porosity induces densification in nearby grains.

Metaxas and Meredith⁵ furnish a thorough explanation of the theory behind the microwave heating of materials. Heat generated due to losses in a material is related to the

electric permittivity (ϵ^*) and magnetic permeability (μ^*) of the material. Most ceramic materials are not significantly influenced by the magnetic portion of the wave, therefore the contribution to heating produced by the magnetic losses are generally ignored. Fathi⁶ provides an excellent review (from a materials science perspective) of the theory behind the interactions of microwaves with materials. He discusses the different types of polarization and the losses associated with them. Space charge polarization and orientation polarization are the two active mechanisms in the microwave frequency range. Space charge polarization refers to the charge build up at the interfaces of a non-homogeneous material in an alternating electric field. Orientation polarization occurs in materials that are comprised of permanent dipoles that have asymmetric charge distributions. The dipoles tend to reorient in an alternating electric field. Fathi also describes the historical development of the theory and equations pertaining to the dielectric heating of materials. The electrical permittivity of a material is defined by the equation

$$\epsilon^* = \epsilon' - j\epsilon'' = \epsilon_0 (\epsilon'_r - j\epsilon''_r) \quad (2-1)$$

where

- ϵ' : dielectric constant (real)
- ϵ'' : dielectric loss factor (imaginary)
- ϵ'_r : relative dielectric constant (ϵ'/ϵ_0)
- ϵ''_{eff} : effective relative loss factor $= \epsilon''_r + \sigma/\epsilon_0\omega$
- ϵ''_r : relative loss factor
- σ : electrical conductivity (ac + dc)
- ϵ_0 : permittivity of free space
- ω : angular frequency $= 2\pi f$, f in Hz.

The dielectric constant (real) and the dielectric loss factor (imaginary) of a material can be measured experimentally. Using cavity perturbation theory, Hutcheon et al.⁷ were able to measure the complex permittivity of several materials. They then were able to mathematically isolate the real and imaginary portions of the complex permittivity. These

values describe the polarization and conductivity losses generated in a material. The loss tangent, $\tan \delta$, relates the real and imaginary terms:

$$\tan \delta = \frac{\epsilon''}{\epsilon'} \quad (2-2)$$

The value of $\tan \delta$ determines the amount of energy dissipated in a material exposed to an alternating electric field. In an ideal dielectric, the induced current will lead the applied voltage by an angle of 90° and $\delta = 0$. In a real material, the time required for polarization causes a phase shift in the induced current in the dielectric, represented by the angle δ in figure 2-1. These losses are temperature dependent and can change rapidly over small temperature regimes. Hutcheon et al.⁸ were able to measure the complex permittivity in a material up to 1400°C . This made it possible to predict heating behavior of the material in a microwave field. Another equation developed by Metaxas and Meredith⁵ that is necessary to understand microwave heating identifies the average power absorbed in a unit volume, P_{av} as

$$P_{av} = \omega \epsilon_0 \epsilon'' E_{rms}^2 \quad (\text{W/m}^3) \quad (2-3a)$$

in terms of $\tan \delta$

$$P_{av} = 2\pi f \epsilon_0 \epsilon' \tan \delta E_{rms}^2 \quad (\text{W/m}^3) \quad (2-3b)$$

where

- ω : angular frequency = $2\pi f$
- f : frequency of microwaves, in GHz
- E_{rms} : internal electric field (root mean square) (V/m).

The complexity of this equation arises in the determination of the internal electric field, which can vary with position and temperature. The authors also derive and simplify other

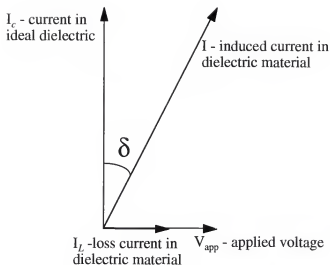


Figure 2-1. Representation of the lag in the current that determines the loss tangent. The dielectric conductivity is a real number so the loss current is in phase with the applied voltage, V_{app} .

pertinent equations such as the penetration depth of the microwaves in the material, D_p . The penetration depth is defined as the distance from the material's surface to the point at which the power drops to e^{-1} of its surface value. This equation is also affected by temperature due to the temperature dependence of ϵ''_{eff} and ϵ' ,

$$D_p = \frac{\lambda'_0}{2\pi(2\epsilon')^{\frac{1}{2}}} \left[\left(1 + \left(\frac{\epsilon''_{eff}}{\epsilon'} \right)^2 \right)^{\frac{1}{2}} - 1 \right]^{-\frac{1}{2}} \quad (2-4a)$$

For low loss dielectrics ($\epsilon''_{eff}/\epsilon' \ll 1$) the equation is

$$D_p = \frac{\lambda'_0 (\epsilon')^{\frac{1}{2}}}{2\pi \epsilon''_{eff}} \quad (2-4b)$$

where λ'_0 is the wavelength of the electric field in free space. The errors associated with the simplification of the penetration depth increase as the ratio $\epsilon''_{eff}/\epsilon'$ approaches one. Table 2-1 contains some representative values of ratios and errors calculated for a frequency of 2.45 GHz.

Table 2-1. Error Associated with Simplified Equation for Penetration Depth for Several $\epsilon''_{eff}/\epsilon'$ Ratios.

$\epsilon''_{eff}/\epsilon'$	% error
0.009	0.1
0.3	1
0.7	5
1	9

Microwave Applicators

The difference between the two most common types of microwave ovens is in the microwave cavity where the material is processed. A multimode cavity is a metal box with an opening in which microwaves are introduced. The microwaves, once introduced into the cavity, reflect off the walls setting up a number of standing waves. The electric field in multimode cavities is not very uniform and requires either a turntable or a mode stirrer (rotating metal fan) to improve the uniformity of the electric field. A single mode cavity has dimensions that are more precise than the multimode cavity. The length of the single mode cavity is approximately the size of the wavelength of the microwave frequency being used. One wall is adjustable so that the cavity can be tuned to the precise length to produce a single standing wave. The advantage of multimode microwave ovens is that they can be fabricated in almost any dimension and are relatively inexpensive. Single mode microwaves have a calculable electric field that permit the identification of the position of the high field strength. As opposed to single mode microwaves, multimode microwave ovens are not capable of developing the power densities necessary to produce efficient heating. Power densities of 10^7 kW/m³ can be achieved in a tuned single mode cavity⁵. Typical power densities of 3 kW/m³ are produced in multimode microwave ovens for home use⁵. In a tuned single mode cavity, incident and reflected waves are superimposed and the position of maximum electric field can be determined. The specimen to be heated can be positioned to provide the optimum transfer of energy. However, in a multimode cavity the microwaves are constantly being perturbed and scattered, minimizing the chance that a specimen is positioned at the point of maximum electric field for more than a few seconds.

In order to heat most ceramic materials in a multimode microwave oven, it is beneficial, if not essential to use microwave hybrid heating (MHH). Microwave hybrid heating incorporates a strong microwave absorbing material into a surrounding piece of

insulation. This material absorbs more microwaves than the material being processed. Silicon carbide is the most common material of choice as the microwave absorbing material in MHH. Silicon carbide is an excellent and inexpensive microwave absorber that can be used in air at elevated temperatures. Above 900°C, the silicon carbide will oxidize to form a protective silica layer. The weight gain associated with the oxidation increases as the temperature increases⁹. The combination of the absorbing material and the insulation is commonly called a microwave susceptor. The purpose of the susceptor is to assist the material of interest in heating to the processing temperature. The development of microwave susceptors has empowered researchers to investigate low loss materials such as high-purity alumina using multimode microwave ovens.

One of the common modifications made to a microwave cavity is the addition of holes to provide access for either a thermocouple, optical pyrometer or other probes. Holes also may be necessary for the application of pressure to a workpiece in a microwave cavity. The presence of holes in the cavity necessitates the use of some type of choking system to prevent microwaves from escaping and presenting a potential health hazard. Holes of a diameter less than one-quarter of the wavelength (3.06 cm for microwaves at 2.45 GHz) theoretically emit no microwave energy. This originates from the equation

$$Z = Z_0 \tan(2\pi d / \lambda) \quad (2-5)$$

where

- Z = input impedance of hole
- Z_0 = characteristic impedance of hole
- d = diameter of hole
- λ = wavelength of microwaves in cavity.

If $d = \lambda/4$, the input impedance goes to infinity and the hole acts as a open circuit. The microwaves are reflected back into the cavity as if the hole did not exist. At aperture sizes

from $0 < d \leq \lambda/2$, there is a small impedance associated with the aperture than can lead to a small emitted electric field. In reality, the wall material (usually aluminum or steel) has a finite impedance and can emit a portion of the incident microwaves. Cathey¹⁰ developed two equations to calculate the ratio of the electric field scattered through an aperture to the incident electric field,

$$\frac{E_s}{E_i} = \pi \frac{d}{\lambda} \exp \left[-\pi \left(\frac{\lambda}{2d} - 1 \right) \frac{z}{\lambda} \right], \quad \frac{z}{\lambda} \leq \frac{d}{4\lambda} \quad (2-6a)$$

and

$$\frac{E_s}{E_i} = \frac{\frac{\pi}{4} \left(\frac{d}{\lambda} \right)^2 \exp \left[-\frac{\pi}{8} \left(1 - \frac{2d}{\lambda} \right) \right]}{\frac{z}{\lambda}}, \quad \frac{z}{\lambda} \geq \frac{d}{4\lambda} \quad (2-6b)$$

where

- E_s = scattered electric field, V/m
- E_i = incident electric field, V/m
- d = aperture diameter, m
- λ = wavelength of microwave, m
- z = distance from aperture, m.

This is the case for the viewing port for an optical pyrometer and the thermocouple feedthrough. At an aperture diameter to wavelength ratio of 0.5, the intensity of microwaves transmitted through the aperture becomes significant. Proximity to an aperture greater than one-half the wavelength of the microwaves can pose a health hazard. Cathey then calculated the ratio of transmitted to incident field for a range of aperture diameters, figure 2-2. It can be ascertained from figure 2-2 that for an aperture of $\lambda/4$ or less, the fraction of transmitted power is small and attenuates quickly. As the aperture size is increased, the intensity of the transmitted field increases greatly. In the situation where a load is to be applied within the cavity, the hole, or aperture, is partially filled with a

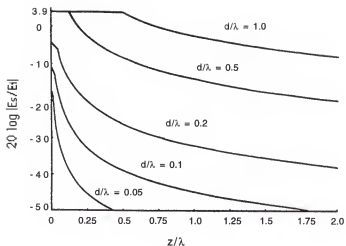


Figure 2-2. Ratio of transmitted to incident field for aperture diameter, $0.05 < d/\lambda < 1.0$.

dielectric material. This material, typically alumina, is used to transfer the load from the external load cell to the workpiece. Here, the wavelength of the microwaves is decreased by the square root of the dielectric constant of the filling material⁵. The decrease in wavelength makes it possible for the incident microwaves to pass through a smaller aperture than expected. This condition requires additional modifications to effectively attenuate the microwaves. Metaxas and Meredith⁵ describe the use of a circular tube of conducting material as a choke. If the diameter of the tube is less than one-half of the incident wavelength, the microwaves are attenuated and the transmitted power decreases rapidly. Under these conditions ($d < \lambda/2$), the attenuation of the power is proportional to e^{-z} , where λ is the wavelength of microwaves in the dielectric material and z is the length of the choke.

Microwave Processing of Materials

In the past fifteen years, numerous efforts to take advantage of the unique capabilities of microwave processing have been undertaken. Sutton¹ outlines the potential advantages of several characteristics of microwave processing over conventional heating processes. These advantages include 1) uniform heating of large sections of material, 2) heating above 2000°C in air, vacuum or controlled atmospheres, 3) rapid processing with reduced grain growth, 4) accelerated sintering and diffusion due to high electric fields, 5) selective heating of particular materials or phases and 6) improvement of mechanical properties. Katz and Blake¹¹ demonstrated that uniformity could be achieved over a large area by simultaneously sintering twenty alumina cylinders. They reported that dimensional tolerances were maintained from experiment to experiment as well as among specimens within each experiment. Holcombe¹² reported attaining a temperature of 2150°C when sintering boron carbide and Tian et al.¹³ reached a temperature of 2200°C when sintering

silicon carbide in a positive pressure argon atmosphere. Other non-oxides have been processed under flowing argon with the resulting x-ray diffraction pattern primarily indicating peaks of the desired phase¹⁴. Using microwave hybrid heating, Dé¹⁵ rapidly sintered high-purity alumina to a nearly fully dense state. In Dé's experiments, specimens were held at the sintering temperature for thirty-five minutes. The lack of significant grain growth reported was analogous to that exhibited in conventional rapid sintering. The author also reported uniform hardness measured across a 25 mm diameter specimen. Moore et al.¹⁶ used the concept of selective coupling to demonstrate the effectiveness of microwave heating. The authors used a lossy binder in the forming step of alumina compacts. When heated using microwaves, the binder burned out cleanly leaving the alumina unaffected. In an attempt to organize their approach to microwave processing, Janney et al.¹⁷ constructed guidelines for microwave processing at the Oak Ridge National Laboratory. They describe the specimen/insulation configurations used and the temperature measurement methods that provided consistent results. The progress demonstrated by researchers worldwide in the microwave processing of materials gained the attention of the U.S. government. Stein et al.¹⁸ summarized a report commissioned by the Department of Defense (DoD) and the National Aeronautics and Space Administration (NASA). This report assessed the current status of the technology, ascertained which applications of the technology show promise to provide energy or space savings and recommended future activities in the field of microwave processing. Two industries in which microwave processing has progressed from an emerging technology to a mature process are the rubber industry¹⁹ and the food industry²⁰.

Numerical Modeling of Microwave/Material Interactions

Until now, all of the discussion concerning microwave/materials interactions has been phenomenological. That is, only the behavior of materials after exposure to

microwaves has been considered. Due to the complexity and multiple interactions of the components in equation 2-3, many researchers do not consider the theoretical aspects of microwave heating. Another more practical reason that theoretical approaches are avoided is the difficulty in measuring the conditions within the microwave during processing. More specifically, it is very difficult to determine the electric field in a material inside a microwave oven. Properties such as the dielectric constant and the loss tangent are temperature dependent. The interaction of the electric field with the dielectric material in the cavity alters the field through absorption or reflection of the waves.

To calculate the electric field in a microwave cavity, it is necessary to solve Maxwell's equations simultaneously. Yee²¹ was the first to develop a numerical solution for these equations in an isotropic medium by replacing them with a set of finite difference equations. Previous to Yee's work, scattering of the electric field was calculated by a laborious integration method that required numerous subdivisions of the material being evaluated²². Taflov and Brodwin²³ extended Yee's findings to determine the field within a dielectric cylinder.

One of the early applications of the finite difference modeling techniques was used in response to cataracts that developed in the eyes of microwave generator operators²⁴. The model was implemented to predict the electromagnetic fields and temperature induced in a microwave irradiated human eye²⁵. Recently, a similar model was used to determine the specific absorption rate of various body components²⁶. The authors suggest that it is possible to take advantage of the potential for selective heating of various types of tissue in surgical procedures.

The bulk of the research in microwave/material interactions has been performed in the food industry. Datta²⁷ judged the determination of the fields within a loaded microwave environment to be too complex to predict accurately. The author concentrated on predicting

the heat and mass transfer associated with microwave processing of foods. Figure 2-3 compares the experimentally and predicted temperatures in a cylindrical roast beef heated using microwaves. In a rigorous evaluation of microwave induced heat and mass transfer in baked dough products, Tong and Lund²⁸ considered the temperature dependence of the dielectric properties of the materials. The authors were able to measure the field strength near the subject's surface and use these values for the model. Figure 2-4 compares their model to experimental results obtained in two different microwave ovens. Pangrle et al.²⁹ introduced the use of finite element analysis to model the microwave thawing of pure water cylinders. Subsequently, Pangrle et al.³⁰ extended the model to multilayer beef/water composites. Many authors choose to neglect the temperature dependent properties of the materials being heated. Ayappa et al.³¹ used the finite element method to determine the effect of the temperature dependent properties on the temperature of various materials. Ayappa et al.³² then extended their finite element model to a 2-dimensional situation. Figure 2-5 is the temperature distribution of microwave heated raw beef using both temperature dependent and constant dielectric properties.

In ceramics, Watters et al.³³ used difference equations to calculate transient temperature profiles in a ceramic using a simplified geometry to represent the ceramic specimen. Gupta and Evans³⁴ developed a 1-dimensional numerical model for chemical vapor infiltration (CVI) using microwave heating. Using an integral method³⁵ for microwave material interactions, Gupta and Evans³⁶ calculated the temperature in a microwave heated 2-dimensional body. In the complicated system of hydrated porous concrete with variable dielectric properties, Li et al.³⁷ developed a numerical 1-dimensional model to determine the temperature and steam pressure developed during microwave heating. Ferber et al.³⁸ were able to calculate stress and temperature distributions for a simplified geometrical model of a ceramic window subjected to microwave heating.

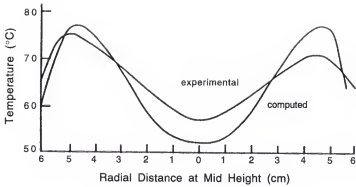


Figure 2-3. Radial temperature profiles in a cylindrical roast beef²⁶.

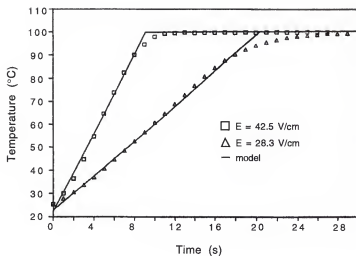


Figure 2-4. Temperature of bread heated with two different field strengths²⁸.

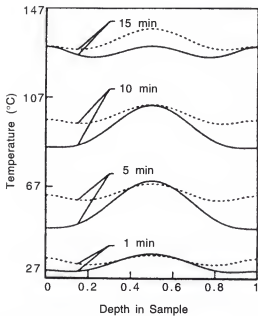


Figure 2-5. Effect of variable (—) versus constant (---) dielectric properties on temperature in a raw beef sample. Depth in sample refers to fraction of whole³².

The joining of ceramics using microwave energy has been considered theoretically³⁹. It was suggested that the joint area be positioned in the area of a hot spot to facilitate joining. However, no experimental data is presented in conjunction with the numerical model. Dibben et al.⁴⁰ presented a finite element and a finite difference method for the modeling of the sintering of ceramics in a multi-mode microwave cavity. Their effort included solving Maxwell's equations and producing 3-dimensional plots of electric field and power density as a function of position. The finite difference method was used to calculate temperatures in a 3-dimensional specimen⁴¹. To calibrate their model with the microwave used for the experiments, water loads were heated and the electric field was calculated from the rate of rise in temperature of the water. In a 1-dimensional model, Skamser and Johnson⁴² developed a system to simulate microwave hybrid heating. The microwave field was assumed to be uniform throughout the microwave. Temperature dependent dielectric properties of the alumina fiber specimens were varied; those of the susceptor were kept constant. Microwave hybrid heating experiments were carried out by Thomas et al.⁴³ using zirconia as the susceping material. Measured temperatures of the workpiece and the insulation were compared to those calculated using a 2-dimensional numerical model. Differences between the measured and calculated temperatures of the workpiece were as much as 120°C during heating. In the insulation these temperature differences exceeded 200°C. When the temperature of the workpiece reached the sintering temperature, the calculated and measured temperatures converged. Figure 2-6 is the computed and measured temperatures of the workpiece and the insulation.

Kriegsmann⁴⁴ proposed a 1-dimensional model to explain the phenomenon of thermal runaway that is occasionally experienced during the heating of ceramics using microwave energy. The author later expanded the model to encompass ceramic fibers and proposed that there exist stable temperatures for given power levels in systems with highly

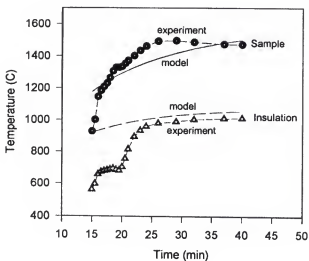


Figure 2-6. Measured and computed temperatures for the specimen and the insulation during a microwave sintering run⁴³.

specified boundary conditions⁴⁵. Spatz et al.⁴⁶ use the principles put forth by Kriegsmann to compare experimentally determined thermal stability conditions. They concluded that microwave hybrid heating is an effective procedure for limiting the formation of hot spots that can lead to thermal runaway. Beale and Artcaga⁴⁷ proposed the use of a closed loop control system to use feedback from a thermocouple to prevent thermal runaway during the microwave joining of ceramics. Numerical simulations by the authors indicate that this system demonstrates potential for experimental applications.

One element of the modeling that has been a constant source of difficulty is resolving the electric field strengths through Maxwell's equations. Ayappa et al.⁴⁸ investigated the applicability of using Lambert's law to predict electric field strengths. Lambert's law describes the exponential decay of the power flux from an initial intensity and is expressed as

$$I(z) = I_0 e^{-2\beta z} \quad (2-7)$$

where

- I_0 = transmitted power flux (W/m^2),
- β = penetration depth (cm) and
- z = distance from the sample surface (cm).

The authors have determined a critical slab thickness (L_{crit}) above which Lambert's law is valid. The critical thickness is dependent upon the penetration depth, equation 2-4a as

$$L_{\text{crit}} = 2.7\beta - 0.08 \quad (2-8)$$

The validity of Lambert's law can be quickly determined for any materials system by calculating the critical thickness at the lowest temperature of interest. That is, the temperature with the largest penetration depth. This will ensure that Lambert's law will be valid over the entire temperature range examined. The critical thickness for several ceramic

materials at a microwave frequency of 2.45 GHz are listed in Table 2-2. A sample calculation of the penetration depth and critical thickness is in Appendix A. When the critical thickness exceeds the sample thickness, it becomes necessary to solve Maxwell's equations to determine the power within a material.

Table 2-2. Critical Thickness and Penetration Depth at Different Temperatures for Several Ceramic Materials at a Frequency of 2.45 GHz.

Material	Temperature (°C)	Penetration Depth (cm)	Critical Thickness (cm)
99.5% alumina	25	9553	25,793
	1000	205	553.4
Al-66 cement	25	127	342.8
	1000	28	75.5
nickel aluminate	25	1848	4989
	1000	5.4	14.5

Evidence of Microwave Enhancements

In the first reported evidence of enhanced diffusion, Janney and Kimrey⁴⁹ used ¹⁸O tracer in a single crystal sapphire substrate in side by side annealing experiments using microwave and conventional heating. Oxygen was selected instead of a more easily traced species to avoid differential microwave coupling during the test. Figure 2-7 compares the activation energies of diffusion for the two processes over a range of temperatures. A single crystalline sample was used to eliminate microwave interactions with the grain boundary phase. These interactions contribute to the decrease in activation energy. The authors do not offer any explanation for the perceived effect. Fathi et al.⁵⁰ performed ion exchange in sodium aluminosilicate glasses. The authors exchanged potassium ions from a salt with the sodium of the glass. The diffusion constants then were calculated from ion concentrations that were measured using electron microprobe analysis. A variation in the soda/alumina ratio resulted in differing penetration depths of the potassium ions. These

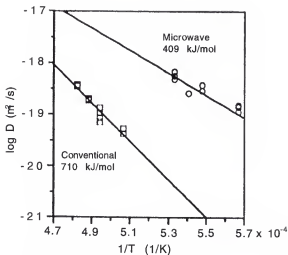


Figure 2-7. The activation energy for ^{18}O diffusion in sapphire measured using both conventional and microwave heating⁴⁹.

results were compared to identical ion exchange experiments carried out using conventional heating. At soda/alumina ratios near 1:1, the measured diffusion distance of the potassium ions is much greater in the microwave processed glasses than in the conventionally processed specimens. As the ratio is varied from 1:1 in either direction, the differences in the diffusion distance of the potassium ions were less discernible. In another variation of the experiment, a smaller susceptor was used and more microwave power was utilized to attain the required temperature. Figure 2-8 compares the use of two different microwave powers with conventional heating for the ion exchange of $K^+ \leftrightarrow Na^+$ at 450°C.

To examine the effect of defect concentrations on diffusion in a microwave field, Ahmad⁵¹ diffused zinc oxide into single crystals of sapphire with differing amounts of lattice defects. He correlated the concentration of defects with the rate of formation of zinc aluminate spinel. Similar experiments were executed by Fathi et al.⁵² using chromium oxide as the diffusing species. No microwave effect was reported, but the authors considered this evidence that thermometry was an acceptable measurement technique in a microwave field. Tieg et al.⁵³ employed the premise of selective coupling described earlier to couple microwave energy with the grain boundary phase of a low loss silicon nitride. A post sintering anneal of the sintered specimens was carried out using both microwave and conventional heating⁵⁴. It was reported that in the specimens with a significant volume of grain boundary phase, there was an improved resistance to creep deformation.

Joining

Joining Methods

The term "joined" has several meanings in the materials world. It refers to components that are held together by one of several methods. The two main types of joining are mechanical joining and chemical joining. Mechanical joining uses fasteners or

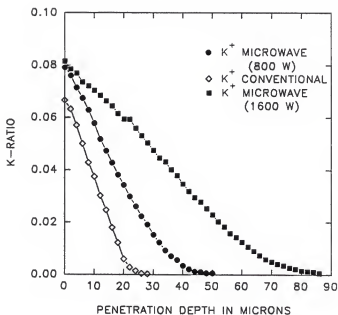


Figure 2-8. Diffusion of potassium in sodium aluminosilicate glass using conventional heating and two different microwave power levels at a temperature of 450°C for 30 minutes⁵⁰.

clamps to join two or more distinct pieces together. It is probably the most preferred method of joining because the parts can often be easily separated at a later time for repositioning or for re-use. Another type of mechanical joining involves the use of interlocking pieces, such as a tongue-in-groove floor or a dovetail joint on a birdhouse roof.

The other type of joining -- chemical joining -- can be further subdivided into direct joining and indirect joining. Direct joining is the adherence of two components directly to each other. These components can be either identical or different. The case in which the two materials are identical is an attractive process because it minimizes the number of components involved. It also eliminates the chance of mismatches in the thermal expansion of the materials, which can lead to a weak joint. Direct joining of similar materials can be accomplished by heating the area near the joint to a temperature at which a liquid will form. However, there are not many materials that can be effectively joined in this manner⁵⁵. In ceramics, low thermal conductivity can result in material failure due to stresses that develop during heating. When the two materials to be joined directly are different, the presence of a compositional gradient provides a driving force for joining. Here also, care must be taken to minimize the thermal stresses that can be induced during the joining process. Thermal stresses can lead to low joint strengths⁵⁶. These stresses are induced by a mismatch in the thermomechanical properties of the dissimilar materials.

Indirect joining employs a third component between the end members that facilitates the bonding of the two parts. This is an excellent alternative to the direct bonding method. Here, the end members can be either identical or dissimilar in composition. When the materials are identical, the interlayer provides a compositional gradient to assist in the joining process. In the case of dissimilar materials, the interlayer material is often chosen to have thermomechanical properties between those of the end members so that thermal

stresses are minimized⁵⁷. These interlayers are more commonly referred to as functionally graded interfaces and will be discussed later in this chapter.

In addition to the various methods of joining, there are many ways to determine whether components are joined. The final application of the joined materials is instrumental in defining what is considered to be an acceptable joint. To say that pieces are joined may mean welding two parts together so there is a gradient of chemical composition or mechanical properties from one material to the next. It can also indicate the joining of a film to a substrate where the purpose of joining the pieces is for physical support of the film. Little or no chemical reaction is desired between the two materials. This joint may be mechanically weak but still acceptable because it met the minimum requirements for use. An example of this type of joint would be superconducting films on an alumina substrate. The superconducting films form a Josephson junction and can detect small magnetic fields. There is also the case of the ceramic/metal joint in a light bulb where the hermeticity of the joint is the determining criterion for suitability. In this case it is not so much the strength or the amount of reaction between the end members that's important, but the ability of the joint to maintain a vacuum at elevated temperatures.

For the purpose of this work, a joined specimen will be defined as two or more components that are physically and chemically attached after exposure to a high temperature and an applied load. Additionally, the components may not be easily separated during normal handling.

Currently, there are many processes in which the previously described methods of joining can be accomplished. Joining by mechanical means requires not only knowledge of the materials being joined, but also requires extensive design skill⁵⁵. In chemical joining, some processes involve only the heating of the area to be joined, whereas others require the entire workpiece to be heated to the joining temperature. The application of pressure on the joint area is usually required during the joining process to form a suitable bond.

Joining processes

Bolting. Bolting materials together is a popular method of joining metals. With ceramic/metal joints care must be taken to avoid stress concentrations⁵⁵. This can be done with the use of a soft washer (either lead or copper) between the metal bolt and the ceramic piece.

Clamping. As with bolting, clamping requires the spreading of the load placed on the ceramic material. Similarly, bending loads should be avoided and gaskets should be used at all ceramic/metal interfaces⁵⁵.

Welding. Oxide ceramics can be joined by welding. A laser or an electron beam is used to heat the edges of the end members above their liquidus temperature. The liquid fills the gap between the materials. This can produce intense local stresses as described previously that can produce cracking during processing or cooling⁵⁸. There is also the possibility of the formation of an undesirable microstructure during the recrystallization of the molten material⁵⁵.

Brazing. Brazing entails the use of a low melting filler between the end members. This is very common in the joining of metals because of the ease of the procedure. When working with advanced ceramics, the use of a low temperature braze material decreases the usefulness of the joined pieces by lowering their maximum use temperature. Other undesirable aspects of brazing are a possible mismatch of thermal expansion coefficients or a chemical reaction between the brazing material and the end member⁵⁵. In the joining process called active metal brazing, these phenomena are controllable and therefore desirable.

Adhesive bonding. This process incorporates the use of an organic adhesive between the ceramic and metal pieces. The organic adhesive is typically flexible compared to the end members. The relative flexibility of the adhesive material can accommodate

stresses that develop between materials with differing thermomechanical properties. Joints made with organic adhesives are usually limited by the strength of the adhesive and the temperature at which the adhesive loses its mechanical integrity. An exceptional example of adhesive bonding is the application of the ceramic insulating tiles to the aluminum skin of the space shuttle.

Hot pressing. Hot pressing is used for both direct and indirect joining. Hot pressing consists of heating the entire assembly to be joined and applying a load at some time during the heating cycle. Direct and indirect joints are both possible using this process. Pressure can be applied either uniaxially, where the end members are usually cylinders, plates or blocks or the pressure can be applied isostatically where any shape can be accommodated. The main limitation of uniaxial hot pressing is the simplicity of the shapes that may be joined. Figure 2-9 represents a typical uniaxial hot pressing setup and the shapes that are most often used. Hot pressing lends itself to the application of diffusion bonding. Diffusion bonding is the formation of a joint through the interdiffusion of two materials with a minimal amount of material deformation. The key requirements to diffusion bonding are 1) intimate contact between the surfaces to be joined and 2) sufficient interdiffusion between the materials being joined to produce a joint in a reasonable time frame. The application of pressure aids in fulfilling both requirements for diffusion bonding. It is a relatively simple matter to hold an assembly as shown in figure 2-9 at the desired temperature and pressure for the extended periods of time that are sometimes necessary for significant diffusion bonding to occur. The isostatic application of pressure is a special case of hot pressing called hot isostatic pressing (HIPing). HIPing allows for application of large pressures and high temperatures. The capital and operational cost of HIPing limits its use to necessary applications.

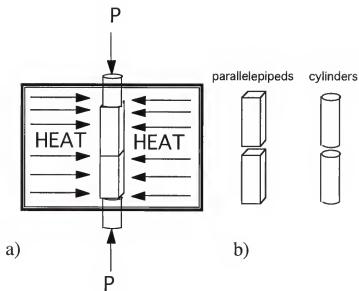


Figure 2-9. Sketches of a) Typical setup used for joining ceramics in a hot press and b) ceramic shapes commonly joined in a hot press.

Criteria for Joining

The joining method of interest in this study is indirect joining through the formation of a diffusion bond. It is now accepted that the mechanisms of mass transfer responsible for joining are the same as those that lead to pressure sintering^{59,60,61,62}. Diffusion and creep mechanisms are responsible for the pore closure that makes up the joining process. These can be grouped most easily by sources and sinks and are illustrated in Figure 2-10. Derby and Wallach⁶², describe the driving forces for each of the mechanisms in Figure 2-10. The driving force for 1 (lattice diffusion) and 2 (vapor transport) is surface curvature and is halted when uniform curvature is achieved. Mechanisms 3 (boundary diffusion) and 4 (surface diffusion) are driven by the chemical potential gradient; 5 (viscous creep) and 6 (dislocation motion) are driven by the applied pressure. The relative importance of each of these mechanisms is determined by the material properties and the time interval required by the joining process of interest.

In diffusion bonding, there are two distinct factors that must be considered for the formation of a good joint. The first factor is the preparation of the surfaces to be joined. For a diffusion bond, it seems reasonable to assume that a mirror smooth surface would be desirable to provide intimate contact between the two surfaces⁶³. Conversely, it also makes sense that a larger contact area provided by a heavily textured surface, figure 2-11, would be conducive to the joining process. The amount of surface texture can be described quantitatively in terms of the ratio of the contact area to the unit area of the surface. The smooth surface in figure 2-11b would have a ratio of one, whereas the textured surface in figure 2-11a would have a ratio greater than one. Villagio⁶⁴ contends that increasing the area of the surfaces to be joined by enlarging the surface profile from a mirror flat finish will increase the contact area and yield the strongest joint. He suggested that sinusoidal shaped surfaces matched together would yield the optimum conditions. The final result is

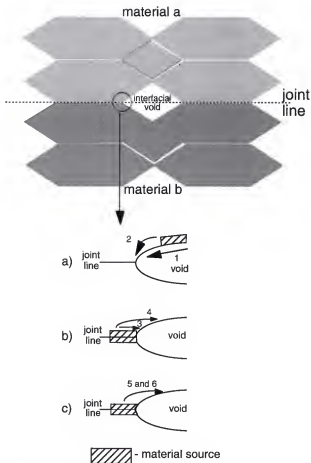


Figure 2-10. Schematic showing the six mechanisms of mass transfer that can lead to joining; a) surface sources, b) bonding interface sources c) bulk deformation after yield or during creep.

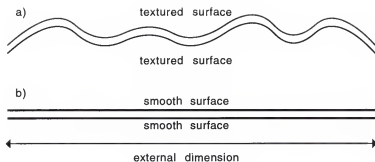


Figure 2-11. Contact area of a) textured surface and b) smooth surface. Contact area in a) is greater than in b) when the external dimension is the same.

a compromise between the two theories that includes a textured surface but not enough to introduce notch stresses at the asperities caused by a reduced area supporting the applied load. The amplitude of the curve suggested by Villagio is small relative to the period of the surface. The ratio of contact area to unit area for the ideal surface discussed by Villagio is only slightly greater than one. In figure 2-12, Suganama et al.⁶⁵ show that an increase in surface roughness of the ceramic decreased the strength of a Si_3N_4 -Al brazed joint. In a review paper, Akselson⁶⁶ suggests that improved joint strengths could have been attained using a higher pressure during processing.

The second factor that must be considered in joint formation is the driving forces responsible for the processes that hold the two pieces together. The impetus for joining can be in the form of van der Waals forces or with an electronic structure across the interface⁵⁵. The goal of all of these mechanisms working together is to reduce the free energy of the system by eliminating the free surface.

Effect of Process Variables on Joining

Temperature

The mechanisms that control joining involve either diffusion or plastic deformation. For the mechanisms that are diffusional, temperature is the most influential variable in the joining process. This is explained by the presence of temperature in the exponent of the diffusion equation. However, the maximum temperature for diffusion bonding is limited to a fraction of the melting temperature of the material to be joined. Akselson⁶⁶ reports the temperature range for sufficient joining to be 0.5-0.8 of the lowest melting point of the materials to be joined. Higher temperatures would lead to excessive creep deformation of the specimen. Crispin and Nicholas⁶⁷ calculated the bond strength of a steel/alumina joint with an aluminum interlayer as a function of temperature. Figure 2-13 plots these values and compares them with values measured between 0.75-0.95 of the melting temperature of

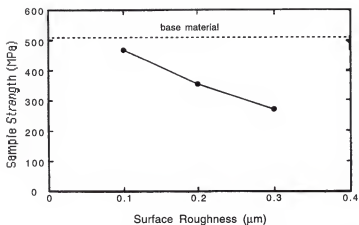


Figure 2-12. Effect of surface roughness (as described in equation 3-1 and figure 3-4) on sample strength⁶⁵.

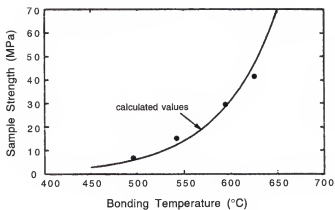


Figure 2-13. Effect of joining temperature on the strength of a joint⁶⁷.

aluminum. Derby and Wallach⁶² review the role of temperature in each of the mechanisms in figure 2-10.

Pressure

The application of pressure during diffusion bonding has the effect of increasing the intimate contact between the surfaces to be joined. When the joining temperature has been attained, the application of pressure assists in deformation near the joint surface that results in the closure of voids at the interface⁶². As reported by Allen and Borbidge⁶⁸ in figure 2-14, at low applied pressures an increase in pressure greatly increases the bond strength. This effect is diminished as the applied pressure is increased. This indicates that there may be, for each joint, an optimum pressure where the greatest benefit of increased bond strength can be realized without significant deleterious deformation of the original materials⁶⁹.

Time

The solid-state joining process of interest is diffusion controlled. The effect of time on the strength of a joint is similar to that of time on atomic diffusion⁶⁶. The well-known equation for diffusion as a function of time is

$$X = k(Dt)^n \quad (2-9)$$

where X is the distance traveled by the diffusing species, k is a constant, D is the diffusion coefficient and the exponent, n, is usually 0.5. The analogous expression

$$BS = B_0 t^{\frac{1}{2}} \quad (2-10)$$

where BS is the bond strength, and B_0 is a constant was developed by Crispin and Nicholas⁶⁷. The equation relates the joining time to the bond strength. Figure 2-15 shows the effect of bonding time on the strength of an Al_2O_3 -Al joint. This equation and plot

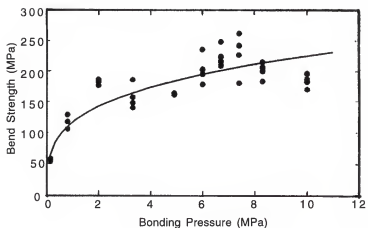


Figure 2-14. The effect of pressure applied during joining on the strength of the joint⁶⁸.

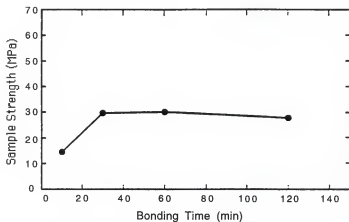


Figure 2-15. The effect of joining time on the strength of the joint⁶⁷.

assume that there is no chemical reaction in the form of a phase change associated with the joining process.

Reactions

While not strictly process variables, reactions in and between the end members and the interlayer may have a significant effect on the quality of the joint and the bond strength. In metal/ceramic joining, there is the possibility of controlling the interfacial reactions. Loehman and Tomsia⁶⁰ compared results from two different investigations of the strength of Nb-Al₂O₃ joined in a vacuum. They discovered that the formation of a reaction layer reported by one set of authors agreed with theoretical prediction based on thermodynamics, while reports by other researches yielded contradictory results. Loehman and Tomsia suggest⁶⁰ that these contradictions can be attributed to a difference in the oxygen partial pressure during processing.

Scales of Joining

Joining can be described on a variety of scales. When two materials are joined chemically, the interactions are typically discussed considering only the scale of interest. That is, when the matching of crystal lattices is the topic, it would be discussed on a nano or atomic scale and the macro and micro scales would not be considered. Figure 2-16 illustrates the four scales of joining that are referred to most often.

Atomic

On the atomic scale, joining can be thought of as interatomic bonding. This can be illustrated by looking at adjoining atoms from the two surfaces. In the case of most metal oxides, the interatomic bond is largely ionic. Kingery et al.⁷⁰ state that as two oppositely charged ions approach one another, the molecule becomes more stable. The energy of attraction is due to the coulombic forces that arise between the oppositely charged ions.

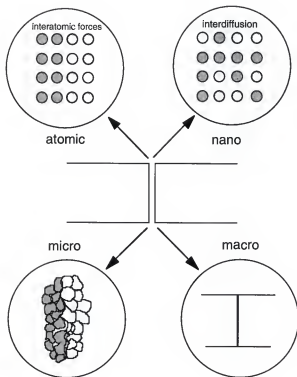


Figure 2-16. Graphic representation of the four scales of joining discussed in the text.

The increase in stability continues until the electron shells associated with the two ions overlap.

As described in the Pauli exclusion principle, only one electron is allowed for each quantum state. As two ions approach each other, a strong repulsive force arises to work against the coulombic attractive force. The combination of these two forces leads to an energy minimum in an energy versus separation diagram, Figure 2-17. Ferrante et al.⁷¹ identify this energy minimum as the binding energy. The authors also state that the derivative of figure 2-17 is the force versus separation curve, figure 2-18, and that the maximum can be considered in simplest terms as the tensile stress ($F_{\max}/A_{\text{surface}}$) necessary to separate the two ions.

Nano

In the next largest scale examined, the first few atomic planes of each surface are considered. Ferrante et al.⁷¹ discuss the difficulties in increasing the scale in the theoretical evaluations. They note deviations from symmetry that muddles the theoretical approach. Some of these deviations are caused by the use of two different planes of the same material or the existence of two different materials in proximity. To simplify this problem, Clarke and Wolf⁷² reduce the interface to a Van der Waals pair potential and sum the potentials over the interface. This can be used for ceramics when the bonding is localized. Metals require another approach that is more complicated and will not be discussed in this dissertation. Stoneham and Tasker⁷³ employed computer codes to model the interfaces between materials. In the evaluation of the BaO/NiO interface, the authors matched surfaces by rotating the 100 planes by 45°. The resulting relaxed structure, figure 2-19, placed the Ni³⁺ ion and vacancies from the disordered NiO lattice near the BaO surface. This is depicted as the lowest energy structure. Unfortunately, the authors do not consider any interdiffusion of the cations in their model.

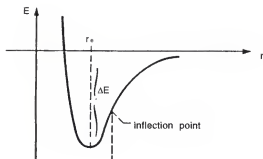


Figure 2-17. Energy versus separation for two ions in proximity to each other⁷¹.

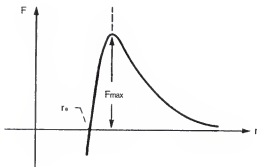


Figure 2-18. Force versus separation for the two ions in figure 2-17⁷¹.

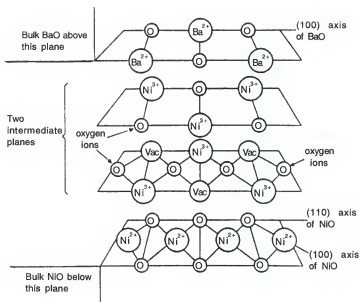


Figure 2-19. Computer derived, relaxed structure of the BaO/NiO interface⁷³.

Micro

Joining on a micro scale can be reviewed in two ways. The most common way to consider joining is by bringing together two distinct pieces of material. If the pieces are determined to be joined, at some position in both materials there will be a deviation in composition and/or structure. If the joining is done properly, the joint may be indistinguishable from the bulk to the naked eye. Optical or electron microscopes may be required to locate the position of the joint. Usually, the area where the initial surfaces contact can be easily identified. Binner et al.⁷⁴ recently reported grain growth across the initial interface, making it difficult to recognize. Al-Assafi⁷⁵ joined alumina of two different purities using an alumina gel as an interlayer. The original interface was indistinguishable from either end member. Backscatter electron microscopy was used to determine the original interface by identifying the silica impurities in the two types of alumina. Another feature associated with the micro scale of joining is the possible observation of porosity. When joining fully dense end members, porosity can appear at the original interface. This usually has a negative effect on the strength of the joint. The micro scale is also where interdiffusion across the interface can be detected and measured. This can be done with backscatter electron spectroscopy (BES), Secondary Ion Mass Spectroscopy (SIMS)⁵¹ or with electron microprobe analysis (EMPA)⁷⁶.

A second way to envision joining on a micro scale is to consider sintering. Sintering is the joining of many smaller particles to each other to form a large mass. Solid state sintering is analogous to joining via diffusion bonding. As discussed earlier, the mechanisms for joining are based upon those developed for sintering. The end members could be considered as grains and the joint line would represent a grain boundary.

Macro

In this paper, the macro scale is considered to encompass those aspects of the joint that can be seen with the unaided eye. The features of a joint that can be discussed on a macro scale include poorly formed joints, interlayers, reaction products and abrupt discontinuities when materials of differing colors are used. When a joint is not fully developed, the original interface is apparent because the edges of the end members still contain porosity. Interlayers are almost always a different material from the end members. Even when the joint is well made, the presence of an interlayer makes joint identification fairly routine. In the situation where there is a reaction product, such as the joining of alumina and nickel oxide to form a spinel, the color change provides a good indication of the extent of the reaction.

Materials Joining

The joining of materials has attracted the interest of a growing number of researchers. There is vast potential in the joining industry to improve the properties of joined components. However, there are many theoretical and experimental issues regarding the joining process that must be addressed if the industry is to fulfill its potential. Some of the theoretical aspects of the joining process have been discussed previously in this dissertation. A recent focal point has been the effect of the use of an interlayer on the stresses developed in the final piece during joining⁷⁷. Experimental work is being performed on several elements of the joining process. This includes the development of new methods for evaluating joint strength and new ways of joining materials. The joining field includes laminar composites that consist of polymer/metal or ceramic/metal bonding, and the more common butt joints of metal/metal, metal/ceramic, ceramic/metal/ceramic and ceramic/ceramic. The most recent addition to the joining field is the functionally graded interface (FGI). The functionally graded interface can be applied to any of the above mentioned methods of joining. The joint consists of a gradual compositional variation from

one surface to the other (e.g. concentration and/or porosity). These changes result in property gradients (e.g. strength, mechanical toughness or thermal expansion coefficients), which can be adjusted by controlling the composition and/or the microstructure of the interlayer.

Metal/ceramic joining

The metal/ceramic joint is present in two different situations. In one instance, it is an element of the design of the component. This enables the exploitation of the properties of both metals and ceramics. One example, mentioned earlier, is the case of a light bulb. The metal base is electrically conductive and permits current flow to the filament with a minimum of resistance. The ceramic component, a glass envelope, is transparent to the visible light emitted by the filament. Joined together to form a vacuum seal, they provide a package that would be difficult to imitate using only a metal or a ceramic. The other instance of metal/ceramic joining occurs when it is necessary to join two ceramic pieces using a metal interlayer. A common example of this is in high-temperature structural applications. Under these circumstances, the high-temperature strength and refractory properties of ceramics are desired. High melting point metals such as titanium are used as interlayers when brazing ceramics for high-temperature applications. The brazing process is used because it requires a minimum amount of metal. Increased metal content may detract from the desired behavior of the ceramics.

Alumina is the most common ceramic material to be studied in metal/ceramic joining. Perhaps this can be attributed to its popularity as a structural material, as well as the wealth of information available on its thermodynamic and mechanical properties. Routine polishing of the surface is the only treatment the ceramic piece receives prior to joining. Conversely, the metals are carefully prepared from high purity materials and meticulously cleaned and polished before these are used. When the joint is to be formed via diffusion bonding, several different metals of varying thickness are used^{78,79}. Usually

the added metallic layers are very thin and have a low melting temperature and elastic modulus compared to either the ceramic or the primary metal. This correlates with several thermal stress reduction methods in metal/ceramic joining discussed by Suga et al⁸⁰. Ishida et al.⁸¹ relieved thermal stresses via the introduction of structural defects. This was accomplished by orienting the lattice when joining single crystals of niobium and alumina. Serier and Treheux⁸² increased the strength of a silver/alumina joint by work hardening the silver. They offer several hypotheses for the increase in strength, including the inducement of structural defects. Frequently, the methods described above are not practical for service operations, and the formation of a liquid phase at the joining temperature is necessary to form a good joint.

Ceramic/ceramic

In 1979, Hauth⁸³ noted that several emerging technologies have high-temperature use specifications for materials that will require ceramic/ceramic joining without the aid of a metal interlayer. The example referred to was a high purity alumina pumpout port for a thermonuclear fusion containment system. The pumpout port is a complex shape that is comprised of several regular shapes (cylinders and plates) fitted together. The joining method consisted of making a slurry of the unsintered material and buttering (as with toast) the surfaces to be joined. This is the same procedure for attaching cup handles and other extremities in the clay based ceramic industry. In the years since, numerous advances have been made in ceramic/ceramic joining but there are still many hurdles to be overcome.

In the direct joining of similar ceramic materials, some chemical or physical variation must be present to assist the driving forces that make up the joining process. Scott and Brewer⁸⁴ diffusion bonded alumina at 1500°C and 69 MPa. The joined pieces were then heated to 1875°C to promote grain growth across the joint. They reported a maximum joining strength of 59% of the starting material. This was achieved with an axial

deformation of 18% during joining. In similar experiments⁸⁵, small amounts of MgO were added as a sintering aid to the alumina cylinders to be joined. The joining temperatures ranged between 1300°C and 1500°C with a pressure of 69 MPa. Deformation increased to over 20% and no mechanical testing results were reported. Zdaniewski and Kirchner⁸⁶ inserted thin polystyrene sheets between 96% alumina plates. The decomposition of the polystyrene during heating created reducing conditions that enhanced interfacial bonding and diffusion. In specimens joined at 1350°C and 17.5 MPa, the authors reported flexural strengths of 194±94 MPa. Direct joining has also been investigated for SiC and Si₃N₄ with modest success^{87,88}.

When the need for an indistinguishable joint is not imperative, there are more straightforward ways of joining ceramics for high temperature use. Zimmer⁸⁹ describes the development of several ceramic cements that can withstand high temperatures (>1450°C). Glass or glass-ceramics are also popular choices as interlayer materials. Whereas some authors^{90,91} chose glasses for their mechanical properties and crystallization abilities, other researchers^{92,93} chose an interlayer glass composition that approximated the composition of the grain boundary phase of the crystalline end members. When the glass was chosen for its crystallization ability, joints of modest flexural strength and fracture toughness were produced. Both groups of investigators who joined Si₃N₄ with a glass similar to the grain boundary phase reported room temperature strengths of 450 MPa.

Microwave Joining

Microwave joining of materials appears to be one of the most promising among the areas of materials processing that have been included in microwave processing research. Researchers have successfully joined alumina, silicon carbide, silicon nitride and mullite⁹⁴⁻¹⁰⁰. With the exception of a few studies, most of the work has been performed using single mode microwave applicators. The first report of joining ceramics using microwaves

was by Meek and Blake³. They successfully joined two alumina plates with a glass interlayer in a home model microwave oven. Palaith et al.⁹⁴ provide an overview of the fundamentals of microwave heating and how it applies to joining. Using a tunable, single mode microwave oven modified to allow for an application of pressure, Fukushima et al.⁹⁵ joined several different purities of alumina and silicon nitride. Specimens consisted of cylindrical rods measuring three millimeters in diameter. The alumina purities varied from 92% to 99%. Joining experiments were conducted at temperatures ranging from 1400°C to 1850°C and pressures up to 2.4 MPa. The authors were able to produce direct joints using 92% and 96% alumina that approached the original strength of the material. Figure 2-20 is the effect of joining temperature on the bending strength of the 92% alumina. The 99% alumina was successfully joined indirectly using both the 92% and the 96% alumina as interlayers. Bending strengths of 90% of the original material were reported. No information was provided regarding creep deformation. However, even at the low joining pressures used, the temperature was high enough for creep to occur in high-purity alumina. The same authors joined silicon nitride in a flowing nitrogen atmosphere using silicon nitride with a greater dielectric loss than the end member material. The effect of joining time on the bending strength of the joined silicon nitride is shown in figure 2-21. Al-Assafi and Clark⁹⁶ successfully joined 94% alumina to 99.5% alumina using a sol-gel-derived alumina as the interlayer. The researchers used a multimode cavity and microwave hybrid heating. Figure 2-22 is the Knoop hardness across the joint area for joints made with and without the gel interlayer. The purpose of the gel interlayer is to provide a high-purity powder with a large surface area to join the two surfaces. In an effort to evaluate the joint non-destructively during processing, Palaith and Silbergli⁹⁷ introduced an apparatus that provides an acoustic pulse echo axially through the sample during joining. This provides information as to the extent of the joint formation. Figure 2-23 is the result

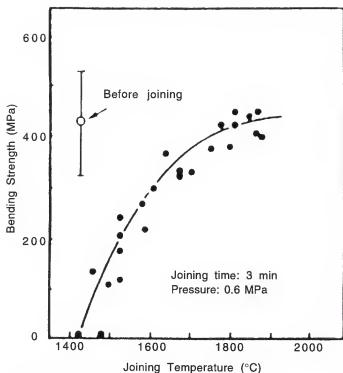


Figure 2-20. Effect of joining temperature on the strength of 92% alumina⁹⁵.

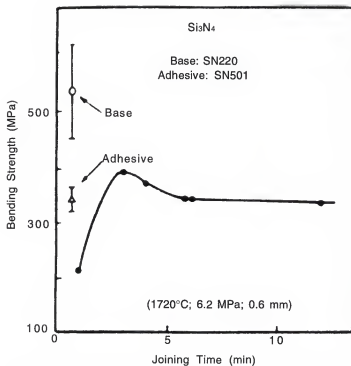


Figure 2-21. The effect of joining time on bend strength of silicon nitride⁹⁵.

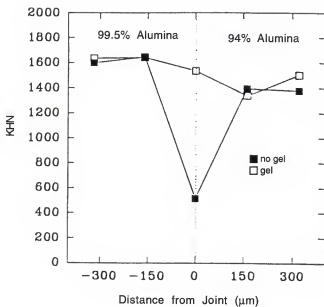


Figure 2-22. Knoop hardness across joint for microwave joined alumina⁹⁶.

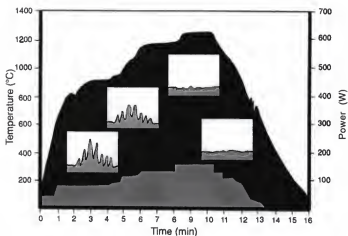


Figure 2-23. Acoustic emission traces for a mullite joining experiment⁹⁷.

of an experiment involving the joining of mullite. Yu et al.⁹⁸ employed this method in the simultaneous sintering and joining of alumina powders. At a temperature of 1400°C and a pressure of 0.238 MPa, they achieved a density of 99% theoretical.

Silicon carbide is an excellent microwave absorber and a ceramic material that has many potential uses. Therefore, it has attracted the bulk of attention for microwave joining. The processing of the silicon carbide, whether it is reaction bonded silicon carbide or hot pressed silicon carbide, can significantly affect its ability to absorb microwaves. Reaction bonded silicon carbide contains residual silicon metal throughout the microstructure. Ahmad et al.⁹⁹ direct joined hot pressed silicon carbide to hot pressed silicon carbide and to reaction bonded silicon carbide. They accomplished this using both a single mode microwave and a multimode microwave oven. Yin et al.¹⁰⁰ joined the high dielectric loss siliconized silicon carbide using a thin aluminum foil as an interlayer. The authors achieved fracture strengths comparable to the original material. Other attempts to join silicon carbide include the use of combustion synthesis. It has been demonstrated that microwaves are an excellent source of energy for initiating and controlling the combustion synthesis reaction¹⁰¹. Silbergliitt et al.¹⁰² made successful SiC/SiC joints by initiating a combustion reaction between titanium, silicon and carbon at the interface.

In an overview paper discussing the problems and opportunities in microwave joining, Loehman¹⁰³ states that there are applications that hold promise but much work needs to be done to prove the value of microwave joining. He discusses potential advantages that could be realized by applying microwave processing to the joining of ceramics. The author also identifies problems that may be encountered and offers solutions through rigid process control.

Summary

Several authors^{104,105} have discussed the potential for energy savings through the use of microwave processing. It still is not clear if there is a significant energy conservation to be realized. Katz¹⁰⁶, regardless of his involvement as a researcher in the field of microwaves, displayed a skepticism towards many of the positive results being published regarding microwave processing. Despite a wary community of researchers, exploration of microwave processing has continued with success in specific areas. One promising niche involves the recovery of common and precious metals from electronic circuit boards¹⁰⁷. Microwaves also have proved successful in several industrial applications¹⁰⁸. They are currently being used in some areas of food processing, rubber vulcanization and wood curing.

Research in the microwave joining of ceramics is developing into a field that will have viable approaches to engineering problems. Microwave joining has proved feasible for several oxide and non-oxide ceramics. These materials can be joined with strengths at or above those attained on conventional joining processes. Some of the advantages that have been demonstrated by researchers include the ability to join materials with unfinished surfaces (large surface roughness) as well as non-destructive evaluation of the joint during the joining process. The in-situ joint evaluation can be performed because it is possible for the end members to extend out of the heating zone. This provides access to the end members for the acoustical equipment. In the brief period of time that microwave joining has been investigated, many discoveries have been made that have led to further research. Much of the work reported has been presented in one of two formats. In the first method, the strength of a joint formed under specific conditions is presented with reference to the strength of the original material. The second method is somewhat more informative in that the results are compared to conventional joining of similar materials under comparable

conditions. The consequences of changing the processing parameters have not yet been investigated. Results need to be evaluated in a more scientific manner than plotting strength versus the processing parameter (temperature, pressure, etc.). These parameters need to be evaluated to determine their relative importance in microwave joining. **The intent of this research was to provide reproducible, microwave joining data based upon an experimental design coupled with numerical modeling of the experiment. The data generated will contribute to the advancement of microwave joining of materials by assisting in clarifying the effects of some of the processing parameters on the joined materials.**

CHAPTER 3

MATERIALS AND METHODS

There are several objectives encompassed by the experimental procedure. The first objective was to choose a system of materials, consisting of end members and an interlayer, that was of technical interest and could be joined successfully using microwave energy. The second objective was to develop a device and procedure that could fabricate joined specimens with reproducible properties. The first two objectives were incorporated into the third objective to manufacture joined specimens that were tested for flexure strength. These results then were analyzed to evaluate the relative importance of the processing parameters on the strength of the joined specimens. A fourth objective of this chapter was to monitor the temperature of the specimen and the susceptor during joining so comparisons could be made to the numerically derived temperature profiles discussed in the next chapter. The experimental work performed in this study can be separated into four phases.

The first phase of the work was the preliminary testing of potential interlayer materials. Various properties of several materials were tested to determine which materials possess the characteristics required to produce a strong joint. The material properties of greatest interest were the mechanical strength, refractoriness and microwave absorbing capabilities. The results reported by Al-Assafi⁷⁵ indicate that an alumina based sol-gel was an excellent candidate to provide the desired characteristics.

The second phase consisted of designing and implementing a microwave joining device to control and record the processing parameters. A microwave susceptor was

developed to heat the end members to a temperature at which they become more efficient microwave absorbers. Using the materials that were classified as tenable interlayers, experiments to join two viable end member materials were initiated. Flexure bars were machined from the joined specimens and tested using four-point bending to evaluate the interlayer and end member materials based on strength.

Phase three was the development of an experimental design that would use the chosen materials system to evaluate the significance of each of the processing parameters on the flexure strength of the joined material. Two values were selected for each processing parameter and an analysis of variances was performed on the results of the flexure tests.

In phase four, a heat transfer program was used to simulate microwave hybrid heating. The results were compared to measured values collected in experiments run to measure the temperature of the specimen and of the susceptor. Two methods of temperature measurement were used to test the validity of the measuring process.

Phase One

The materials that were identified as potential interlayers were a series of alumina based gels, 96% pure alumina and nickel oxide. The alumina gel used by Al-Assafi was investigated as an interlayer material. It also served as a base gel that was combined with other materials. The other materials were introduced to the base gel either by substituting for the aluminum salt in the gel during formation or by admixing them to the stable sol before gelation. All of the materials added to the base gel were considered to be strong microwave absorbers. The intent of this approach was to increase the absorption of microwave energy in the joint area. All of the joining experiments in this study were performed in a constantly changing microwave field. Therefore, unlike the single mode applicator used by Fukushima et al.⁹⁵, there were no fixed positions where a high electric

field was present. Due to these processing conditions, there was no technique available to determine the position of a stable hot spot as described by Booty and Kriegsmann³⁹.

Five materials (chromium oxide, iron (II) oxide, iron (III) oxide, nickel oxide and silicon carbide) were used in conjunction with the base gel to make ceramic powders for subsequent evaluation. These materials were selected from a myriad of strong microwave absorbers because of the way they combine with alumina. Chromium oxide is mutually soluble in alumina for an entire range of compositions. Iron (III) oxide also forms a solid solution with alumina, but each material is capable of dissolving around 10% of the other. Iron (II) oxide and nickel oxide both form a spinel when combined with alumina. Silicon carbide does not form any intermediate compounds with alumina.

Thin monolithic disks of 96% pure alumina and of nickel oxide also were examined as potential interlayer materials. Alumina was considered because it is very similar to the materials being used as end members: 99.5% and 96% alumina. Using a similar material as the interlayer reduces the risk of stresses from differential expansion and maintains a high strength material throughout the joint region. However, the similarity in composition presents a challenge to joining because it reduces the presence of a compositional gradient to act as a driving force. Nickel oxide was chosen over iron (II) oxide as the second solid material because it is less sensitive than iron (II) oxide to oxygen partial pressures.

Sol-Gel

Base gel

The alumina based sol-gel interlayer was produced in accordance with a patent by Clark et al.¹⁰⁹ for the creation of boehmite sols. The materials used to produce the base gel are water*, aluminum sec-butoxide**, and aluminum nitrate nonahydrate***. The

* Deionized water - resistance > 10 Mohms

** Alpha Chemicals # 11140 - $\text{Al}(\text{OC}_4\text{H}_9)_3$ F.W. 246.33

*** Fisher Chemicals # A586-500 - $\text{Al}(\text{NO}_3)_3 \cdot 9\text{H}_2\text{O}$ F.W. 375.14

purpose of the aluminum sec-butoxide is to provide the solution with metal ions. The water hydrolyzes the aluminum sec-butoxide. Aluminum nitrate nonahydrate is a peptizing agent that breaks up the precursor, permitting the hydrolysis to occur. This facilitates the formation of colloidal aluminum hydroxide particles. Throughout the remainder of this thesis, aluminum sec-butoxide will be referred to as ASB, and aluminum nitrate nonahydrate will be referred to as aluminum nitrate. Working within the parameters established by the patent, Dalzell¹¹⁰ reported a ratio of ASB:aluminum nitrate of 25:1 as providing a stable sol. The ratio of 25:1 ASB:peptizer was used throughout the course of this study. The ratios of the three components for the initial sol were 100:1:0.04 corresponding to water:ASB:aluminum nitrate.

Under reflux conditions, 675 milliliters of deionized water was heated to 88°C in a 1000 milliliter Pyrex flask that had been washed in a 6M nitric acid/0.2M hydrofluoric acid solution and rinsed in deionized water. During heating the water was stirred continuously by a Teflon coated magnet. Meanwhile, six grams of aluminum nitrate was dissolved in 45 milliliters of water. Rapidly, 104 milliliters of ASB was measured to minimize hydrolysis of the ASB from the air. The ASB then was added to the water using two syringes*. The aluminum nitrate solution then was immediately added to the flask. The result was a cloudy, milky-white solution. This was stirred continuously until it became translucent. The clearing process took several hours. After the sol cleared, it was cooled to room temperature and stored in a polypropylene container until used.

Doped gel

According to the patent by Clark et al.¹⁰⁹, several other metal nitrate salts may be substituted for aluminum nitrate during the sol-gel process. Both chromium nitrate** and

*Fisher Chemicals # 14-823-2D - 60 ml syringes

**Fisher Chemicals # C331-500 Cr(NO₃)₃·9H₂O F.W. 400.15

iron (III) nitrate* can replace aluminum nitrate in the sol. Chromium oxide forms a solid solution with alumina at every composition. Figure 3-1 is the binary $\text{Al}_2\text{O}_3\text{-Cr}_2\text{O}_3$ phase diagram at elevated temperatures. The $\text{Al}_2\text{O}_3\text{-Fe}_2\text{O}_3$ phase diagram, figure 3-2, is more complex. Below 1300°C , there is a mixture of the Fe_2O_3 (hematite) phase solid solution with Al_2O_3 and Al_2O_3 (corundum) phase solid solution with Fe_2O_3 . Near 1400°C , the presence of FeO becomes significant as the spinel, FeAl_2O_4 , is formed. McGill et al.¹¹¹ reported that both chromium oxide and iron (III) oxide are excellent microwave absorbers in the temperature range investigated at the frequency of 2.45 GHz. The other additives, silicon carbide**, nickel oxide*** and iron (II) oxide****, were admixed as powders into an alumina sol and reduced to a solid. The yield of the sol was determined in two ways. In the direct method, 200 milliliters of sol was dried and then heated to 1200°C . This temperature was above the crystallization temperature of the stable α -alumina phase. X-ray diffraction analysis confirmed that the alpha phase was the only phase present in detectable amounts. The resulting powder was weighed and had a mass of 5.08 grams. The yield of the sols was also determined mathematically. Using the ratios of materials stated earlier, calculations were made based on using 100 moles of water, one mol of ASB and 0.04 moles of aluminum nitrate. This would provide 1.04 moles of aluminum available for oxide formation. This, in turn, would produce 0.52 moles of alumina which represents a mass of 53 grams of alumina. By calculating the volume of the resulting sol, a yield of 0.026 grams of alumina per milliliter of sol was determined. For a 200 milliliter

*Fisher Chemicals # I110-500 $\text{Fe}(\text{NO}_3)_3 \cdot 9\text{H}_2\text{O}$ F.W.

**Norton Company SiC E-85 Crystolon 220 grit F.W. 40.1

***Fisher Chemicals # N69-500 NiO F.W. 74.71

****Fisher Chemicals # I119-500 FeO F.W. 231.54

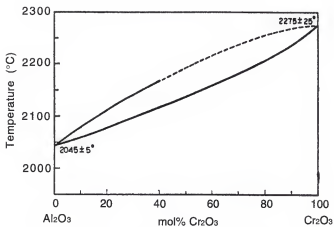


Figure 3-1. Binary Cr_2O_3 - Al_2O_3 phase diagram¹¹².

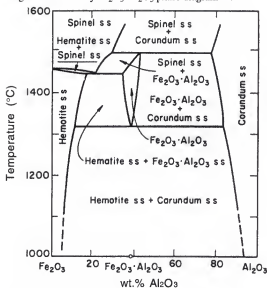


Figure 3-2. Binary Fe_2O_3 - Al_2O_3 phase diagram¹¹³.

sol, this renders 5.12 grams of alumina -- a difference of less than one percent from the experimentally determined value.

The powders were added to sols in a 1:1 molar ratio with the expected yield of alumina. The mixture then was ultrasonicated for ten minutes to break up agglomerates. The sol/powder mixture then was gently heated on a hot plate while stirring until much of the liquid was removed. The resulting gel was heated overnight at 150 °C to remove most of the remaining liquid. The end result was a solid mass of opaque material. This was crushed in a mortar and pestle and sieved through a 325 mesh (44µm) screen. Using a 1.2 centimeter diameter steel die, 1.5 grams of each powder were pressed into pellets using a 13.3 kN force.

Sol-Gel Characterization

The gels produced were characterized using several diverse methods. The different compositions of pellets were heated using microwave energy at 2.45 GHz to evaluate each as a microwave absorber. Differential scanning calorimetry (DSC) was performed on the various compositions with x-ray diffraction analysis conducted on the resulting material. Dielectric properties of the different compositions were measured at 2.45 GHz as a function of temperature.

Stand alone heating

A home-style microwave oven* was fitted with an on/off temperature controller. An inconel-shielded, Type-K thermocouple was placed in contact with the specimen for temperature measurement within the microwave. Refractory brick** was sculpted to accommodate a specimen and a thermocouple feedthrough. The brick provides insulation to reduce heat loss from the specimen during heating. The setup in Figure 3-3 has a

*General Electric 750 Watt Dual Wave II Microwave System

**Thermal Ceramics K-3000 3000°F refractory brick

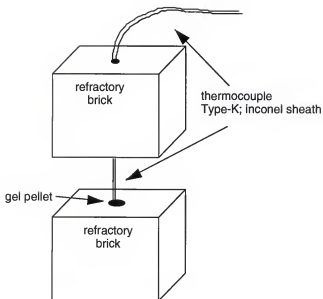


Figure 3-3. Setup used to measure temperature of gel compositions heated solely by microwaves (setup was placed in a microwave for heating).

maximum test temperature of 1175 °C. Specimens were heated at full power (800 W) using the setup in Figure 3-3. Temperature readings were taken periodically. Initial results may have been influenced by arcing between the thermocouple and the specimen. Arcing is the release of a charge build up between two points which can cause localized heating and even melting of the thermocouple and the specimen. Another problem associated with arcing is inaccurate, widely varied temperature readings. One way in which arcing was reduced was by increasing the surface area of the tip of the thermocouple. In this case, a thin nickel disk was placed between the thermocouple tip and the specimen. This significantly reduced the amount of arcing encountered during the study.

Differential scanning calorimetry

Differential scanning calorimetry was performed on a Stanton Redcroft DSC 1500S. The gels were heated from room temperature to 1400°C at ten degrees per minute in flowing air. A second experiment was conducted on the sample containing FeO. This time, the maximum temperature was 1250°C in order to avoid any reactions that occur above 1250°C. A piece of sapphire, similar in mass to the sample powder, was used as a reference material to maintain a level baseline.

X-ray diffraction analysis

The ceramic powders that resulted from heating in the DSC were subsequently analyzed using a Scintag X-Ray Diffraction Analyzer. The x-rays were copper k-alpha at 45 kilovolts and 40 milliamps at a wavelength of 1.54060 angstroms. The powders were scanned at one degree 2 θ per minute from twenty to sixty degrees 2 θ . This 2 θ range was sufficient to identify any of the compounds formed during heating that involved any of the materials used.

Dielectric properties

The relative dielectric constant and loss factor, ϵ'_r and ϵ''_{eff} , were measured for several compositions of the dried powder at 2.45 GHz as a function of temperature. Before analysis, the powders were heated to 450°C to remove all of the bound and structural water. This was done to provide the instrument with a relatively constant mass of material. The dielectric properties were measured from room temperature up to 1400°C. These measurements were performed at Chalk River Laboratories/Atomic Energy of Canada, Ltd. using the cavity perturbation method*.

Alumina

The two purities of alumina used as an interlayer material were Coors AD94, 94% alumina and Coors AD96, 96% alumina. The major impurities in all of the Coors alumina products are silica, magnesia and calcia. These impurities act as fluxes for densification and as grain-growth inhibitors. The manufacturer reports a room temperature flexure strength for the AD94 of 350 MPa. The grain size ranges from 2-25 microns with an average grain size of 12 microns. Other relevant properties of the alumina are in Table 3-1. The interlayers were produced by cutting disks approximately 2 millimeters thick from a cylindrical rod 2.54 ± 0.0025 centimeters in diameter and 20.32 ± 0.0025 centimeters long. The disks were mounted on a glass plate and the surfaces were machined using a high speed diamond grinding wheel**. The machining procedure used a downfeed of five microns per pass and a crossfeed of 2.5 millimeters. The disks had a final thickness of 1.5 ± 0.15 millimeters.

*R. Hutcheon AECL Chalk River Laboratories, Chalk River, Ontario, CA

**Norton ASD320-R75B99-1/4 320 grit wheel

Table 3-1. Manufacturer Reported Properties of Coors Alumina Used in Study.

Property		Units	AD-94+	AD-96+	AD-995+
Specific Gravity			3.62	3.72	3.84
Crystal Size	range average	microns	2-25 12	2-20 11	10-50 20
Flexural Strength	25°C 1000°C	MPa	350 140	359 172	310 230
Modulus of Elasticity		GPa	282	303	358
Shear Modulus		GPa	117	124	152
Bulk Modulus		GPa	166	173	207
Poisson's Ratio			0.21	0.21	0.21
Maximum Use (no load) Temperature		°C	1700	1700	1,750
Thermal Conductivity	25°C 100°C 400°C 800°C	W/m·K	18.0 14.6 7.1 4.2	18.0 14.6 7.1 4.2	31.4 27.2 11.7 7.1
Specific Heat	100°C	J/K(kg)	880	880	880
Dielectric Constant	25°C 500°C 1 GHz 800°C	ratio	8.9 - - -	8.9 - - -	9.4 10.4 11.0
Dielectric Loss Factor	25°C 500°C 1 GHz 800°C	ratio	0.0008 - - -	0.0001 - - -	0.0001 0.0002 0.0003
Loss Tangent (tan δ)	25°C 500°C 1 GHz 800°C	ϵ''/ϵ'	0.007 - - -	0.001 - - -	0.001 0.002 0.003

*Coors Alumina and Beryllia Properties Handbook, Bulletin 952, Coors Ceramics, (1969)
Nickel Oxide

High-purity nickel oxide disks, hot pressed to >80% dense, were obtained from Super Conductor Materials, Inc. The as-received disks were 2.5 centimeters in diameter and 1.2 centimeters thick. The surface of the disks were impregnated with a graphite

residue from the manufacturing process. A low speed wafering saw was used to section the disks into thinner pieces. As with the alumina interlayer specimens, the nickel oxide disks were mounted on a glass plate and machined to a thickness of 0.33 ± 0.02 millimeters. All of the graphite was removed during the grinding step.

Surface roughness

The machined surfaces were characterized using a laser profilometer*. A 3-dimensional scan was performed on a five millimeter by five millimeter square section of the surface. A total of 250 line scans were performed on each material. The table speed was 10 mm/minute. The average surface roughness was calculated from a single scan using the same distance and table speed as the 3-dimensional scans. The roughness reported is the deviation from the arithmetic mean and was calculated automatically from the profiles using the equation

$$R_a = \frac{1}{l} \int_0^l |y(x)| dx. \quad (3-1)$$

Figure 3-4 illustrates the arithmetic mean in a simulated profile and identifies the components of equation 3-1 that are used to compute the surface roughness.

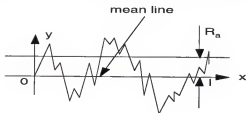


Figure 3-4. Simulated material profile depicting the arithmetic mean.

*Rodenstock RM-600 Laser Profilometer

Phase Two

Currently, there are no commercially available systems to perform the microwave joining of ceramics. Therefore, an apparatus had to be designed and constructed to accomplish this task. The modification of a microwave oven to accommodate the application of pressure has many challenges associated with it. Turntables or fans used to stir the microwave field may interfere with the application of pressure and must be removed or repositioned. The external holes needed to apply a load on a specimen in the microwave cavity are a breach of the microwave containment system and present a potential health problem (see equation 2-5). Extreme care must be taken in the design and fabrication of the joining apparatus to address these challenges and prevent them from hindering the joining experiments.

There are several reasons why alumina was chosen as the material of interest for this study. Alumina is one of the most widely used technical ceramics. It is prominent as a substrate for electronic materials, as a refractory material, and as a structural ceramic. Although alumina is not always the ideal material for the intended use, it is often chosen because of its low cost. The thermal or mechanical properties of alumina are also considered acceptable for many applications when the ideal material is either unavailable or too costly. Alumina can be obtained in a multitude of purities, grades and sizes designed to meet most of the needs of the technical community. Another predominant reason for selecting alumina for this study is that it is a common material for testing and analysis. There is an abundance of documentation available detailing its properties and performance under widespread conditions. This includes the thermal, electrical, optical and mechanical behavior upon exposure to elevated temperatures.

The end members considered for the joining experiments, 99.5% and 96% pure alumina, are both poor microwave absorbers compared with the materials being surveyed

as potential interlayers. Without assistance, the end members are unable to heat to the temperature required for joining using the microwave oven designated for this study. Microwave hybrid heating, discussed in Chapter 2, is a logical approach to provide the thermal energy for joining these end members. A microwave susceptor was used to generate the radiant heat necessary to raise the temperature of the end members being joined to a temperature where they could then more efficiently absorb microwaves. The susceptor can be made from a number of materials, including those being examined as potential interlayers. Design parameters that should be considered include the shape of the workpiece being heated, the air gap desired between the workpiece and the susceptor, the method in which the temperature of the workpiece will be measured, and most importantly, the ability of the workpiece to absorb microwaves. This last factor will determine the amount of microwave absorber needed in the susceptor to attain the desired temperature. There are at least two methods of making susceptors. The first consists of fixing a microwave absorbing material to a piece of low density insulation that has been shaped into the desired configuration. This was simple to construct and works well for low temperature applications. The second method involves casting a susceptor using a refractory cement with granules of microwave absorbing material dispersed in it. This method works very well at high temperatures. These susceptors tend to be more massive than the first type and can shield very small specimens from the microwave field.

Microwave Joining Apparatus

The joining apparatus consisted of several components, each with a specific function. To physically support the remaining components, a load frame, capable of sustaining the maximum applied load, was machined from an aluminum alloy. A home model microwave oven* was modified to facilitate the application of pressure and the

*Goldstar MA-1172M 1000 Watt microwave oven

monitoring and control of temperature. An air cylinder* capable of supplying a load of 2.2 kN was mounted on the top of the load frame. A load cell**, mounted in line with the air cylinder, measured the load being applied. The feedback provided by the load cell in the form of a voltage, was used to control the load applied by the air cylinder. An 18 millimeter diameter high-purity alumina rod was used to transfer the load into the microwave cavity. A 20 millimeter feedthrough was machined in the top of the microwave to provide the ram access to the cavity. The diameter of the hole was less than one-sixth the wavelength of the microwaves used in this study. In Chapter 2, the critical hole diameter for significant transmittal of microwaves was found to be one-half the wavelength of the microwave. However, in this setup, there was a dielectric material (alumina push rod, $\epsilon'_r \approx 9$) partially filling the aperture in the wall of the microwave cavity. In this setup, the dielectric material acts as an antenna for microwave propagation and the ability to contain the microwaves was brought into question. To ensure a minimum transmittal of microwave energy via the feedthrough, a 7.5 centimeter long copper tube of the same diameter as the aperture was inserted into the feedthrough. The placement of an electrical conductor tube prevents microwave leakage. Metallic tape was used to cover any other gaps where microwaves might leak. The microwave's turntable was discarded and the turntable motor was relocated to the side of the microwave opposite the wave guide. An aluminum mode stirrer was attached to the motor to improve the uniformity of the field within the microwave. Most of the operations performed during the joining process were controlled by a computer program*** running on a Macintosh IIC. This included storing the values of applied pressure and using this information to adjust the air cylinder. The

*Bellofram model # 900-009 500# air cylinder

**Revere Transducers model # 63HC-D3-500-10p1 500# load cell

***National Instruments Labview Version 2.0

computer was also used to store the temperature readings from two Type-R thermocouples*. The two thermocouples were fed through an eight millimeter hole in the back wall of the microwave cavity. A setpoint controller** was used to regulate the maximum temperature during the process. The temperature controller was spliced into the magnetron power supply so that the temperature could be regulated by turning the magnetron on and off as necessary. Figure 3-5 is a schematic and figure 3-6 is a photograph of the microwave joining setup.

Microwave Susceptors

In preliminary microwave hybrid heating experiments, Dé114 heated alumina in a microwave furnace using a commercially available susceptor***. These microwave furnaces were simply a silicon carbide coating on a low density alumino-silicate refractory. At temperatures near 1500°C, both the silicon carbide coating and the refractory lining experienced significant degradation. This led to a reduction in the furnace's ability to absorb microwaves. Al-Assafi75 produced susceptors using a refractory with a lower dielectric loss factor than the commercially available furnace. This enabled the maintenance of temperatures of 1500°C for one hour without destruction of the susceptor. These susceptors proved sufficient for one experiment, but assembling a susceptor with a uniform coating that maintained its microwave absorbing ability throughout a course of high-temperature experiments was not feasible. It became necessary to seek an alternative approach to microwave hybrid heating to provide a high-temperature, extended-use susceptor. For this research, a mold of the desired susceptor was formed out of concentric

*Ari Inc. model # HIT-99N-4DR9AA-36 Type-R thermocouple

**Omega model # CN9000A Miniature Autotune Temperature Controller

***National Superconductor - Microwave Glass Melter

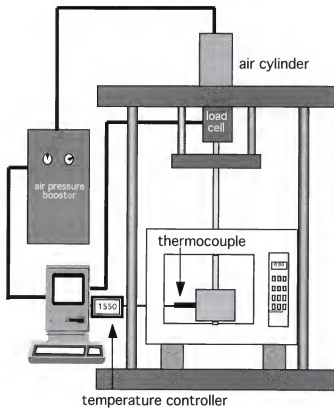


Figure 3-5. Schematic of the microwave joining apparatus.



Figure 3-6. Photograph of the microwave joining apparatus used in all of the microwave joining experiments.

polypropylene cylinders. High alumina content cement* was mixed with silicon carbide granules and enough water to make a slurry. This was cast into the mold and allowed to set. The process for forming the susceptor is outlined in figure 3-7. The polypropylene rings were removed and the cement/SiC cylinder was cured by slowly heating it in a conventional furnace to 1000 °C for one hour. After cooling, the susceptor was ready to use.

The amount of cement and silicon carbide was varied to determine the amount of silicon carbide that would absorb the appropriate amount of microwaves to provide the desired thermal environment for the joining process. This was done systematically by mixing the cement and silicon carbide in different ratios. Silicon carbide granules were added in amounts of 5, 10, 20, and 30 volume percent of the cement. The volumes were determined using the density of alumina to approximate the density of the cement (96% alumina) and the density of silicon carbide. Enough water was added to make the mixture castable. The cylinders were all approximately 300 grams. All of the cylinders were cured as described earlier.

To determine the ability of the cylinders to heat, they were insulated as shown in figure 3-8, placed in a microwave oven and heated using 3200 watts of power. The temperature was measured in both the center of thesuscepting cylinder and outside of the refractory wall using Type-K thermocouples shielded from the microwaves by a inconel sheath. The dielectric properties of the cylinders as a function of temperature were measured at AECL using the cavity perturbation method.

The susceptor used for the joining process was similar to those used in the susceptor evaluation experiments. A 36 volume percent loading of silicon carbide was used in the susceptor. Two 4 millimeter in diameter hollow alumina tubes were fixed in

*Alcoa Al-66 97% Al_2O_3 3% CaO

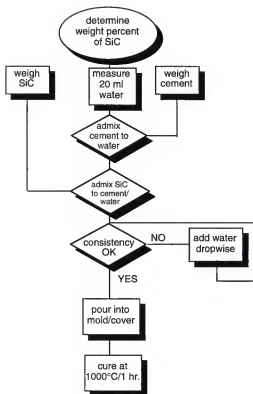


Figure 3-7. Flowchart used to produce susceptors for microwave joining.

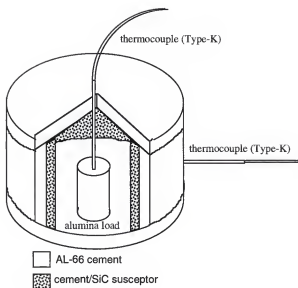


Figure 3-8. Cutaway view of the setup used to evaluate the heating ability of susceptors.

the side wall of the susceptor mold. The tubes allowed the thermocouples access to the specimen being joined. The alumina tubes were maintained as part of the susceptor to act as a barrier between the silicon carbide in the susceptor and the platinum sheath of the thermocouple. To insulate the susceptor, low density fiber board* was cut into pieces that formed a close fitting box around the susceptor. A hole was machined in the top of the fiber board to accommodate the ram used to apply the load. Two smaller holes were machined in the side for the thermocouples and a third hole provided a viewing port for the optical pyrometer. An additional hole was placed in the bottom piece so that another short rod of alumina could support the specimen from the bottom. Figure 3-9 is a schematic and figure 3-10 is a photograph of the susceptor used in the joining experiments.

The first group of experiments involved the joining of assorted end members of AD995 and AD96 alumina using an alumina based gel or AD96 alumina as the interlayer material. The two sols used for these experiments were the sol made with 4 mol% chromia and the sol loaded with 50 mol% nickel aluminate spinel. These gels were chosen because they both heat better than the base gel in a microwave field and they both react predictably under the heating conditions used. Further discussion of the selection of these compositions will be presented in Chapter 5.

The surfaces of the end members to be joined were thoroughly cleaned with acetone. A drop of ethanol was placed on the machined surface of one end member to promote the wetting of the alumina by the sol. The sol was added to the surface dropwise until it was covered completely -- about two milliliters of sol total. The sol was dried in ambient air and formed a solid, glossy layer. The two end members were placed in contact and held together with cellophane tape. The specimen was positioned in a 36 volume percent silicon carbide susceptor and a 50 N load was applied to secure the specimen in

*Rath Performance Fiber Inc, Altra KVS 17/400 high temperature insulating board

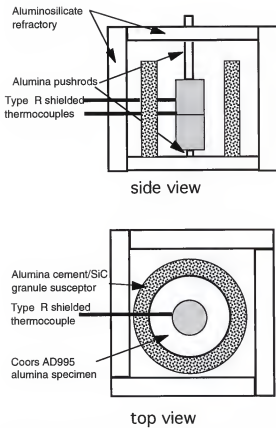


Figure 3-9. Schematic of the specimen/susceptor setup used in the microwave joining experiments.

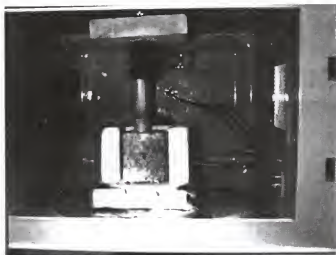


Figure 3-10. Photograph of susceptor set up inside the microwave cavity.

place. The specimen was heated at full power to the setpoint of 1500°C. Approximately 50 minutes were required to attain the setpoint temperature. The specimen temperature was measured with a single Type-R thermocouple described previously, placed in proximity to the joint. From then on, the setpoint controller maintained the temperature at $\pm 7^\circ\text{C}$. A pressure of 2.5 MPa then was applied for a duration of 30 minutes. The power to the microwave was turned off and the pressure reduced. The specimen was allowed to furnace cool to room temperature.

Specimen Preparation

The joined specimens from the microwave joining experiments were characterized using a several step process. After joining, the specimen was visually inspected to determine if it was joined on a macro scale. This inspection was also to look for any indications of problems that may have occurred during the experiment. This included end members that are not parallel due to uneven loading or scorch marks left from extensive arcing between the specimen and the thermocouple. The joined specimens then were mounted upright onto a glass plate so they could be machined into bars for strength testing. The same machine used to prepare the specimens for joining was used for the machining of the flexure bars. A feed rate of five microns per pass was used to cut the joined cylinders into slabs approximately 4.5 millimeters thick. The position of each slab in the starting specimen was noted. The cut slabs then were remounted flat on the glass plate. The surfaces were marked with an indelible marker to ensure that material had been removed from the entire surface of each slab. The exposed surface of the slabs was machined using the diamond wheel described earlier. A downfeed of five microns per pass and a crossfeed of 2.5 millimeters per pass was used to limit the machining stresses experienced by the joined material. When the slabs were machined to a uniform size, the thickness was measured and remounted with the as-cut side exposed. For this side, the downfeed and crossfeed remained the same. However, the amount of material to be removed was

calculated so that the finished slab would be 4.0 ± 0.05 millimeters thick. After the desired thickness was achieved, the diamond slicing wheel was again used to cut the slabs into bars approximately 3.5 millimeters thick. The machined bars were cleaned using acetone in an ultrasonic bath to remove any remaining adhesive used to fix the specimens to the glass plate. Each bar was mounted in a vise to expose the cut surface. In the same manner as the slabs, the bars were machined to a thickness of 3.0 ± 0.05 millimeters. To limit the possibility of the bars fracturing at the edges during testing, a special vise was used to chamfer the edges of each bar. Approximately 75 microns of material was removed from the edge of each bar using the grinding wheel and machining parameters described previously.

During the machining of the test bars, the joined specimens were put under grinding stresses that were typically 5 MPa and above. Several of the joined specimens failed during various stages of the machining process. In some instances, specimens that were considered joined after visual inspection, did not yield any intact bars after the machining process. Figure 3-11 is a schematic of the joining process and the flexure bar preparation.

Mechanical Testing

The bars were tested in a screw-driven test machine*. Four-point bending was used to break the bars. A crosshead speed of 0.5 mm/min was used in all the experiments. Figure 3-12 is a schematic of the test fixture used for all the room temperature flexure tests. After each bar was fractured, the fracture load was noted and the remnants of the test piece were collected for optical inspection of the fracture surface.

Flexure tests were performed at 1000°C on some of the joined specimens. It was necessary to use a different load frame for the high-temperature tests. On this load frame, the load was applied pneumatically so the applied load was controlled as opposed to the

*ATS series 1605 computer controlled universal test machine

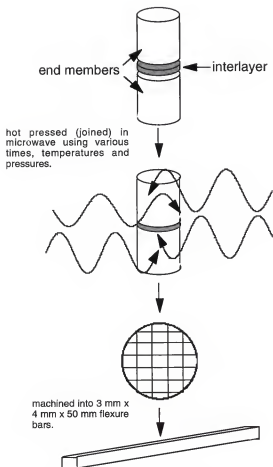


Figure 3-11. Flow diagram of the microwave joining process and specimen preparation.

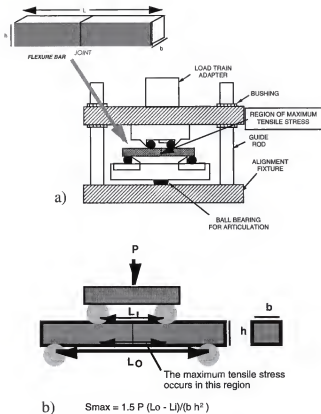


Figure 3-12. Flexure fixture for room temperature testing of bars using four-point bending. a) schematic of flexure rig and b) labels of relevant dimensions.

screw driven machines where the crosshead speed was controlled. Bars from some of the experiments were loaded in an alumina fixture and heated to 1000°C in approximately 30 minutes. When the temperature stabilized, the bars were put under an increasing force of 7 N/s until fracture.

Phase Three

In phase three, the development of an experimental design was used to evaluate the significance of each of the processing parameters on the flexure strength of the joined material. Five of the processing parameters were varied. Two values were selected for each processing parameter and an array of joining experiments were devised. Flexure tests of bars machined from the joined specimens provided the strength data to perform an analysis of variances comparing the two levels of each processing parameter. A separate study was done to evaluate the effect of the original position of the bar within the joined workpiece on the flexure strength. The effect of the bar's position on flexure strength was explored separately for specimens joined using microwave energy and those joined using conventional heating methods. Various analytical methods were employed to characterize the joint region in terms of microstructure, composition and reactivity.

An experimental design was constructed in an effort to determine the relative importance of several of the variables in the joining process. Along with time, temperature and pressure, the interlayer material and the method of heating were investigated. In order to assess the influence of each of the five variables, it was determined that the flexure strength of the joined materials would provide an accurate reflection of the integrity of the joint. Each of these processing parameters were considered at two levels, "high" and "low". For the linear parameters of time, temperature and pressure, the two levels were chosen from the typical range for these parameters for the joining of alumina. The "high" and "low" levels of the non-linear parameters of interlayer material and heating method are

fixed as shown in Table 3-2. Monolithic interlayer materials were used for this portion of the study instead of the gel-derived materials to provide more substantial contact between the end members and the interlayer. To evaluate all of the possible effects of the processing parameters would require an excessive number of experiments. Using the half factorial experimental design laid out by Davies¹¹⁵ permitted the evaluation of the main effect of each of the processing parameters on the flexure strength of the joined specimens. The use of the half factorial design sacrifices the acquisition of information regarding second and higher order effects. An example of a second order effect would be the influence of time on the way pressure effects the flexure strength of the joined material. The number of experiments to fill out this design was calculated from the equation

$$\#ex. = 2^{n-1} \quad (3-2)$$

where # ex. is the number of experiments necessary and n is the number of processing variables (five in this case).

Table 3-2. Levels of Varied Processing Conditions.

	Time (min)	Temperature (°C)	Pressure (MPa)	Heating method	Interlayer material
High (+)	45	1550	3	microwave	AD94
Low (-)	15	1450	1	conventional	NiO

The sixteen experiments needed to provide enough information to sufficiently evaluate each of the processing parameters are identified by this design. Table 3-3 lists the required experiments along with the processing parameters. Note that not every combination of the two levels of each parameter was present. This was the advantage of the half factorial where there were no second order interactions.

Microwave Joining

The eight microwave joining experiments were carried out in the microwave apparatus described previously using the susceptor produced with 36 volume percent

silicon carbide. A nominal load of 50 N was used to secure the specimen in place. Specimens were heated as rapidly as possible to the joining temperature. At that time, the temperature controller turned the microwaves on and off as necessary to maintain the setpoint temperature. Simultaneously, the load was increased to the predetermined value. After the prescribed soak at temperature, the load was reduced to the original level. The initial 20 minutes of cooling was carried out by generating microwaves 40% of the time. The second 20 minutes of cooling was facilitated by the generation of microwaves for 20% of the time. After the forty minutes of controlled cooling, the joined specimen was allowed to cool naturally. This procedure paralleled the cooling profile in the conventional furnace more closely than if the microwaves were just turned off.

Table 3-3. Experimental Design used to Aid in Determining the Effect of Processing Conditions on the Strength of the Joint.

Trial	time (min)	temperature (°C)	pressure (MPa)	heating method	interlayer material
4	15	1450	1	Microwave	NiO
2	45	1450	1	Microwave	Al ₂ O ₃ (94%)
3	15	1550	1	Microwave	Al ₂ O ₃ (94%)
4	15	1550	1	Microwave	NiO
5	15	1450	3	Microwave	Al ₂ O ₃ (94%)
6	15	1450	3	Microwave	NiO
7	15	1550	3	Microwave	NiO
9	45	1550	3	Microwave	Al ₂ O ₃ (94%)
9	15	1450	1	Conventional	Al ₂ O ₃ (94%)
10	45	1450	1	Conventional	NiO
11	15	1550	1	Conventional	NiO
12	45	1550	1	Conventional	Al ₂ O ₃ (94%)
13	15	1450	3	Conventional	NiO
14	45	1450	3	Conventional	Al ₂ O ₃ (94%)
15	15	1550	3	Conventional	Al ₂ O ₃ (94%)
16	45	1550	3	Conventional	NiO

Conventional Joining

The conventional joining experiments described in the experimental matrix were carried out in a furnace designed for high-temperature compression testing. Resistively-heated molybdenum disilicide elements were used to heat the specimens. The specimen to be joined was placed between two 25 millimeter diameter silicon carbide rods extending through both the top and the bottom of the furnace. A load was applied to the upper rod by an air cylinder capable of generating 2000 N of force. A load cell, connected to the lower silicon carbide rod, measured the applied load. As with the microwave joining experiments, a nominal load was used to secure the specimens in place. The temperature of the specimen was measured by a Type-S thermocouple placed within one centimeter of the bottom end member. The furnace was heated at full power up to the joining temperature at which the joining load was applied. When the duration of the joining portion of the experiment had concluded, the load was removed and the furnace was shut off and allowed to cool. A data collection program* was used to apply the load at the setpoint and record the applied load and specimen temperature during the experiment.

Optical Inspection

Specimens that appeared joined after visual inspection were viewed with a stereo microscope to evaluate the quality of the joint. Specimens that were initially considered to be joined but subsequently failed during handling were also inspected using the stereo microscope.

The fracture surfaces of all of the bars tested were inspected using the stereo microscope. Some of the bars were mounted in epoxy so that the joint region was exposed. The bars then were polished to a mirror finish with 0.25 micron diamond paste. The joint region of these specimens were examined in an optical microscope. Several of the

*Keithley 500 data acquisition software; modified by M.K. Ferber, Metals and Ceramics Division, Oak Ridge National Labs

specimens were coated with a carbon film and observed using a scanning electron microscope*.

The roughness of the end member at the joint line was compared to the roughness of the end member prior to joining. This was accomplished by digitizing the joint line from micrographs taken of the profiles of the joint line and of the initial surface. The digitized images were plotted graphically and roughness values were calculated using equation 3-1.

Wavelength dispersive spectroscopy (WDS) was performed using a JEOL Superprobe 733 electron microprobe. X-ray maps generated by this analytical method provide qualitative data with respect to the amount of each of the elements present. The x-ray maps are generated by first calibrating the detector using a standard that contains a known amount of the element to be measured. Then a photograph was taken of the area in question for reference purposes. Finally, the detector performs a sweep across the desired area, measuring the intensity of the x-rays corresponding to the standard. Silica was the main impurity in both AD995 and AD94 alumina. A silicon calibration standard was used to confirm the presence of silica near the joint area of several of the specimens joined using AD94 as the interlayer material.

Statistical Analysis

An analysis of variances (ANOVA) was performed using statistical software** to determine the extent of the effect of the processing conditions on the strength of the bend bars. The program is capable of performing analysis on the half-factorial experimental design devised earlier. There are also provisions that can account for the specimens that were joined on a macro scale, but did not yield any flexure bars after the machining process. The ANOVA compares the mean strengths of the bars at the two levels of each

*Hitachi S-800 Scanning Electron Microscope

**Abacus Concepts - SuperANOVA version 1.11

processing parameter. The program then determines if there is a significant difference between the strengths measured with the two levels at a 5% level of confidence. A separate ANOVA was performed only on the specimens joined using AD94 as the interlayer material. The effect of the position of the bar in the original material (i.e. center; middle; inside; outside) upon the flexure strength was investigated for both the microwave and conventionally joined specimens. A comparison of the results for the two heating methods provides insight into the contribution of volumetric heating towards the uniform heating of large pieces.

Phase Four

Phase four consisted of both the measurement of microwave heating profiles and the generation of these profiles using a heat transfer program. The measured profiles were collected for the workpiece and the outer wall of the susceptor. The temperatures at these two positions were measured using both a shielded thermocouple and an optical pyrometer. In the simulated microwave hybrid heating portion of the experiment, the temperature was tracked at positions corresponding to those monitored in the laboratory experiments. Heating profiles were generated for different interlayer materials and thicknesses. The profiles were compared to the measured temperatures to determine the validity of the model. The development of the model for simulating microwave hybrid heating is discussed in detail in Chapter 4.

CHAPTER 4

NUMERICAL MODELING

While the experimental joining work was being performed, a simultaneous effort was put forth to model the transient temperature profiles of the workpiece being joined and of the microwave susceptor. The purpose of this endeavor was to evaluate the possibility of enhanced heating of the workpiece under microwave hybrid heating conditions.

A conduction heat transfer program* was used to develop a model to simulate the heating profiles measured in a microwave oven. Heating 7.2 is a multifaceted program that allows the user to choose from a variety of coordinate axes in one- two- or three-dimensions to describe the physical model. Many of the material properties necessary for the heat transfer calculations can be input as a constant, or as a function of either time, temperature or position. Heating 7.2 is capable of solving both steady-state and transient heat conduction problems. Transient heating profiles are calculated using one of several finite difference schemes available to the user. An explicit or implicit transient solution technique can be specified for solving the problem. The required input is read from a file resembling a set of Fortran punch cards, relying on keywords to identify the input data. The program output can be readily formatted as an ASCII file which then can be read by many available plotting programs. Heating 7.2 implements the computational method of finite time difference to solve the partial differential equation used to describe heat transfer in materials. Due to the versatility of Heating 7.2, the discussion of the elements of the program will be limited to those pertaining to the intended calculations.

*Heating 7.2 K.W. Childs, Computing Applications Division, Oak Ridge National Labs

Heat Transfer

The first step in calculating heat transfer is to define a grid superimposed on a coordinate axis. Grid intersections are called nodes and each node is surrounded (in 3-d) by eight elements and is in contact with six other nodes. The temperature of each node is calculated from a combination of the properties describing that node, the temperatures of the six nodes in contact and, to a lesser extent, nodes that are nearby but not connected to the node in question. The finite-volume heat balance is based on the partial differential equation representing heat transport in a material, equation 4-1.

$$\rho C_p \frac{\partial T}{\partial t} = K \frac{\partial^2 T}{\partial x^2} + P_v \quad (4-1)$$

where

- C_p = heat capacity, J/kgK
- ρ = density, kg/m³
- K = thermal conductivity, W/mK and
- P_v = absorbed power per unit volume, W/m³.

When this partial differential equation is converted into a finite-volume heat balance equation for node o , it is expressed as

$$C_o \frac{T_o^{n+1} - T_o^n}{\Delta t} = P_o + \sum_{m=1}^6 {}_oK_m (T_m^n - T_o^n) \quad (4-2)$$

where

- T_m^n = temperature of the m th node adjacent to node o at time t_n ,
- ${}_oK_m$ = thermal conductivity between nodes o and m ,
- C_o = heat capacitance of node o , determined from the materials associated with that node,
- P_o = heat generation rate and
- Δt = time step ($t_{n+1} - t_n$).

Node o and the six neighboring nodes are shown in figure 4-1. In a two-dimensional view, this simplifies to the grid structure in figure 4-2. The coordinate system chosen for this research was the r - z - θ system. In the physical model, figure 4-3, there is a symmetry about the z -axis. This symmetry permits the use of a two-dimensional r - z coordinate system instead of the more complicated r - z - θ system. For the two-dimensional model that will be considered here, there will be one C, one P and four K's associated with each node. One K is for each quadrant in contact with the node. For node o , these parameters can be expressed by

$$\begin{aligned} C_o &= \sum_{l=1}^4 c_{pl} \rho_l V_l, \\ P_o &= \sum_{l=1}^4 Q_l V_l, \\ {}_oK_m &= \frac{1}{L_{m\gamma}} \sum_{\gamma=1}^2 k_{m,\gamma} A_{m,\gamma} \end{aligned} \quad (4-3)$$

where

- c_{pl} = specific heat of material in the l th quadrant,
- ρ_l = density of material in the l th quadrant,
- V_l = volume of the l th quadrant of node o ,
- Q_l = heat generation rate per unit volume in the l th quadrant,
- $L_{m\gamma}$ = distance between node o and adjacent node m ,
- $k_{m,\gamma}$ = thermal conductivity of material in the γ th of the two possible heat-flow paths between nodes o and m ,
- $A_{m,\gamma}$ = cross-sectional area of the γ th heat flow path between nodes o and m .

For surface nodes, the general heat balance equation for node i , having M_i neighbors is

$$C_i \frac{T_i^{n+1} - T_i^n}{\Delta t} = P_i^n + \sum_{m=1}^{M_i} {}_iK_{a_m} (T_{a_m}^n - T_i^n) \quad (4-4)$$

where a_m is the m th neighbor of the i th node and T_i^n is the temperature at node i at the n th time level.

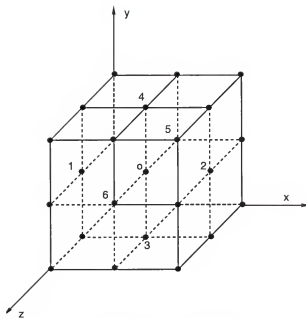


Figure 4-1. Grid structure surrounding node o , the node of interest.

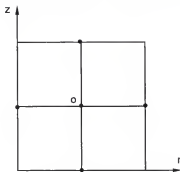


Figure 4-2. Two-dimensional grid structure using the r - z coordinate axes.

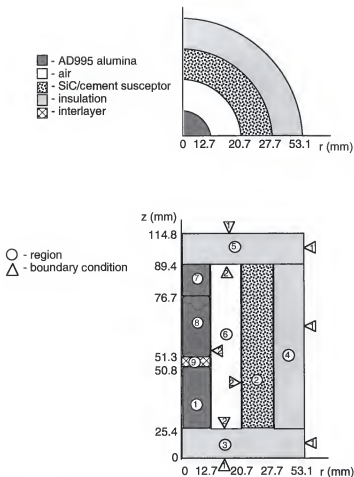


Figure 4-3. Model used for the simulation of microwave hybrid heating. (○ - regions and △ - boundaries refer to materials and conditions used in the model.)

Transient Heat Conduction

The heat transfer model that will be described later in the chapter is a transient heat flow problem and employs an implicit procedure known as the Crank-Nicolson technique to solve it. This is the technique recommended by the authors of Heating 7.2 and is always stable regardless of the size of the time step. The Crank-Nicolson technique generates a system of equations that are solved by a point-successive-overrelaxation iteration. The Heating 7.2 program includes a provision for automatically approximating the optimum acceleration parameter.

Using the Crank-Nicolson method, equation 4-2 becomes

$$C_i^{n+0.5} \frac{T_i^{n+1} - T_i^n}{\Delta t} = P_i^{n+0.5} + 0.5 \left[\sum_{n=1}^M K_{i_n}^{n+0.5} (T_{i_n}^{n+1} - T_i^{n+1}) + \sum_{n=1}^M K_{i_n}^{n+0.5} (T_{i_n}^n - T_i^n) \right] \quad (4-5)$$

For this equation all of the finite differences are taken about the point x_i , $t_{n+1/2}$, halfway between the known and unknown time levels. Figure 4-4 is a graphical representation of the Crank-Nicolson point in a one-dimensional problem. For a problem with N nodes, this equation yields N equations and N unknowns. To solve these equations iteratively, separate the temperatures so that temperatures at t_{n+1} are on the other side of the equation from temperatures at t_n . The equation then becomes

$$H_i = -0.5 \left[\sum_{n=1}^M K_{i_n}^{n+0.5} T_{i_n}^{n+0.5} \right] + \left[\frac{C_i^{n+0.5}}{\Delta t} + 0.5 \sum_{n=1}^M K_{i_n}^{n+0.5} \right] T_i^{n+1} \quad (4-6)$$

where

$$H_i = \frac{C_i^{n+0.5}}{\Delta t} T_i^n + P_i^{n+0.5} + 0.5 \left[\sum_{n=1}^M K_{i_n}^{n+0.5} (T_{i_n}^n - T_i^n) \right] \quad (4-7)$$

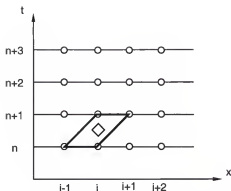


Figure 4-4. Time-temperature coordinates involved in the Crank-Nicolson equation. The trapezoid connects the time-position values used to calculate temperature values at the point indicated, \diamond .

By defining

$$D_i = \frac{C_i^{n+0.5}}{\Delta t} + 0.5 \sum_{m=1}^{M_i} K_{i_m}^{n+0.5} \quad (4-8)$$

and omitting the superscript $(n+1)$ on the temperature T_i , the temperature of node i at the new time level can be written as

$$T_i = \frac{0.5 \left[\sum_{m=1}^{M_i} K_{i_m}^{n+0.5} T_{i_m} \right] + H_i}{D_i} \quad (4-9)$$

However, values of T_{i_m} are unknown, so this equation cannot be solved directly. The existence of an estimate of the temperature distribution at the next time step can be used in equation 4-8 to calculate a new temperature distribution. This process can be iterated until

the approximation of the new temperature distribution converges at the new time level. For the first time step, the initial temperature distribution is input by the user.

When there are temperature dependent thermal properties such as density, thermal conductivity or specific heat, they are recalculated after the new temperature distribution has been determined. The temperature dependent properties of the material between nodes are calculated by evaluating the property of the material at the average temperature of the two adjacent nodes.

Boundary Conditions

Heating 7.2 can accommodate several types of boundary conditions. The boundary conditions are used to manage the discontinuities associated with a surface node. A surface node is a node on the face of a material that is not surrounded by other material nodes. The surface node is connected to a boundary node. A boundary node is a dummy node that represents the temperature of the environment in contact with the surface node. Depending on the type of boundary condition that is specified, the temperature of the environment (dummy node) can be determined in various ways. It can be a constant, a function of time or position, or it can be specified indirectly by defining the heat transfer mechanisms of the surface node. Convection (forced or natural) and radiation are the heat flux mechanisms that must be specified to describe heat flow from a surface node to a boundary node. Temperatures of the surface nodes that have specified boundary conditions are not calculated from equation 4-3. The heat flux is calculated from the specified mechanisms and multiplied by the nodes surface area. The result is added to the heat generation term in equation 4-3. Uncovered regions that are modeled without an assigned boundary condition are modeled as an adiabatic surface.

Surface-to-environment and surface-to-surface are the two types of boundary conditions used in the modeling work in this dissertation. Surface-to-environment boundary conditions are used to describe heat transfer between a surface node and a

boundary node. The surface-to-surface boundary conditions describe heat transfer directly between two corresponding nodes on opposing surfaces. This is an accurate approximation for narrow gaps that do not contain any material.

For both of the boundary conditions discussed, the heat flow term in equation 4-4 is calculated from

$${}_iK_a(T_a^n - T_i^n) = {}_iK_b(T_b^n - T_i^n) \quad (4-10)$$

where

- ${}_iK_b$ = effective conductivity from surface node i to either boundary node b or opposing surface node b .
- T_b^n = temperature of either boundary node b or opposing surface node b at time t_n .

The effective conductivity for the surface node is

$${}_iK_b = hA \quad (4-11)$$

where h is the effective heat transfer coefficient, and A is the surface area of node i associated with the boundary condition. The effective heat transfer coefficient is made up of the heat flux mechanisms discussed earlier and is calculated as

$$h = h_c + h_r \left[(T_i^n)^2 + (T_b^n)^2 \right] [T_i^n + T_b^n] + h_n |T_i^n - T_b^n|^{h_e} \quad (4-12)$$

where

- h_c = forced convection heat transfer coefficient,
- h_r = radiative heat transfer coefficient,
- h_n = coefficient for natural convection,
- h_e = exponent for natural convection.

These parameters must be specified by the user and can be represented as a constant, a function of time or a function of temperature. As with the other temperature dependent properties mentioned previously, the value of each of the parameters for the material between nodes is calculated using the average temperature of the nodes in question.

The Physical Model

Heating 7.2 is an extremely versatile program that can provide a solution for a multitude of heat transfer problems. This versatility requires that a large number of parameters be specified. A complete table of all the possible input parameters is located in Appendix B.

The physical model used is shown in figure 4-3 as a section of the microwave setup being modeled. This figure shows nickel oxide as the interlayer material. In other problems, the nickel oxide is replaced by AD94 alumina. For each problem, the material and thickness of the interlayer will be identified in the problem's input data. As the input parameters are specified, the terms appearing in the model and the reasoning used in the development of the input parameters will be discussed. The data is input in an ASCII file that resembles Fortran punch cards. Each line in the input file is described as a "card". The parameter cards will be identified and discussed in the order that they appear in the input file. Occasionally, a parameter card will refer to another card that has not yet been introduced. At this point, the discontinuity will be noted and the cards will continue to be addressed in the order that they will appear. Some cards will offer choices of input to choose from. The choices that are available are identified in Appendix B. The mks system of weights and measures is used for all of the data input into the sample problem discussed below. Input parameters for each card are identified below in the same manner that they are identified in Appendix B.

Case Title

This parameter card is available to the user to provide a description of the problem. It associates the input data with the programs output.

IOBDES. The case title card may be left blank. The different problems investigated in this study are identified by the type and thickness of the interlayer material used in the physical model.

General Problem Parameters

The general parameters are specified in this card. These are required to initialize the Heating 7.2 program.

MXCPU. This term sets a limit on the computer processor time, in seconds, that the problem may use. If the problem is not solved in the allotted time, the calculations are terminated. For the current study, a large limit of 28,800 seconds (eight hours) was set to ensure the problem would run to completion.

NGEOM. The cylindrical r-z coordinate system was chosen because it most closely resembled the actual problem. This is represented by the input value of 3 from the table in Appendix B.

TIM. The initial problem time was set at zero. There is the potential to restart a previous problem, but this option was never pursued.

IDEGRE. The Celsius temperature scale is used for all of the problems. This is indicated by a 1 on the parameter card, taken from the choices presented in Appendix B.

Region Data

This is actually a set of cards that describe the physical model using the coordinate axes chosen earlier. Each region is represented by two input cards. Card one is used to identify the regions by number, identify the material occupying the region and provide physical dimensions for the region.

NOREG. For the example problem being set up here, the regions are identified in figure 4-3. In this model, there are nine regions that must be specified.

MATS. This term identifies the material occupying the region by a number that points to a card that contains the material's properties.

REGDIM. The dimensional boundaries of each region are input in meters. The region boundaries are labeled in figure 4-3 as millimeters.

The second card in the set specifies the initial temperature of each region, the heat generation of the region and the boundary condition associated with each physical dimension specified in the first card.

ITS. The initial temperature can be varied from region to region. This card designates the card that will describe the initial temperature for a given region.

NGENS. This term inputs the identification number of the heat generation card associated with each region. The values for the different heat generations are specified later in the text.

NREGBC. The boundary conditions, specified later, are associated with each of the regions physical boundaries.

The values for all of the input data that describe the nine regions are summarized in Table 4-1.

Materials

The materials card specifies the various properties of the material that are necessary for the calculations. The four materials represented in the model are AD995 alumina, a silicon carbide/AL-66 alumina cement, Rath fiber insulation and nickel oxide.

MAT. This is the card identification number that is pointed to in the region material number card.

MATNAM. This space contains an allotment of eight characters for the name of the material.

DENSTY. This entry is for the density of the material in kilograms per cubic meter. The density values used for the AD995 alumina and the insulation was the density reported by the manufacturer. The density of the susceptor was measured at AECL during the evaluation of the susceptors dielectric properties. A sintered density of approximately 80% of theoretical was reported by the manufacturer of the nickel oxide.

SPHEAT. This contains the specific heat if it is a constant. The manufacturer reports the specific heat of the insulation material to be 920 J/Kg.°C.

Table 4-1. Summary of the Parameter Cards Used to Describe the Nine Model Regions.

card 1	region	material	smaller r	larger r	smaller z	larger z
card 2	initial temperature	heat generation	smaller r boundary	larger r boundary	smaller z boundary	larger z boundary
1	1	0	0	0.0127	0.0254	0.0508
2	1	1	0	1	0	0
1	2	1	0.0207	0.0277	0.0254	0.0894
2	1	2	1	0	0	0
1	3	3	0	0.0531	0	0.0254
2	1	3	1	1	0	0
1	4	1	0.0277	0.0531	0.0254	0.0894
2	1	1	1	1	0	0
1	5	3	0	0.0531	0.0894	0.1148
2	1	3	0	1	0	1
1	6	1	0.0127	0.0207	0.0254	0.0894
2	1	1	2	2	2	2
1	7	4	0	0.0127	0.0767	0.0894
2	1	0	0	1	0	0
1	8	1	0	0.0127	0.0513	0.0767
2	1	1	0	1	0	0
1	9	5	0	0.0127	0.0508	0.0513
2	1	4	0	1	0	0

NCONTP. This points to a function card that represents the thermal conductivity of the material as a function of temperature.

NSPHTP. This points to a function card that represents the specific heat of the material as a function of temperature.

The materials cards for the four materials in the model are shown in Table 4-2.

Table 4-2. Input Parameters for the Four Materials Represented in the Model.

material number	material name	density (kg/m ³)	temperature dependent thermal conductivity function*	temperature dependent specific heat function
1	AD995	3810	-1	1
2	susceptor	2060	-2	1
3	insulation	400	2	1
4	nickel oxide	5336	-3	3

*A positive integer references an analytical function and a negative integer a tabular function.

Initial Temperature

This is the card that was specified earlier in the region definition cards to describe the initial temperature of a particular region.

INT. This is the identification number of the initial temperature card for the problem.

TEMPIN. An initial temperature of 45°C was used for all of the experiments. It was not necessary to start at a lower temperature because the thermocouples used in the actual experiments are not accurate at low temperatures.

Heat Generation

This card was specified in the region definitions card. It represents a unique heat generation term for each material.

NGN. This is the heat generation identification number referred to previously.

NGNFCN. This term points to a function card that describes a temperature dependent heat generation function. The origin of these functions will be addressed in the section detailing the function cards.

Table 4-3 represents the heat generation cards for the four materials. A fifth material, air, has material properties accessible from the materials library contained in Heating 7.2.

Table 4-3. Heat Generation Cards for the Four Materials in the Model.

material	heat generation number	temperature dependent function
AD995	1	4
susceptor	2	5
insulation	3	6
nickel oxide	4	7

Boundary Conditions

A boundary condition is defined for each unique boundary condition identification number. Each boundary condition consists of several cards that describe the characteristics of that boundary as well as the coefficients, exponents and functions that help define the boundary. The first card defines the type of the boundary condition present. The second card specifies the coefficients and exponents associated with the heat transfer characteristics of the boundary condition. The third card points to equation cards that describe the dependent behavior of the heat transfer characteristics of the boundary condition.

NBDTB. This term identifies the boundary condition with a unique number that corresponds with a regions dimension. Card 1.

NBYTYP. Designates the type of the boundary condition that is associated with the boundary condition number. The type of boundary condition is chosen from the table in Appendix B. Card 1.

BYTEMP. Specifies the boundary temperature in degrees Celsius. This is not applicable to surface-to-surface type boundaries. Card 1.

BCDEF(2). This specifies the radiation coefficient term, h_r , for the determination of the effective heat transfer coefficient. Since alumina is the predominant material in all of the boundary conditions, the radiation coefficient term for alumina will be used in the boundary condition description. To determine this, the material at the boundary condition is assumed to be a gray body. This leads to the equation

$$E = h_r T^4 \quad (4-13)$$

where

E	=	energy emitted from a radiating gray body,
h_r	=	radiation coefficient term, fraction emitted $\times \sigma$,
σ	=	Stephan-Boltzman constant, $5.6697 \times 10^{-8} \text{ W/m}^2\text{K}^4$ and
T	=	temperature (K).

The fraction emitted refers to the percent of the energy that the gray body emits relative to a blackbody emitter. The emissivity for alumina is about 98% at room temperature, decreases to 80% at 400°C and drops off steadily from there¹¹⁶. The radiation coefficient term is then calculated to be

$$h_r = 0.98(\sigma) = 5.5563 \times 10^{-8} \text{ W/m}^2\text{K}^4 \quad (4-14)$$

and was placed in card 2. This is the emissivity at room temperature. To calculate the emissivity at higher temperatures, h_r is multiplied by an analytical function determined later in this chapter.

BCDEF(3). This specifies the natural convection multiplier term, h_n . For natural convection, the coefficient is determined by the geometry of the boundary. For a cylindrical configuration the empirical correlation is

$$\frac{h_n L}{k} = C (Gr_L Pr)^a \quad (4-15)$$

where

L	=	characteristic length of the configuration, m
k	=	thermal conductivity of air, W/m·K
C	=	correlation for geometry,
Gr_L	=	Grashof number,

Pr = Prandtl number, typically 0.7 for air,
 a = natural convection exponent term.

The characteristic length, L, is defined in a table for various geometries. For this model it is the height of the boundary, 0.064 m. The thermal conductivity of air changes over the temperature range in question. However, it is not a significant change so the thermal conductivity of air was taken to be that at 650°C, 0.0626 W/m·K. The correlation, C, is taken from the same table as the characteristic length and is determined to be 0.59 for this geometry. The natural convection exponent term, a, was determined from the same table to be 0.25. The Grashof number for an enclosed space is calculated from the equation

$$Gr = \frac{g\beta(T_s - T_\infty)b^3}{\nu^2} \quad (4-16)$$

where

g = acceleration due to gravity, 9.81 m/s²,
 β = coefficient of volume expansion = 1/T,
 T_s = surface temperature, °C,
 T_∞ = temperature of the environment, °C,
 b = distance between surfaces, m,
 ν = velocity (flux) of air, m²/s.

To maintain consistency in the calculations, the Grashof number was calculated at 650°C and determined to be 15,032. This was used to calculate the natural convection multiplier term, 5.85 W/m²·K. Card 2.

BCDEF(3). This is the exponent term, a, that was determined in the previous calculations and is now identified as h_c. Card 2.

NBCTEM. This card refers to the temperature dependent function for radiation that is multiplied by the radiation coefficient specified earlier. The function will be determined later using the emissivity of alumina as a function of temperature.

Grids

A set of two cards are used to define the grid for each axis. The first card is the gross grid lines for the r and z axes. These are determined from the dimensional

boundaries of the regions described previously. The second card is the fine grid lines to be included between each set of gross grid lines. Fine grid lines are used to subdivide the material regions for more accurate calculations. There will be one less entry on this card than the first. Table 4-4 is both the gross and fine grid lines for each axis.

Table 4-4. Table of the Gross and Fine Grid Lines for Both the r and z Axes.

card 1	smallest gross grid	next larger gross grid	next larger gross grid	next larger gross grid	next larger gross grid	next larger gross grid	next larger gross grid
card 2	divisions between 1 st and 2 nd gross grid lines	divisions between 2 nd and 3 rd gross grid lines	divisions between 3 rd and 4 th gross grid lines	divisions between 4 th and 5 th gross grid lines	divisions between 5 th and 6 th gross grid lines	divisions between 6 th and 7 th gross grid lines	divisions between 7 th and 8 th gross grid lines
r-axis	0.0	0.0127	0.0207	0.0277	0.0531	-	-
r-axis	4	3	3	8	-	-	-
z-axis	0.0	0.0254	0.0508	0.0513	0.0767	0.0894	0.1148
z-axis	8	8	1	8	4	8	-

Analytical Functions

The analytical functions developed in this section describe either the time or temperature dependent properties that were addressed previously. When fitting data with an analytical function, care must be taken so that there is no aberrant behavior in the function outside of the data that has been fitted. An example of this would be fitting a set of decreasing thermal conductivities over a relatively short temperature range. This provides a monotonic curve with a negative slope. Over most of the temperature regime this does not represent a problem. However, at very high temperatures the thermal conductivity becomes negative, causing the heat to flow from the cooler to the hotter nodes within the material. To avoid these situations, some of the data has been input as tabular functions which will be discussed later. For the input, the first card identifies the analytical function. The second card is a series of pairs of values. The first number in each pair refers to the coefficient index, A_i , for the general analytical equation

$$F(V)=A_1 + A_2V + A_3V^2 + A_4\cos(A_5V) + A_6\exp(A_7V) + A_8\sin(A_9V) + A_{10}\ln(A_{11}V) \quad (4-17)$$

and the second number is the user specified value of the coefficient.

Specific heat. The first analytical function represents the temperature dependent specific heat of the predominantly alumina materials, AD995 and the susceptor. Furukawa et al.¹¹⁷ measured the specific heat of alumina as a function of temperature. Figure 4-5 is a fitted plot of their reported data. The coefficients from the logarithmic fit are used in the analytical cards to describe the temperature dependent behavior of the specific heat of the AD995 alumina and the susceptor. Miyayama et al.¹¹⁸ reported the specific heat of nickel oxide at several temperatures. Figure 4-6 is a plot of analytical function fitting their data.

Thermal conductivity. Unlike the less porous materials, the slope of the thermal conductivity for the insulation board is positive. Values for the thermal conductivity of the fiber board were taken from the manufacturer's information sheet* and plotted as a function of temperature in figure 4-7 along with an analytical fit of the data.

Power generation. The determination of the power generation terms for each of the materials in a microwave field was a several step process. The first piece of information needed was the magnitude of the electric field in the microwave. Typically, the electric field in a microwave oven varies with position throughout the microwave cavity. Microwave oven manufacturers attempt to obtain a uniform electric field by optimizing the dimensions of the microwave cavity. In addition, a metal fan to stir the microwaves or a turntable to move the load through the field is added to increase the uniformity of the electric field. For the purpose of these calculations, the electric field is assumed to be uniform throughout the microwave cavity.

*Rath Performance Fibers Inc. gm:\ww\data\kvs\17-40.pri

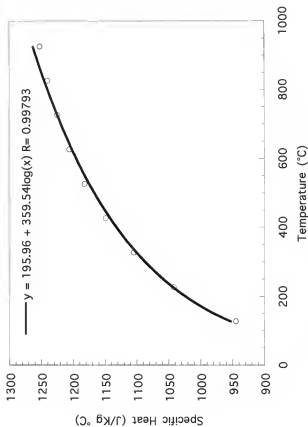


Figure 4-5. Logarithmic fit to data for the specific heat of alumina.

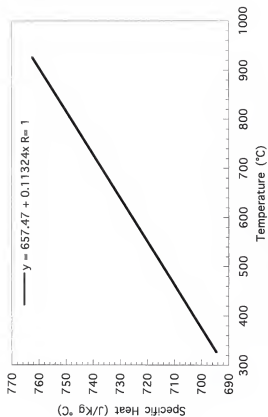


Figure 4-6. Linear fit for the specific heat of nickel oxide.

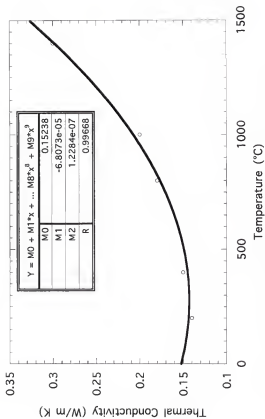


Figure 4-7. Polynomial fit to thermal conductivity of insulating fiber board.

Calorimetry was used to calculate the intensity of the electric field. This consisted of placing an insulated beaker of water in the microwave oven. A thermocouple was immersed in the water to a point approximately at the center of the beaker. The water then was heated using full power and the temperature was measured. Figure 4-8 is a plot of the temperature of the water as a function of time. The rate of rise of the water temperature is the slope of the graph. The electric field in the water can be calculated from the rate of rise in water temperature using the equation

$$E_{H_2O} = \sqrt{\frac{\rho C_p \left(\frac{T - T_0}{t} \right)}{0.556 \times 10^{-10} f \epsilon_{eff}^*}} \cdot \frac{V}{m} \quad (4-18)$$

where

- E_{H_2O} = electric field,
 ρ = density of water (Kg/m^3),
 C_p = specific heat of water ($\text{J/Kg}\cdot\text{K}$),
 $\frac{T - T_0}{t}$ = temperature rate of rise ($^{\circ}\text{C/s}$),
 f = frequency of microwaves (sec^{-1}),
 ϵ_{eff}^* = effective dielectric loss.

At a temperature of 50°C the electric field in the water is calculated to be 2.34 kV/m . The electric field in the microwave cavity (external field) can be calculated using the dielectric constant of water at 50°C , $\epsilon_{H_2O} = 80$, from the equation

$$E_{ext} = E_{H_2O} \frac{\epsilon_{H_2O}}{\epsilon_{ext}} \quad (4-19)$$

where

- E_{ext} = external electric field (V/m),
 ϵ_{ext} = external dielectric constant (air, $\epsilon = 1$)⁴².

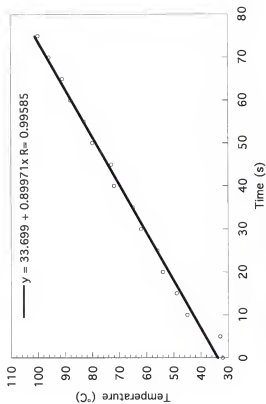


Figure 4-8. Temperature of water as a function of time.

The external electric field is calculated to be 187.2 kV/m. Since the field in the microwave is assumed to be uniform this will be the value used to calculate the absorbed power in each of the materials.

The next bits of information needed were the dielectric properties of each of the materials as a function of temperature. The dielectric constant and dielectric loss were measured on samples of the AD995, the susceptor and the nickel oxide by Ron Hutcheon at the AECL using the cavity perturbation method referred to previously. From these data as well as from the calculated electric field, the power in the alumina, the nickel oxide and the susceptor was calculated at several temperatures using the equation

$$P_a = 2\pi f \epsilon_0 \epsilon_d \tan\delta |E_{int}|^2 \quad (4-20)$$

where

P_a	=	power absorbed by the material, W/m ³ ,
f	=	frequency of microwaves, s ⁻¹ ,
ϵ_0	=	permittivity of free space,
ϵ_d	=	dielectric constant of material,
$\tan\delta$	=	loss tangent of material,
E_{int}	=	internal electric field of material, W/m ² .

The value for E_{int} in all three materials was calculated as a function of temperature using equation 4-19 and the dielectric data measured at AECL. These values then were plotted and fitted to a curve. Figure 4-9 is a power fit to the power absorbed versus temperature data for AD995 alumina. The coefficients were used to represent the temperature dependent power generation term as an analytical function. There was no dielectric data available for the insulation board. The insulation had a porosity of 90% (10% dense). Therefore, since the insulation board was predominantly alumina, the power generation was assumed to be 10% of that of the AD995 alumina. For the nickel oxide, a similar set of calculations were performed using equation 4-20. Figure 4-10 is a second order

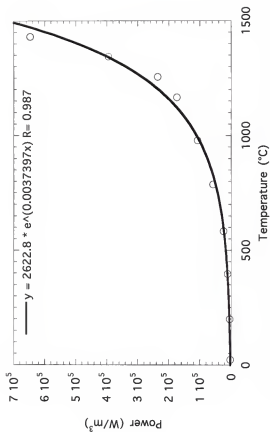


Figure 4-9. Power absorbed (calculated) as a function of temperature for AD995 alumina.

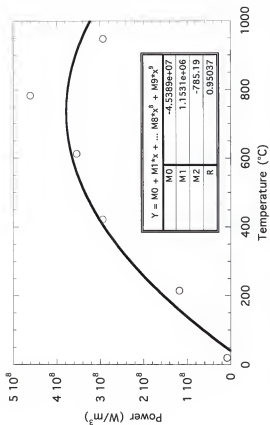


Figure 4-10. Power absorbed (calculated) as a function of temperature for nickel oxide.

polynomial fit to the power absorbed versus temperature data for nickel oxide. The susceptor is actually a composite material made from the relatively microwave transparent cement and the strongly absorbing silicon carbide. There are two possible approaches to determine the dielectric properties of the susceptor. The first is to treat it as a composite and use a weighted proportion of the dielectric properties for each material. The second approach is to use the dielectric data measured from a specimen cast with the same composition as the susceptor. The second approach was chosen for use in the model using the data obtained for the susceptor in the experiments described in Chapter 3. Figure 4-11 is the power curve fit to the data for the susceptor similar to the one used in the laboratory experiments. The data in the curve is valid over only a limited temperature range. This is due to the increasing inaccuracy of the cavity perturbation method for dielectric measurements on strong microwave absorbers. As the dielectric losses increase, the penetration depth decreases and the material begins to act as a microwave reflector. This affects the ability to measure the dielectric properties accurately by increasing the error associated with the measurement.

Boundary condition. As mentioned previously, the emissivity of alumina decreases with increasing temperature. The coefficient was calculated in equation 4-14 to be approximately $5.56 \times 10^{-8} \text{ W/m}^2\text{K}^4$. The function that accompanies the coefficient to describe the decreasing emissivity with temperature is shown in figure 4-12.

Tabular Functions

Tabular functions were used to represent the thermal conductivities of the three materials that exhibited a decrease in thermal conductivity as a function of temperature. This was done to eliminate the possibility of the analytical equation resulting in erroneous values. At temperatures below the temperature listed for the first tabular entry, Heating 7.2 uses the lowest value. While within the temperature range of the table, the functions values are interpolated. At temperatures above the highest tabular value, the last value is used.

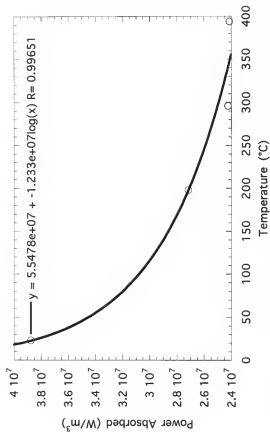


Figure 4-11. Power absorbed (calculated) as a function of temperature for the 30 vol.% SiC susceptor.

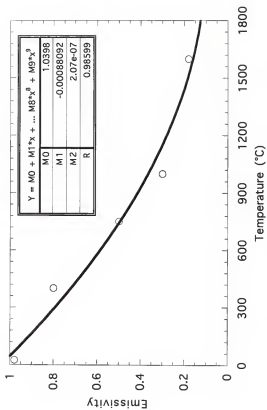


Figure 4-12. Curve fit for the emissivity of alumina as a function of temperature.

The tabular function option uses two cards to describe each function. The first card is the function number that was referred to earlier in the input. The second card is a series of paired table values. The first number is the independent value and the second number is the corresponding dependent value.

Thermal conductivity. The thermal conductivity at several temperatures for the AD995 alumina was obtained from the same source as the emissivity for alumina¹¹⁶. Table 4-5 is the thermal conductivity data available for the AD995 alumina.

Table 4-5. Thermal Conductivity of Coors AD995 Alumina at Different Temperatures.

Temperature (°C)	Thermal Conductivity (W/m·°C)
25	33.47
700	7.53

For nickel oxide, the thermal conductivity values were obtained from the same source as the specific heat¹¹⁸. Since the nickel oxide used in this study had a density of 80% the theoretical value, the reported values were adjusted for porosity using the rule of mixtures

$$P = P_1 V_1 + P_2 V_2 + P_1 V_1 + V_p \quad (4-21)$$

where

- P = value of the material property of composite,
- P₁ = value of the material property of the first component,
- V₁ = volume fraction of first component,
- V_p = volume fraction of porosity.

These values for nickel oxide are listed in Table 4-6.

Table 4-6. Thermal Conductivity of the Nickel Oxide Used in the Model at Different Temperatures.

Temperature (°C)	Thermal Conductivity (W/m·°C)
200	17.05
800	5.0

The susceptor is a composite of alumina cement, silicon carbide and porosity. The thermal conductivity of the susceptor was calculated using the rule of mixtures for the three

materials. The volume percent of porosity can be calculated using the measured density, the density of alumina and silicon carbide and the proportions of cement and silicon carbide used in the susceptor. The thermal conductivity of the porosity was assumed to be zero. The thermal conductivity of the cement was taken from the information sheet provided by the manufacturer*. Select values of the thermal conductivity of silicon carbide were reported in a compilation of properties of materials¹¹⁹. The volume weighted values of the cement and silicon carbide then were added to obtain the thermal conductivity of the composite. The calculated values for the thermal conductivity of the susceptor used in this model are listed in Table 4-7.

Table 4-7. Calculated Values for the Thermal Conductivity of a 30 wt.% SiC/Cement Susceptor.

Temperature (°C)	Thermal Conductivity (W/m·°C)
200	2.07
700	1.35

Printout Times

This card specifies the times at which a solution summary of the transient solution is written to the main output file. The times are consistent with the models units so for this study the times were in seconds.

PRTIME. This is the value of the printout times listed sequentially. An interval of 300 seconds was chosen for the printout times for all of the calculations in this study. The printout times are then at 300 s, 600 s, 900 s, 1200 s, 1500 s, 1800 s, 2100 s, 2400 s, 2700 s, and 3000 s.

*The Carborundum Company - Alfrax No. 66 Aluminum Oxide Castable Form A-2043.

Nodes Monitored

Heating 7.2 has a provision for the monitoring of specified nodes during the calculations. The program has the ability to write the temperatures at these nodes to a separate file during calculations.

NTS. This specifies the number of time steps between the writing of the temperature of the nodes to an output file.

NDS. This entry contains the identity of the nodes by number that the user wishes to monitor.

Transient Data

This set of three cards is used to specify the parameters that are desired to govern the transient calculation technique.

NTYPE. The transient solution technique to be used is specified from Appendix B. For all of the calculations, an implicit solution is used. Card 1.

ETIME. This input specifies the final time for the calculations, indicating when the program should terminate. Card 1.

THETA. The input here determines the differencing technique used. This value corresponds to several of the coefficients and exponents in equations 4-5 through 4-8. To specify the Crank-Nicolson technique, this value was set at 0.5. Card 2.

DELTAT. This value is the initial time step for the implicit solution. A value of 0.5 seconds was chosen because it is near the value determined by Heating 7.2 and provides a more organized output than the time step calculated by the program.

The last card is the data termination card that sends a flag to the program that the input is complete. This card consists only of a percentage symbol, %.

Figure 4-13 is the resulting input file for the situation that has been described here. The input directs Heating 7.2 to calculate the heating profile for the physical model in figure 4-3 heated in a microwave at full power for fifty minutes. The temperature at select nodes

```

susceptor 0.5mm nio
26800 3 0 1
regions
1 1 0.0 0.0127 0 0 0.0254 0.0508
1 1 0 1
2 2 0.0207 0.0277 0 0 0.0254 0.0694
1 2 1
3 3 0.0 0.0531 0 0 0.0 0.0254
1 3 0 1 0 0 1
4 3 0.0277 0.0531 0 0 0.0254 0.0694
1 3 0 1
5 3 0.0 0.0531 0 0 0.0894 0.1148
1 3 0 1 0 0 0 1
8 5 0.0127 0.0207 0 0 0.0254 0.0694
1 0 2 2 2
7 1 0.0 0.0127 0 0 0.0767 0.0894
1 1 0 1
8 1 0.0 0.0127 0 0 0.0513 0.0767
1 1 0 1
9 4 0 0 0.0127 0 0 0.0508 0.0513
1 4 0 1
Materials
1 AD950 0 3810 0 -1 0 1
2 aia 0 2060 0 -2 0 1
3 inail 0 400 0 2 0 1
4 nio 0 5338 0 -3 0 3
5 *550f 1
Initial temperatures
1 45.0
heat generations
1 0 0 4
2 0 0 5
3 0 0 6
4 0 0 7
boundary conditions
1 1 45.0
0 4.558e-8 5.85 0.25 0 2
0 8
2 3
0 4.558e-8 5.85 0.25 0 2
0 8
rgrid
0 0 0.0127 0.0207 0.0277 0.0531
4 3 3 6
zgrid
0 0 0.0254 0.0508 0.0513 0.0767 0.0694 0.1148
8 8 1 8 4 8
analytical functions
1
1 195.96 10 359.54 11 1
2
10.15238 2 -8.8073e-5 3 1 2284e-7
3
1 657.47 2 0 11324
4
6 24917 7 3.7397e-3
5
1 5.6676e7 10 -1.233e7 11 1
6
6 2491.7 7 3.7397e-3
7
1 -4.3369e7 2 1 1531e6 3 -785 19
tabular functions
1
25 33 47 700 7 58
2
25 2.07 700 1 35
3
200 17.05 800 5 0
printout
300 600 900 1200 1500 1800 2100 2400 2700 3000
nodes monitored
600 328 333 334 423
standart
2 5001
0.5
0.5
%

```

Figure 4-13. Sample input to calculate a heating profile of the model in figure 4-4.

corresponding to the several points of interest will be output for every five minutes of simulated heating. Figure 4-14 is a map of the node numbers with the material regions outlined. Table 4-8 lists the nodes of interest and where they are on figure 4-14. These nodes were chosen so that the calculated temperature could be compared to the temperatures that were measured for the workpiece, susceptor and interlayer in the preceding chapter.

Table 4-8. Nodes of Interest and Their Placement in the Model.

node number	position
326	interior of interlayer
328	exterior of interlayer, facing susceptor
334	interior of susceptor
335	exterior of susceptor, bounded by insulation
421	interior of end member
423	exterior of end member, facing susceptor

The input file in figure 4-13 was run using Heating 7.2. The temperature at each of the nodes was written to a separate output file. The temperatures appear as a block of numbers for each of the output times requested on the printout card, PRTIME. Figure 4-15 is a sequence of temperature profiles generated from the example using 10 minute increments of time. Similar input files, altered to reflect interlayers of varying materials and size, were also processed. Comparisons of the temperatures of the nodes that were monitored were made with the experiments performed in Chapter 3. These will be discussed in Chapter 5.

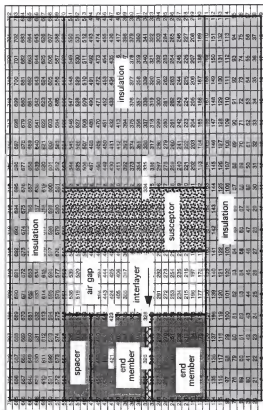


Figure 4-14. Map of node numbers for the input file in figure 4-13. Geometry corresponds to the model in figure 4-3. The nodes that represent thermocouple locations are 328 (interlayer) and 423 (bulk). The pyrometer is represented by node 328.

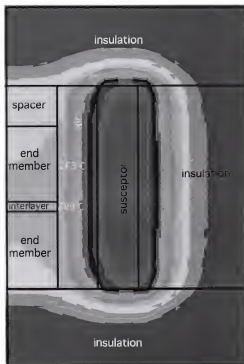


Figure 4-15. Temperature profiles for simulated microwave hybrid heating generated using the input in figure 4-13. a) 10 minutes; b) 20 minutes; c) 30 minutes; d) 40 minutes; e) 50 minutes. Temperatures indicated represent thermocouple positions.

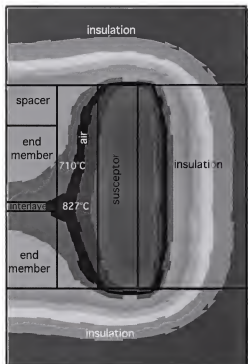


Figure 4-15 -- continued

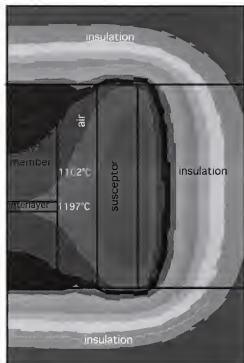


Figure 4-15 -- continued

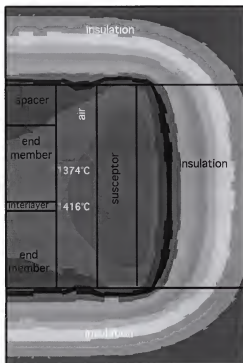


Figure 4-15 -- continued

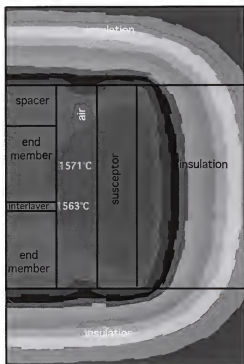


Figure 4-15 -- continued

CHAPTER 5

RESULTS

Machined Surfaces

The machined surfaces of all the sample alumina pieces used were similar. The finish of a typical machined surface finish is shown in figure 5-1. The surface appears flat and featureless at the magnification used. The same machined surface was characterized with a laser profilometer using the conditions outlined in Chapter 3. A three-dimensional plot corresponding to the surface in figure 5-1 is displayed in figure 5-2. Using equation 3-1, the roughness (arithmetic mean) of a single surface scan was calculated to be 2.47 microns. Figure 5-3 is a photograph of the surface of a machined nickel oxide interlayer. The nickel oxide had a porosity of 20% and was much more delicate than the alumina. During the machining process, special care was taken to avoid damaging the nickel oxide disks. After machining, the cleaning of the surface removed some of the surface texture imparted by the grinding wheel. Figure 5-4 is a laser profilometer profile generated for the machined nickel oxide surface. The roughness (arithmetic mean) for the nickel oxide surface was calculated to be 1.40 microns.

Sol-Gel Interlayers

Stand Alone Heating

All of the interlayer materials investigated that contained a sol-gel-derived powder were heated at full power (750 W*) in the microwave using the setup in figure 3-4. Figure 5-5 is a plot of the temperature of the pellets made from the potential interlayer materials as

*Microwave output reported by manufacturer.

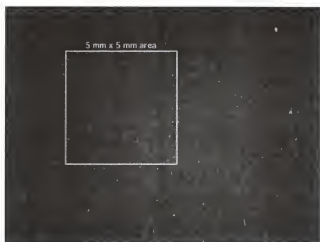


Figure 5-1. Area of the surface of alumina end member used for roughness analysis.

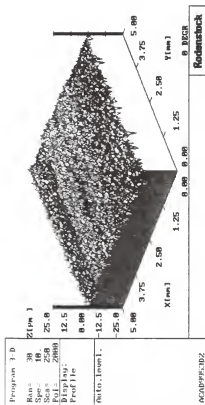


Figure 5-2. Profile of 5 mm x 5 mm area of alumina from figure 5-1 analyzed using a laser profilometer. Light regions correspond to the area above mean peak height and darker regions correspond to area below mean peak height.

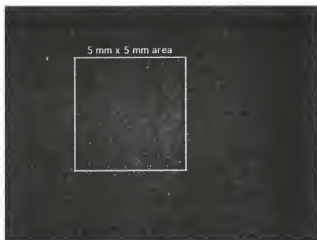


Figure 5-3. Area of the surface of nickel oxide interlayer used for roughness analysis.

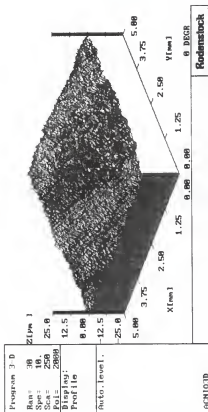


Figure 5-4. Profile of 5 mm x 5 mm area of nickel oxide from figure 5-3 analyzed using a laser profilometer. Light regions correspond to the area above mean peak height and darker regions correspond to area below mean peak height.

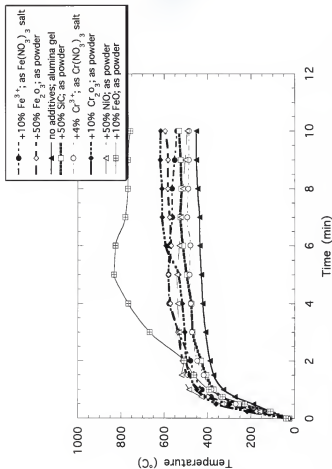


Figure 5-5. Temperature of the potential interlayer materials heated using stand alone microwave heating.

a function of time. All of the materials rapidly heated to 400°C in the microwave oven. At this point, the rate of the rise in temperature decreased in all but one of the materials. The pellet containing 10 mol% iron (II) oxide continued to heat to a maximum temperature of 841°C. After the maximum was reached, the temperature decreased to approximately 750°C where the experiment ended. The pellets made with either an iron or chromium salt substituted for the aluminum salt, heated at a slightly faster rate than the base gel. The pellets containing 4 mol% chromia and 10 mol% iron (III) oxide reached temperatures of 40°C and 100°C above that of the base gel, respectively. The pellet containing 50 mol% SiC reached a maximum temperature of 532°C, 75°C above that of the base gel.

Differential Scanning Calorimetry

The base gel and four of the more promising materials (nickel oxide, silicon carbide, iron (II) oxide and 4 mol% chromia) were chosen for continued study. Figure 5-6 shows the DSC traces for the five materials. The temperature regimes shaded on the figure are labeled with the reactions most likely responsible for peak formation. All of the gel-derived powders exhibited an endotherm between 100°C and 200°C. The next reaction observed appeared at a temperature slightly above 200°C. The endotherm was observed in all of the materials and was most pronounced in the gel made with 4 mol% chromia. An endotherm was detected in all of the materials beginning at 400°C and ending near 450°C. The specimen containing 50 mol% silicon carbide featured an exothermic peak between 525- 550°C. This was the only specimen to exhibit this behavior. All of the powders displayed an exotherm between 1150°C and 1210°C. The exothermic peaks for specimens with 50 mol% nickel oxide and silicon carbide closely resembled that of the base gel. However, the peaks for both compositions were less intense than that of the base gel. For the specimen made with 4 mol% chromia, the exothermic peak in this region was similar in size to the base gel endotherm. However, it appeared at a temperature 50°C above that of the base gel. The specimen made with 50 mol% iron (II) oxide contained two exotherms in

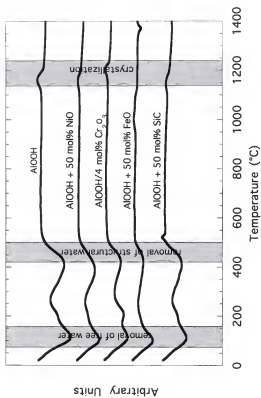


Figure 5-6. Differential Scanning Calorimetry (DSC) of the base gel, alone and with additives.

this temperature range. The two peaks were diffuse and overlapped each other but were still distinguishable as two separate peaks. An endothermic peak unique to the 50 mol% iron (II) oxide specimen appeared near 1350°C.

X-ray Diffraction Analysis

Powder x-ray diffraction analysis was performed on the specimens retrieved from the DSC. An additional sample of the 50 mol% iron (II) oxide was run in the DSC to a temperature of 1200°C to provide information about the specimen prior to the last endotherm observed in the DSC trace. The x-ray analysis was carried out in the manner described in Chapter 3. Figure 5-7 shows the x-ray scans for the ceramic powders made from gel precursors heated in the DSC.

The powder made solely of the base gel had x-ray peaks that correspond well to those of high-purity alumina *. All of the peaks present had a corresponding peak on the ICDD card. The powder loaded with nickel oxide displayed peaks that could be attributed to alumina, nickel oxide and a nickel aluminate spinel. The production of the gel with 4 mol% chromia rendered a specimen with x-ray peaks that resembled the alumina ICDD card. All of the peaks in this specimen were shifted slightly to lower 2θ values. The specimen containing 50 mol% silicon carbide produced x-ray peaks corresponding to silicon carbide and alumina. When the specimen loaded with 50 mol% iron (II) oxide was heated to 1400°C, alumina and iron (III) oxide were the predominant phases present. When a similar specimen was heated to only 1200°C, there was evidence of a third phase, in addition to alumina and iron (III) oxide, with peaks that correspond to the iron (II) aluminate spinel, $\text{FeO} \cdot \text{Al}_2\text{O}_3$. All of the specimens were heated in flowing air and a change in the oxidation state of some of the iron (II) oxide was expected.

*International Centre for Diffraction Data; card 10-0173 - aluminum oxide/corundum

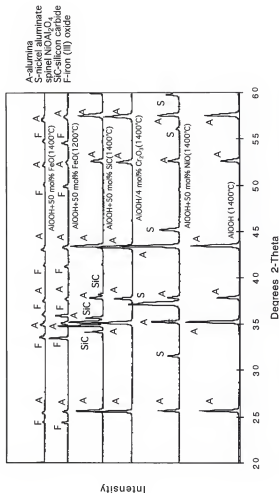


Figure 5-7. X-Ray Diffraction Analysis (XRD) of powders synthesized during DSC analysis. Specimens containing iron compounds exhibited spectra with reduced intensities. This is most likely due to the fluorescence of iron from Cu k-alpha radiation. Fluorescence tends to reduce peak/background ratios.

Dielectric Measurements

The relative dielectric constant, ϵ'_r , and the loss factor, ϵ''_{eff} , of several of the compositions investigated above were measured at AECL using the cavity perturbation method mentioned previously. Figure 5-8 is the relative dielectric constant as a function of temperature for six of the compositions being investigated as a potential interlayer material. The specimen containing iron (III) oxide had the largest dielectric constant over the temperature range investigated. Figure 5-9 is the same data plotted without the iron (III) oxide so the features of the other curves could be distinguished. For the remaining materials, the curves display similar trends with temperature. In all cases, the dielectric constant decreased until 500°C, then increased steadily up to 1000°C, where it decreased slightly before rising dramatically at temperatures above 1200°C. The dielectric loss factor was measured at the same time as the dielectric constant. Figure 5-10 is the loss factor measured as a function of temperature for the potential interlayer materials. As with the dielectric constant, the loss factor of the specimen containing iron (III) oxide was much greater than the other compositions at temperatures above 600°C. The specimen containing nickel oxide diverged from the range of values measured for the other materials. This effect was not as marked as in the iron (III) oxide specimen. The dielectric loss factor of these two specimens increased steadily with temperature. Figure 5-11 represents the loss factors of the remaining compositions. The trends followed by these compositions varied with temperature in the same manner as the dielectric constants. The loss tangent, $\tan \delta$, for these materials was calculated using equation 2-2. These values are plotted in figure 5-12 as a function of temperature for the potential interlayer materials. The appearance of

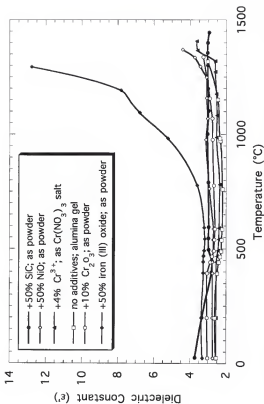


Figure 5-8. Dielectric constant versus temperature of potential interlayer materials. Measured at 2.46 GHz.

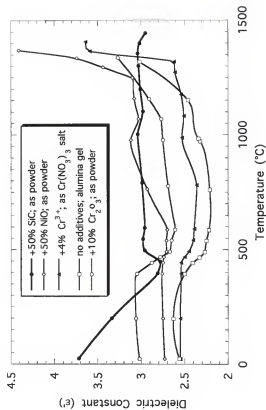


Figure 5.9. Dielectric constants, measured at 2.46 GHz, plotted without the iron (III) oxide composition.

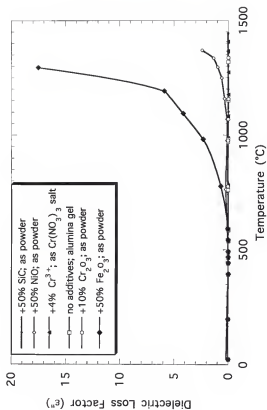


Figure 5-10. Dielectric loss factor, measured at 2.46 GHz, versus temperature for potential interlayer materials.

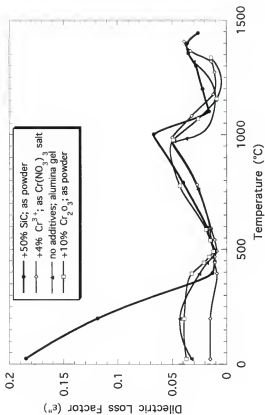


Figure 5-11. Dielectric loss factors plotted without the iron (III) oxide and nickel oxide compositions. Measured at 2.46 GHz.

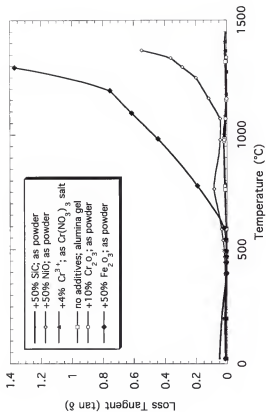


Figure 5-12. Loss tangent, measured at 2.46 GHz, versus temperature for potential interlayer materials.

this set of curves is very similar to that of the curves of the loss factors. The specimens containing iron (III) oxide and nickel oxide display a large increase in the loss tangent with increasing temperature. The plots of the remaining materials, figure 5-13, resemble the curves in figure 5-11.

Microwave Susceptors

The susceptors made with varying amounts of silicon carbide were heated using the setup shown in figure 3-4. Figure 5-14 is the temperature of a 50 gram, 96% pure alumina load placed in the center of the susceptor during heating. The susceptor with no silicon carbide heated to a temperature slightly less than 600 °C. As the volume percent of silicon carbide in the susceptor increased, the maximum temperature attained in the 50 minutes of heating time increased. The susceptor with 30 volume percent silicon carbide reached a temperature of 996°C in the same 50 minute period.

As with the gel-derived ceramic powders, dielectric properties were measured as a function of temperature at 2.46 GHz for specimens made from of each the susceptor compositions. The dielectric constant for each of the susceptors is plotted as a function of temperature in figure 5-15. For all of the compositions investigated, the dielectric constant increased monotonically with temperature. As the amount of silicon carbide increased, the dielectric constant of the material increased for every composition investigated. Figure 5-16 shows the dielectric loss factors of the susceptors measured at the same time as the dielectric constants. The loss factor of the susceptor made without silicon carbide increased monotonically with temperature. In all of the susceptors containing silicon carbide, there was an initial decrease in the loss factor as the temperature increased. As the temperature rose above 400°C, the loss factor increased with increasing temperature. Similar trends were observed in the loss tangents of the susceptors figure 5-17. Figure 5-18 are the temperatures of the susceptors at various times plotted as a function of silicon carbide content.

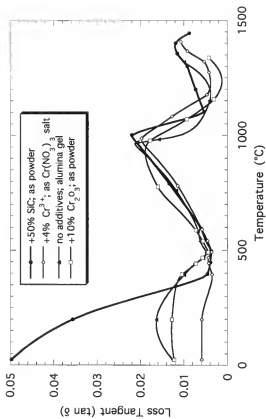


Figure 5-13. Loss tangents plotted without iron (III) oxide and nickel oxide compositions. Measured at 2.46 GHz.

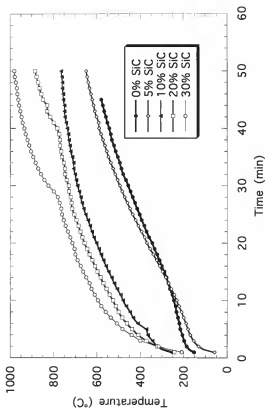


Figure 5-14. Temperature of alumina load in silicon carbide/alumina cement susceptor heated using 3.2 KW with a 75% duty cycle (% time on).

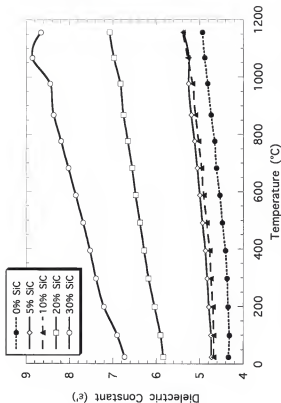


Figure 5-15. Dielectric constant, measured at 2.46 GHz, versus temperature for several compositions of susceptors.

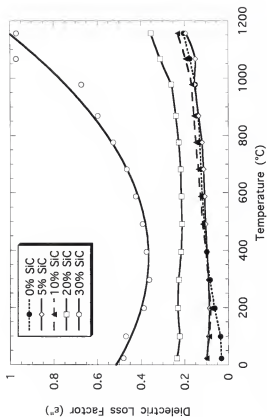


Figure 5-16. Dielectric loss factor, measured at 2.46 GHz, versus temperature for several compositions of susceptors. The minimum in the loss factor, associated with some types of silicon carbide, has yet to be explained.

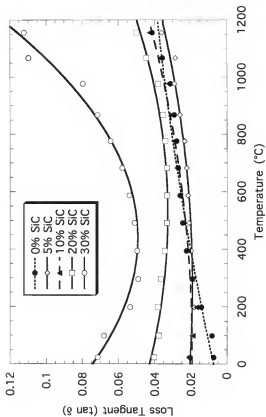


Figure 5-17. Loss tangent for several susceptor compositions at 2.46 GHz.

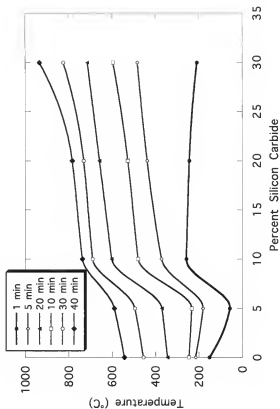


Figure 5-18. Temperature of susceptors as a function of silicon carbide content.

Joining

Joining Conditions

All of the joining experiments were performed using the same protocol. Although processing parameters (time, temperature and pressure) were varied, they were varied in a consistent fashion throughout the study. Figure 5-19 is a typical joining curve used in microwave joining trial #6 (45 min/1450°C/3 MPa/M/NiO). The temperature of the end member closely matched that of the interlayer throughout the entire experiment. The joining temperature of 1450°C was reached in 48 minutes using full power (1000 W*). The joining pressure of 3 MPa was achieved during a 75 second time span. The specimen was unloaded after the 45 minute soak at the processing temperature. Figure 5-20 is the joining curve generated during trial #11 (15 min/1550°C/1 MPa/C/NiO). In the conventional joining operation, data collection of the force and temperature does not begin until the loading procedure has been initiated. In this experiment, approximately 75 minutes were required to reach the processing temperature of 1550°C. This is in contrast to the 56 minutes needed in trial #8 (45 min/1550°C/3 MPa/M/AD94) to reach 1550°C using microwave hybrid heating.

Visual Inspection

After the joining procedure was concluded, the specimens were visually inspected. The specimens that separated easily after the joining process were designated unjoined. This occurred in two instances, trials #1 (15 min/1450°C/1 MPa/M/NiO) and #13 (15 min/1450°C/3 MPa/C/NiO). In both trials the interlayer material was nickel oxide. When the specimens were removed from the microwave, they were easily separated into three parts consisting of the two end members and the interlayer material. The blue color of the joint surfaces was the only sign of any interaction between the end members and the

*Microwave output reported by manufacturer.

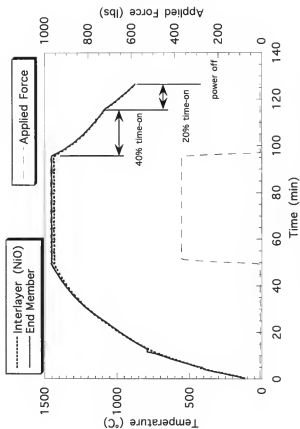


Figure 5-19. Microwave processing conditions for trial #6 (1450°C; 45 min; 3 MPa; nickel oxide interlayer).

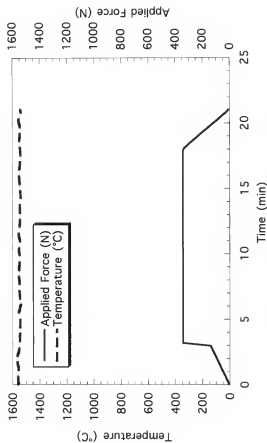


Figure 5-20. Conventional processing conditions for trial #11 (1550°C; 15 min; 1 MPa; nickel oxide interlayer).

interlayer. These two joining experiments were assigned a strength value of zero. Two of the trials joined using a nickel oxide interlayer, trials #4 (45 min/1550°C/1 MPa/M/NiO) and #6, were deemed joined after visual inspection. However, both of the specimens later failed during handling. Figures 5-21 and 5-22 are photographs of the fracture surfaces of the specimens from trials #4 and #6.

Flexure Testing

All of the specimens joined were machined into flexure bars. Bars that did not fail during the machining process were tested using 4-point bending. The first set of bars tested were those joined using various sol-gel compositions as the interlayer material. Table 5-1 presents the joining conditions and the results of these experiments.

Table 5-1. Flexure Strength of AD995 Alumina Joined Under Various Conditions Using Several Different Interlayer Materials*.

Temperature (°C)	Pressure (MPa)	Heating Method	Interlayer Material	Flexure Strength (MPa)	Standard Deviation (MPa)
1500	2.45	microwave	4 mol % Cr-sol	90.8	39.5
1500	0	microwave	as-received	298.9	34.9
1400	1.85	microwave	AD96	184.5	11.2
1500	2.45	conventional	NiO/Al ₂ O ₃ sol	108.4	28.2
1500	2.45	conventional	4 mol % Cr-sol	51.4	20.3
none	0	none	as-received	303.0	19.7

*In all cases, the time spent at temperature was 30 minutes.

Both the as-received alumina and the as-received alumina that was heat treated in the microwave had flexure strengths that were similar to the flexure strength reported by the manufacturer. All of the joined specimens had flexure strengths significantly lower than the as-received alumina. Figure 5-23 is a typical fracture surface of a flexure bar joined using a gel-derived interlayer. During the heating process, the gel shrinks considerably. Consequently, the interlayer material does not cover the entire surface of the end members.

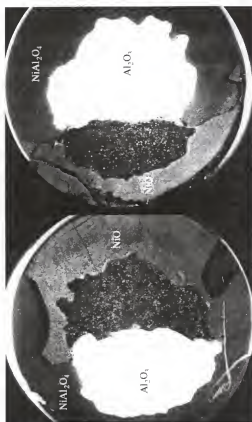


Figure 5-21. Fracture surfaces of specimens from trial #4 (45 min; 1550°C; 1 MPa; nickel oxide interlayer; microwave heated).

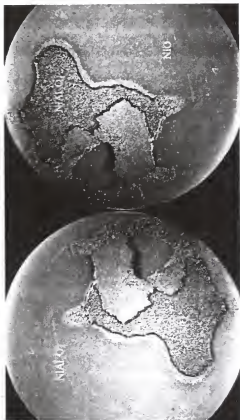


Figure 5-22. Fracture surfaces of specimen from trial #6 (45 min; 1450°C; 3 MPa; nickel oxide interlayer; microwave heated).

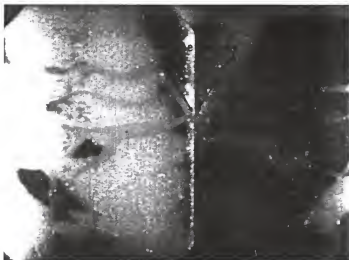


Figure 5-23. Fracture surfaces of a flexure bar joined using a gel-derived (4 mol% Cr_2O_3) interlayer.

The specimen joined using a solid piece of AD96 alumina had a flexure strength of 184.5 MPa, more than 60% of the strength measured in the as-received material.

The next set of experiments considered either AD94 or nickel oxide as the interlayer. AD94 is an alumina material with a dielectric loss greater than the AD96. The other interlayer material, nickel oxide, reacts with alumina to form a nickel aluminate spinel, NiAl_2O_4 . As described in Chapter 3, an experimental design was developed to evaluate the joining parameters statistically, using the flexure strength as the dependent variable.

All of the joints made with AD94 alumina as the interlayer were intact at the conclusion of the experiments. However, trials #2 (45 min/1450°C/1 MPa/M/AD94) and #9 (15 min/1450°C/1 MPa/C/AD94) both separated during the fabrication of the test bars. Other test specimens provided between five and eleven bars for strength testing. For the specimens joined with nickel oxide as the interlayer material, only two specimens, #11 and #15 (15 min/1550°C/3 MPa/C/AD94), were joined sufficiently enough to provide bars for flexure testing. Trials #1 and #13 were unjoined after visual inspection, trials #4 and #6 failed during handling and trials #7 (15 min/1550°C/3 MPa/M/NiO) and #10 (45 min/1450°C/1 MPa/C/NiO) failed during the machining of the bars. Table 5-2 shows the results of the four-point bend testing of the joined bars compared to the as-received material. With the exception of a few bars from trial #15 which broke at the support pins, all the bars failed at the interface between the interlayer and the end member. The highest strength recorded was 273 MPa for a bar from trial #15. The lowest measured strength was 19.2 MPa recorded from a bar in trial #16 (45 min/1550°C/3 MPa/C/NiO). Figure 5-24 is a plot of the strengths with the error bars at one standard deviation. Trial #15 had the highest mean flexural strength at 252 MPa. Trial #11 had the lowest standard deviation (5.0 MPa) and trial #8 had the highest standard deviation (57.3 MPa).

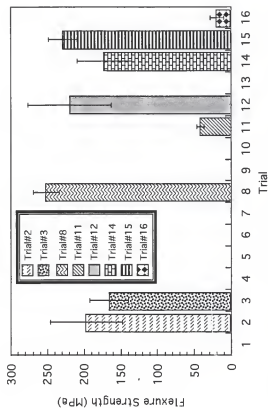


Figure 5-24. Mean flexure strength of bars for each of the trials in the experimental design. Error bars correspond to one standard deviation.

Table 5-2. Mean Strength and Standard Deviation of Bars Joined by either Microwave or Conventional Heating.

Trial	Joining Conditions* time/temperature/pressure/ heating method/interlayer	Strength (MPa)	Standard Deviation (MPa)
1	15/1450/1/M/NiO	0	-
2	45/1450/1/M/AD94	-	-
3	15/1550/1/M/AD94	197	48.8
4	45/1550/1/M/NiO	-	-
5	15/1450/3/M/AD94	166	26.0
6	45/1450/3/M/NiO	-	-
7	15/1550/3/M/NiO	-	-
8	45/1550/3/C/AD94	229	57.3
9	15/1450/1/C/AD94	-	-
10	45/1450/1/C/NiO	-	-
11	15/1550/1/C/NiO	41.6	5.0
12	45/1550/1/C/AD94	172	37.7
13	15/1450/3/C/NiO	0	-
14	45/1450/3/C/AD94	219	19.4
15	15/1550/3/C/AD94	252	17.8
16	45/1550/3/C/NiO	19.2	9.4
AR	-	303	19.7

* time (min); temperature (°C); pressure (MPa); heating method (M-microwave, C-conventional)

Figure 5-25 is a typical fracture surface for a specimen joined with an AD94 alumina interlayer. The interlayer and the end member separated leaving a fracture surface that was very smooth with little in the way of fracture markings on the surface. Figure 5-26 shows the joint line between the interlayer (AD94) and the end member (AD995) in a bar that had a strength of 142 MPa. The joint appears well formed along the majority of the joint line. A closer examination, figure 5-27, reveals a representative portion of the joint area exhibiting porosity, grains for the two surfaces in contact, and grains connected by a grain boundary 0.5 μm thick. Figure 5-28 shows the intact joint in a bar from trial #15 that



Figure 5-25. Fracture surface of specimen from trial #12, representative of all the specimens joined using AD94 alumina as the interlayer material.

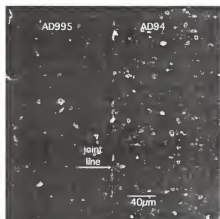


Figure 5-26. Joint line between AD94 alumina interlayer and AD995 alumina end member (250x). Trial #14 (45 min/1450°C/3 MPa/C/AD94).



Figure 5-27. Micrograph of joint region in figure 5-26 showing porosity and grain boundary material (20,000x).

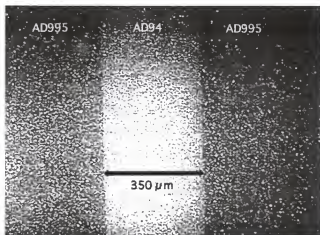


Figure 5-28. Intact interlayer material in bar that fractured away from the joint area. Trial #8 (45 min/1550°C/3 MPa/M/AD94) (6,000x).

failed at a distance away from the interface and had a strength of 220 MPa. The joint region in figure 5-29 seems to have less porosity than that in figure 5-26. Closer examination of the joint regions, figure 5-30, exhibits many of the same features as the specimen in figure 5-27. However, there is evidence of increased contact between the grains of the interlayer and the end member. At this magnification, 20,000x, the joint line is hard to discern because interparticle contact interrupts the continuity of the grain boundary phase that forms the joint line.

The wavelength dispersive spectroscopy feature of the electron microprobe was used to map the presence of silicon near the joint area. It was assumed that all of the silicon present was in the form of silica. An area encompassing the joint, approximately 14 μm by 14 μm , was examined for specimens from trials #2, #3, #8, #12, #14, and #15. Trials #3 and #15 were joined at the same temperature with a force applied for the same duration of time. Trial #3 was joined using microwave energy while trial #15 was joined by conventional heating. Figure 5-31 and 5-32 are micrographs and the accompanying silicon x-ray maps for the area surveyed for both trials. In both instances there appears to be a greater concentration of silica in the joint area than in either the interlayer (AD94) or the end member (AD995). There does not appear to be a noticeable variation between the two specimens in the amount of silica at the joint interface. Trials #2 and #8 were both joined using microwave energy for the same time duration. However, trial #2 was joined at 1450°C whereas trial #8 was joined at a temperature of 1550°C. Figure 5-33 and 5-34 are micrographs and the accompanying silicon x-ray maps for the areas surveyed in the two trials. In the specimen joined at the higher temperature, there is less contact between the grains of the interlayer material and the end member. The x-ray maps also indicate a greater concentration of silica at the joint interface of the specimen joined at 1550°C.

Fracture surfaces of the specimens joined with nickel oxide as the interlayer material varied with the flexure strength of the bars. Figures 5-35 through 5-37 are fracture

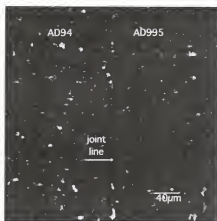


Figure 5-29. Joint region of bar from trial #15, flexure strength 220 MPa (250x). Trial #8 (45 min/1550°C/3 MPa/M/AD94) (6,000x).

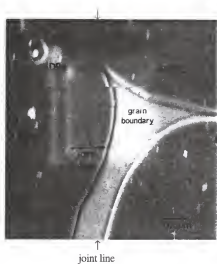


Figure 5-30. Magnified micrograph of the joint line in figure 5-29 (20,000x).

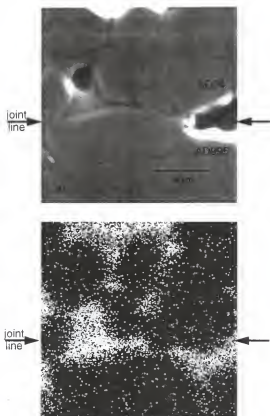


Figure 5-31. Joint area of a bar microwave joined in trial #3 (15 min/1550°C/1 MPa/M/AD94) (6,000x). a) micrograph and b) WDS x-ray map of silicon.

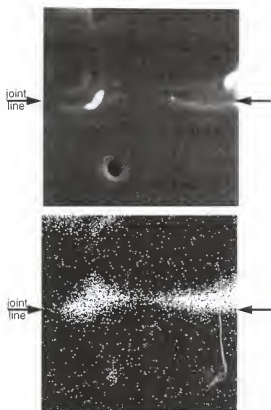


Figure 5-32. Joint area of a bar conventionally joined in trial #15 (15 min/1550°C/3 MPa/C/AD94) (6,000x). a) micrograph and b) WDS x-ray map of silicon.

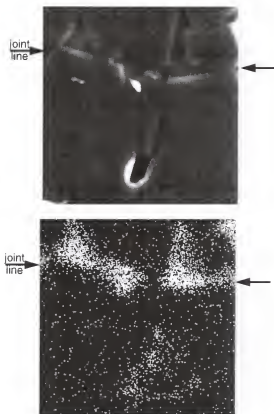


Figure 5-33. Joint area of a bar microwave joined in trial #2 (45 min/1450°C/1 MPa/M/AD94) (6,000x). a) micrograph and b) WDS x-ray map of silicon.

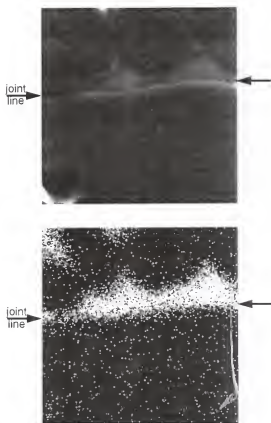


Figure 5-34. Joint area of a bar microwave joined in trial #8 (45 min/1550°C/3 MPa/M/AD94) (6,000x). a) micrograph and b) WDS x-ray map of silicon.

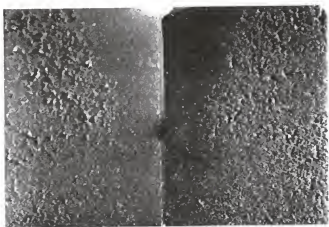


Figure 5-35. Matching fracture surface of bar joined with a nickel oxide interlayer that failed before flexure testing. Compare to Figures 5-36 and 5-37. Trial #11 (15 min/1550°C/1 MPa/C/NiO).



Figure 5-36. Matching fracture surfaces of bar joined with a nickel oxide interlayer with a flexure strength of 38 MPa. Trial #11 (15 min/1550°C/1 MPa/C/NiO).

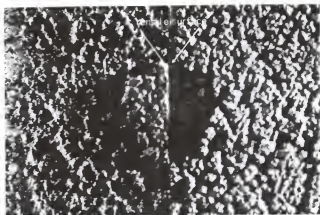


Figure 5-37. Matching fracture surfaces of bar joined with a nickel oxide interlayer with a flexure strength of 45 MPa. Texture difference is due to slow crack growth from controlled loading (slow rate). Trial #11 (15 min/1550°C/1 MPa/C/NiO).

surfaces of bars from trial #11 (15 min/1550°C/1 MPa/C/NiO) that had strengths of 0, 38, and 45 MPa, respectively. Figure 5-38 is a micrograph of the joint region in the specimen with no flexure strength. The presence of a reaction layer between the alumina and the nickel oxide is noted along the entire length of the joint line. The reaction layer is approximately ten microns thick and does not have as much porosity as the nickel oxide. Figure 5-39 is a higher magnification photograph of the same area. The joint area of the bar with a flexure strength of 45 MPa had a reaction layer of a thickness similar to the weaker specimen, figure 5-40. A closer examination of the same area, figure 5-41, indicates that the nickel oxide in contact with the reaction layer is more sound than the nickel oxide in figure 5-39.

The digitized surface profiles of microwave and conventionally joined end members were plotted for a 180 μm length of the joint line, figures 5-42 and 5-43. A similar plot was made for a micrograph of the profile of an as-machined surface, figure 5-44. The roughness of the surface, calculated using equation 3-1, was 0.884 μm for the microwave joined specimen (trial #8) and 1.115 for the conventionally joined specimen (trial #12). The profile roughness calculated for the as-machined surface was 0.535 μm .

Statistical Analysis

To perform an analysis of variances (ANOVA) of the experimental design, the average strength of each of the trials was calculated from the strength of the individual flexure bars. The two trials that did not join at all, trial #1 and #13, were assigned a flexure strength of zero. Six of the specimens that were determined to be joined during visual examination, failed during the machining process. The values of the strengths for these trials were left vacant. There is a provision in the statistical software for uncollectible data that can evaluate the information with missing data. Table 5-3 is the data as input into the analysis program. The program performs a Type III Sum of Squares on the data. This removes the influence of all of the other variables prior to testing the variable in question.

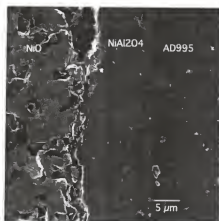


Figure 5-38. Micrograph of joint region of bar from figure 5-35 joined with a nickel oxide interlayer (2,000x). Flexure strength 0 MPa.

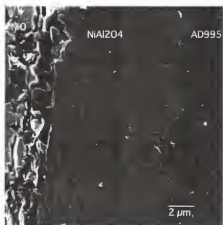


Figure 5-39. Micrograph of joint region of bar from figure 5-35 joined with a nickel oxide interlayer (5,000x). Flexure strength 0 MPa.

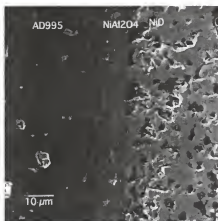


Figure 5-40. Micrograph of joint region of bar from figure 5-37 joined with a nickel oxide interlayer (1,000x). Flexure strength 45 MPa.

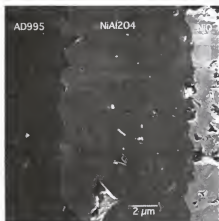


Figure 5-41. Micrograph of joint region of bar from figure 5-37 joined with a nickel oxide interlayer (5,000x). Flexure strength 45 MPa.

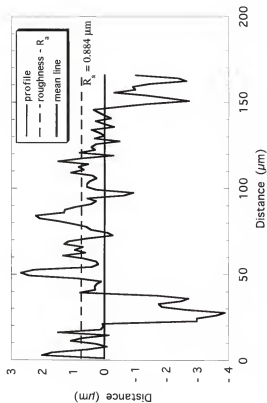


Figure 5-42. Roughness of joined surface (trial #8) calculated from micrograph taken at 500x.

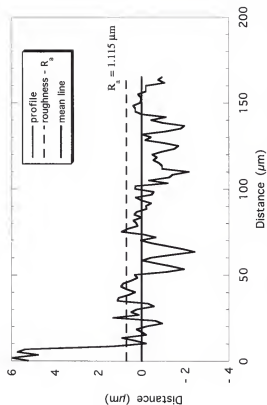


Figure S-43. Roughness of joined surface (trial #12) calculated from micrograph taken at 500x.

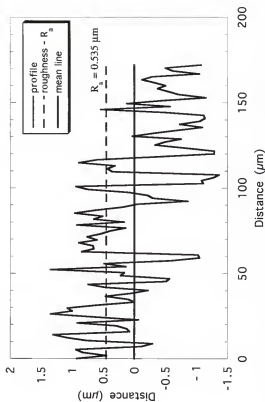


Figure 5.44. Roughness of as-machined surface calculated from micrograph taken at 500x.

Table 5-3. Data Used to Perform ANOVA Analysis.

Name	Time	Temperature	Pressure	Heating Method*	Interlayer	Flexure Strength
Type	Integer	Integer	Integer	Integer	String	Real
Mean	-	-	-	-	-	129.58
Std. Dev.	-	-	-	-	-	102.2
Std. Error	-	-	-	-	-	32.3
Minimum	15	1450	1	C	Al ₂ O ₃	0
Maximum	45	1550	3	M	NiO	252
Range	30	100	2	1	1	252
Sum	-	-	-	-	-	1295.8
Sum of Squares	-	-	-	-	-	261954.2
1	15	1450	1	C	NiO	0
2	45	1450	1	C	Al ₂ O ₃	-
3	15	1550	1	C	Al ₂ O ₃	197
4	45	1550	1	C	NiO	-
5	15	1450	3	C	Al ₂ O ₃	166
6	45	1450	3	C	NiO	-
7	15	1550	3	C	NiO	-
8	45	1550	3	C	Al ₂ O ₃	229
9	15	1450	1	M	Al ₂ O ₃	-
10	45	1450	1	M	NiO	-
11	15	1550	1	M	NiO	41.6
12	45	1550	1	M	Al ₂ O ₃	172
13	15	1450	3	M	NiO	0
14	45	1450	3	M	Al ₂ O ₃	219
15	15	1550	3	M	Al ₂ O ₃	252
16	45	1550	3	M	NiO	19.2

* C - conventional; M - microwave

The full analysis of the data is in Table 5-4. The flexural strength is the dependent variable

Table 5-4. Output of Statistical Analysis of Data from Table 5-3.

Type III Sums of Squares

Source	df	Sum of Squares	Mean Square	F-Value	P-Value
Time	1	294.648	294.648	.297	.6147
Temperature	1	1839.608	1839.608	1.854	.2449
Pressure	1	979.448	979.448	.987	.3766
Heating Method	1	190.821	190.821	.192	.6836
Interlayer	1	64719.362	64719.362	65.241	.0013
Residual	4	3968.020	992.005		

Dependent: Flexure Strength

and the joining parameters (time, temperature, pressure, heating method, and interlayer material) are the independent variables. The null hypothesis is a statement asserting that there are no differences between the values of the dependent variable, flexure strength, caused by the differences in the independent variables. The model assumes a null hypothesis for each of the processing parameters at a significance level of 0.05. This means that in 5% of the analyses, a valid hypothesis will be rejected. The values of interest in Table 5-4 are in the column entitled "F-values". The F-value is a ratio of the mean square of the processing parameter in question to the mean square of the residual. The F-value is compared to the theoretical value generated by the model assuming the null hypothesis is true. If the calculated F-value is larger than the theoretical value, it is assumed the null hypothesis was false; there is a significant influence of the processing parameter in question on the flexure strength. The two F-values are compared to produce a p-value that then can be compared to the level of significance that has been stated earlier in the analysis. Appendix C is a set of sample calculations for a hypothetical series of experiments. According to the results in Table 5-3, the interlayer material is the only processing parameter that exhibited a significant difference on the flexure strength at a 95% confidence interval. Figures 5-45 through 5-49 are comparisons of the means of the flexure strength at the two levels of each independent variable. The graphs are plotted with

Means Table
Effect: Time
Dependent: Flexure Strength

	Bar Count	Mean	Std. Dev.	Std. Error
15	6	109.433	109.312	44.626
45	4	159.800	96.972	48.486

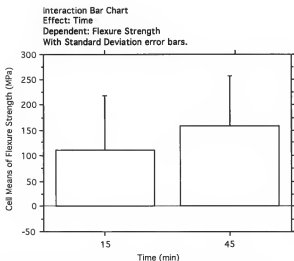


Figure 5-45. Effect of time on the flexure strength of joined bars.

Means Table
 Effect: Temperature
 Dependent: Flexure Strength

	Bar Count	Mean	Std. Dev.	Std. Error
1450	4	96.250	113.227	56.613
1550	6	151.800	98.161	40.074

Interaction Bar Chart
 Effect: Temperature
 Dependent: Flexure Strength
 With Standard Deviation error bars.

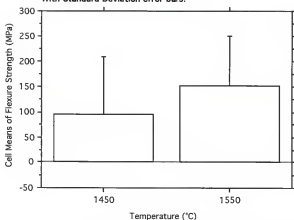


Figure 5-46. Effect of temperature on the flexure strength of joined bars.

Means Table
Effect: Pressure
Dependent: Flexure Strength

	Bar Count	Mean	Std. Dev.	Std. Error
1	4	102.650	96.567	48.283
3	6	147.533	110.665	45.179

Interaction Bar Chart
Effect: Pressure
Dependent: Flexure Strength
With Standard Deviation error bars.

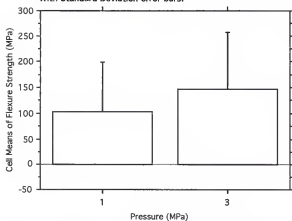


Figure 5-47. Effect of pressure on the flexure strength of joined bars.

Means Table
Effect: Heating Method
Dependent: Flexure Strength

	Bar Count	Mean	Std. Dev.	Std. Error
C	6	117.300	110.084	44.942
M	4	148.000	101.964	50.982

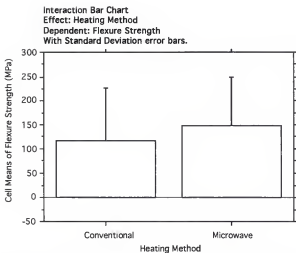


Figure 5-48. Effect of the heating method on the flexure strength of joined bars.

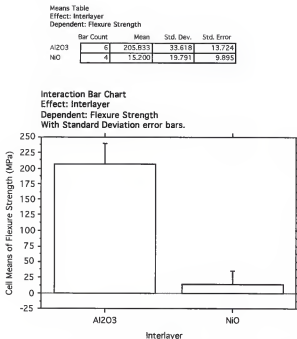


Figure 5-49. Effect of the interlayer material on the flexure strength of joined bars.

error bars equal to one standard deviation of the mean. The graph comparing the means for the two interlayer materials, figure 5-49, is the lone figure where the error bars do not overlap. When the data is evaluated at 90% confidence interval, the difference in heating method does have a statistical effect on the flexure strength, Figure 5-50.

During the machining, the original position in the cylinder of each of the test bars was noted. The positions were designated as either outside, inside, middle or center. Figure 5-51 shows where these designations correlate to their position in the cylinder. Recovery of all of the bars from every joined specimen was not possible. Several of the bars failed during different stages of the machining process. For the joined specimens that were machined, anywhere from two to eleven bars were available for testing. A statistical analysis of the influence of the position of the bar on the flexure strength was performed for each heating method. Table 5-5 shows the results including the effect of the interaction between the bar position and the heating method. Figure 5-52 plots the interaction of the effect of the position of the bar and the heating method on the flexure strength. The table of means in Table 5-6 provides the data used to generate the graph including the number of

Table 5-5. Statistical Analysis of the Effect of Bar Position on the Flexure Strength for both Microwave and Conventional Heating.

Type III Sums of Squares

Source	df	Sum of Squares	Mean Square	F-Value	P-Value
Position	3	13881.092	4627.031	2.172	.1041
Heating Method	1	605.707	605.707	.284	.5964
Position * Heating	3	3580.446	1193.482	.560	.6440
Residual	46	97991.830	2130.257		

Dependent: Flexure Strength

Means Table
Effect: Heating
Dependent: MOR (MPa)

	BarCount	Mean	Std. Dev.	Std. Error	90% lower	90% upper
Conventional	36	150.222	98.504	16.417	122.484	177.961
Microwave	30	210.000	48.492	8.853	194.657	225.043

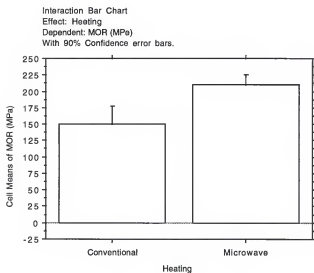


Figure 5-50. Effect of the heating method on the flexure strength of joined bars plotted with error bars at the 90% confidence interval.

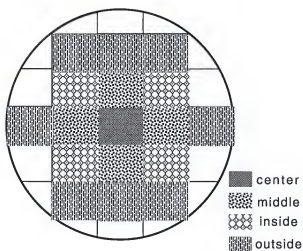


Figure 5-51. Map of original bar positions in the joined cylinder before machining.

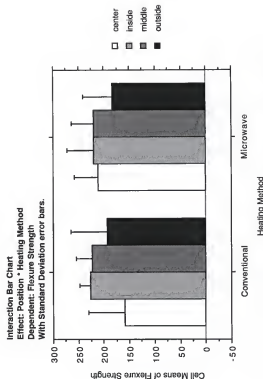


Figure 5-51. Interaction chart showing the combined effect of the position of the bar and the heating method on the flexure strength.

Table 5-6. Effect of Position/Heating Method Interaction on the Flexure Strength.

Means Table

Effect: Position * Heating Method

Dependent: Flexure Strength

	Count	Mean	Std. Dev.	Std. Error
center, Conventional	2	159.500	70.004	49.500
center, Microwave	3	210.333	47.353	27.339
inside, Conventional	9	226.667	20.857	6.952
inside, Microwave	8	220.625	50.737	17.938
middle, Conventional	9	223.556	30.818	10.273
middle, Microwave	11	219.091	45.110	13.601
outside, Conventional	5	193.200	71.304	31.888
outside, Microwave	7	184.143	56.010	21.170

bars at each position. The Type III Sum of Squares uses a weighted average of the number of specimens to account for the different number of bars for each position. The F-values calculated for the position, heating method and the combined influence of the two variables were relatively low.

Numerical Modeling

The procedures detailed in Chapter 4 can be used to generate numerous heating profiles for various heating conditions. Simulations were run for a case in which there is no susceptor, no interlayer, a 500 μm nickel oxide interlayer and a 500 μm AD94 alumina interlayer. In all situations, the model was heated at full power (1000 W) for fifty minutes, the approximate time needed to reach 1550°C in the laboratory. The heating profiles generated in the example in Chapter 4, figure 4-15, provide information as to where the heat is generated and how it is transferred throughout the model. Experimentally, the temperature was measured only at the surface of both the interlayer and the end member. Nodes in the model corresponding to the positions of the thermocouples were monitored for comparison purposes. The positions of these nodes are highlighted in figure 4-14.

The temperature of the workpiece and the susceptor was monitored during microwave heating using thermocouples and an optical pyrometer. Figure 5-53 is the temperature of the workpiece measured simultaneously by the optical pyrometer and a thermocouple. Figure 5-54 is the variation in temperature between the optical pyrometer and the thermocouple. As the heating initially increased, the thermocouple led the pyrometer by as much as 80°C. As the temperature approached the joining temperature, the difference was reduced to less than 30°C. Figure 5-55 is the temperature of the susceptor measured using both a thermocouple and an optical pyrometer. Using the two temperature monitoring methods, the differences measured in the susceptor varied less than in the workpiece, figure 5-56.

The temperature of the interlayer at node 328, calculated for the AD94 alumina is plotted with the measured temperature of the AD94 alumina interlayer in trial #8, figure 5-57. At low temperatures, the measured value at the interlayer is greater than either of the calculated temperatures. As the temperature increases, the measured and calculated temperatures converge. These results are similar to those reported by Thomas et al⁴³. Figure 5-58 is a similar plot for measured and calculated temperatures of a specimen made with a nickel oxide interlayer. Figure 5-59 shows the calculated temperatures at the surface of the joint region, node 328, for the four simulations mentioned earlier. The simulation run with a specimen and no susceptor reached a maximum temperature of 51°C after 50 minutes. The simulation with AD94 as the interlayer material had a temperature profile similar to the case with no interlayer. When nickel oxide was used as the interlayer, the behavior of the interlayer was different. At low temperatures (40°C to 450°C), the temperature of the nickel oxide interlayer was 20°C to 50°C higher than that of the AD94 alumina interlayer. As the temperature of the specimens increased from 450°C to 1200°C, the temperature difference between the materials reached 175°C. Above 1200°C, the difference in temperature of the two interlayer materials gradually decreased until they

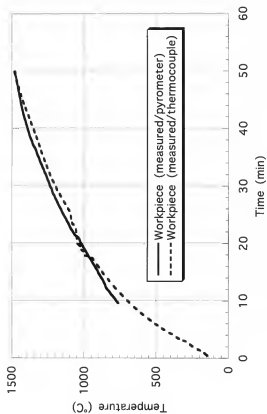


Figure 5-53. Temperature of the workpiece measured using a thermocouple and an optical pyrometer.

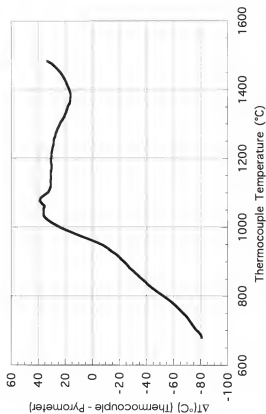


Figure 5-54. Variation in temperature of the workpiece between the thermocouple and the optical pyrometer.

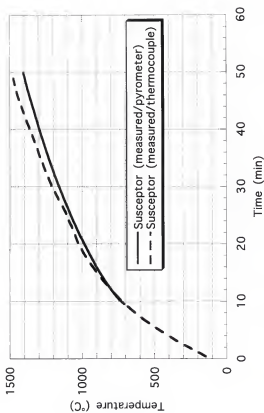


Figure 5-55. Temperature of the susceptor measured using both a thermocouple and an optical pyrometer.

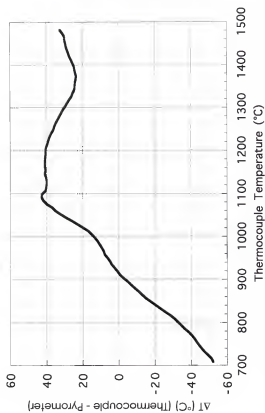


Figure 5-56. Variation in temperature of the susceptor between the thermocouple and the optical pyrometer.

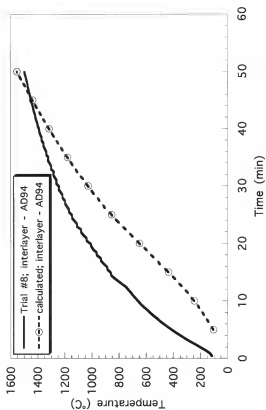


Figure 5-57. Temperature (calculated and measured) at the surface of the AD94 interlayer.

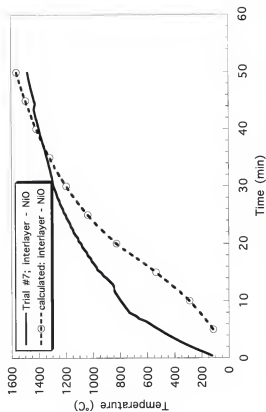


Figure 5-58. Temperature (calculated and measured) at the surface of the NiO interlayer.

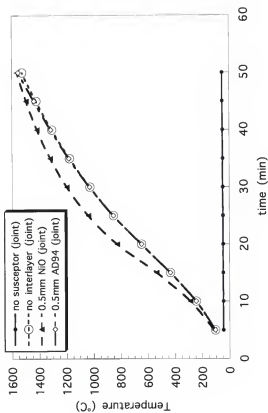


Figure 5-59. Temperature (calculated) at the surface of the joint region for various heating conditions.

converged at 1550°C. Figure 5-60 plots the calculated temperature of the surface of the end member, node 423, for the same simulations in figure 5-59. In all cases, the material at this node is AD995 alumina. As in figure 5-59, little temperature rise was calculated in the simulation using no susceptor. The temperature of the end member calculated for the case with a AD94 alumina interlayer was almost identical to the end member in the simulation that used no interlayer. The difference displayed in the simulation that used nickel oxide as the interlayer material in figure 5-59 is also present in figure 5-60. Although the variation in temperature of the end member is not as pronounced as the interlayer, there is a noticeable spread between the simulations that used nickel oxide and AD94 alumina as the interlayer.

The calculated temperatures are plotted in figure 5-61 for both the interlayer and the end member in the simulation that used AD94 as the interlayer. Node 328 is AD94 alumina and represents the interlayer and node 423 is AD995 alumina and represents the end member. The calculated temperatures at the two positions were similar for the entire heating period. A similar plot was done for the simulation that used nickel oxide as the interlayer, figure 5-62. In this plot, the material represented by node 328 is nickel oxide. As the specimen was heated to 450°C, the temperature of the interlayer was similar to the end member. The temperature of the interlayer rises faster from 450°C to 1200°C than that of the end member. As the simulation continues, the temperatures of the interlayer and the end member converge. Figure 5-63 is a plot comparing the calculated temperature of a nickel oxide interlayer 0.5 mm thick with one 5 mm thick. Initially, the thicker interlayer heats much faster. As the simulation progresses, the temperature of the thinner interlayer eventually exceeds that of the thicker nickel oxide piece.

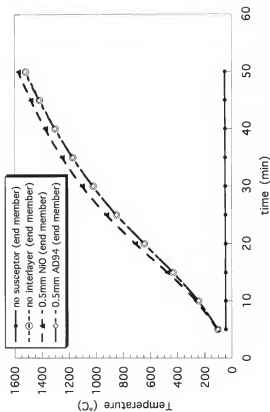


Figure 5-60. Temperature (calculated) at the surface of the end member for various heating conditions.

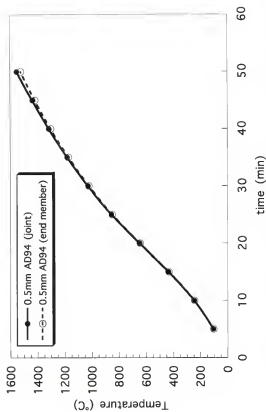


Figure 5-61. Temperature (calculated) at the surface of the joint region (AD94) and end member (AD995).

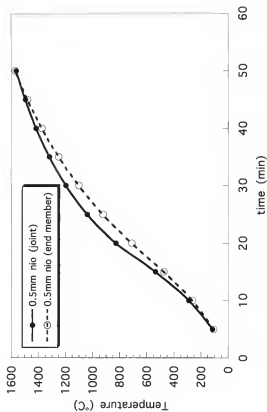


Figure 5-62. Temperature (calculated) at the surface of the joint region (NiO) and end member (AD995).

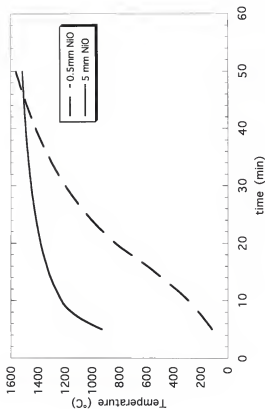


Figure 5-63. Comparison of calculated temperatures for specimens heated with nickel oxide interlayers of different thickness.

CHAPTER 6

DISCUSSION

In Chapter 2, a survey was performed using available literature pertaining to microwave processing of materials and materials joining. Chapters three and four specified a course of experiments based on the information gathered in Chapter 2. The intent of the experiments was to broaden the knowledge in the area of microwave joining of materials. In Chapter 5, the results of the experiments designed in Chapters 3 and 4 are presented. In this chapter, the results are reviewed and explanations are presented that may account for these results. The rationale presented is compared and contrasted to discussions presented in the literature evaluated in Chapter 2.

Phase One

Phase one of the experimental procedure involved the investigation of potential interlayer materials for the joining portion of the research. Several different compositions of gel-derived powders were produced and analyzed to determine their potential as an interlayer.

Machined Surfaces

The roughness of the machined surfaces that were in contact for the joining procedures were in the range of 1.0 μm to 3.0 μm . These numbers are within the parameters set forth by Villagio⁶⁴. The 3-dimensional surface plots in figures 5-2 and 5-4 indicated that there was a textured surface that could promote the interlocking of asperities without inducing significant interfacial porosity during joining.

Sol-Gel Interlayers

The initial rapid heating to 400°C of all of the gel pellets during stand alone heating is related to the removal of the free water and structural water present in the gel. The rise in temperature slowed as first the free water, and then the bound water were eliminated. As described in equation 2-3, the power absorbed in a material is proportional to the dielectric loss factor of the material. The dielectric loss factor for all of the gels, figure 5-11, is relatively high at room temperature and decreases steadily to a temperature of 500°C. The continued rise in the temperature of the gels can be attributed to the consistent increase in the dielectric loss factor with temperature. After the maximum of 841°C was reached, the pellet containing 10 mol% iron (II) oxide experienced a decrease in temperature. This can be associated with the oxidation of iron (II) oxide to iron (II,III) oxide. The further oxidized iron is a less efficient microwave absorber than the iron (II) oxide. Visual inspection of the pellet after heating showed it to be red, supporting the speculation of additional oxidation.

All of the DSC traces exhibited endothermic peaks corresponding to the removal of bound water between 75°C and 150°C and to the removal of structural water between 425°C and 500°C. The exotherm between 525-550°C, present in the sample containing 50 mol% silicon carbide, is due to the oxidation of free carbon in the silicon carbide⁹. The base gel, the gel with 50 mol% nickel oxide and the gel with 50 mol% silicon carbide all displayed exotherms near 1160°C. This exotherm results from the formation of alpha-alumina. In the gel containing chromia, the exotherm corresponding to the crystallization of alpha-alumina occurred at 1207°C. The partial substitution of chromia for alumina distorts the crystal structure, causing the peak to appear at higher temperatures. In the DSC trace of the gel containing 50 mol% iron (II) oxide, two overlapping peaks appeared in the temperature range where crystallization is expected. This specimen was the only one that revealed an endotherm near 1350°C. Examination of the iron (II) oxide/alumina phase diagram, figure

6-1, shows a eutectic between 1300-1350°C. The formation of a liquid phase is possible in an iron (II) oxide rich environment (>10 wt% alumina). The presence of a liquid phase and flowing air led to an increased oxidation of the iron to the 3+ state.

X-ray diffraction analysis was performed on the four compositions heated to 1400°C in the DSC. A second sample of the gel containing 50 mol% iron (II) oxide was heated in the DSC to 1200°C, a temperature lower than that at which the endotherm occurred. The peak positions of the base gel's x-ray diffraction pattern corresponded well to the peak positions published for alumina. This was confirmation that the method for producing alumina was acceptable. The nickel oxide containing specimen had peaks corresponding to alumina, nickel oxide and nickel aluminate spinel. The presence of alumina and nickel oxide are a result of the incomplete reaction of the two materials. This is understandable since the specimens were heated at 40°C/min. In the specimen containing chromia, all of the peaks present coincided well with the reference peak for alumina but the peak positions were all shifted to a smaller angle. This is due to the chromia entering the alumina as a solid solution. Chromium has a larger ionic radius than aluminum. When chromium is substituted for aluminum in the crystal lattice, the spacing between the lattice planes increases. This produces an increase in the d-spacing of the lattice. Applying Bragg's Law,

$$n\lambda = 2 \cdot d \cdot \sin(\theta) \quad (6-1)$$

it is apparent that the x-ray peaks are shifted to smaller 2θ values. In the specimen made with iron (II) oxide heated to 1200°C, peaks matching iron (II) oxide/alumina spinel, alumina and iron (II) oxide were identified. As with the specimen containing nickel oxide, the rapid heating in the DSC did not provide sufficient time for a complete reaction to occur. Additional oxidation of the iron was predicted from the results of the stand alone heating experiments. The x-ray diffraction pattern of the iron (II) oxide specimen heated to

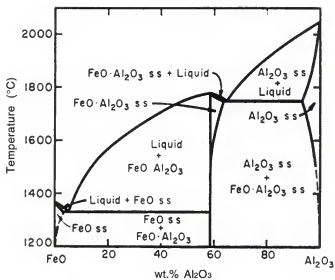


Figure 6-1. Phase diagram of the FeO-Al₂O₃ system¹²⁰.

1400°C exhibited only peaks indicating the presence of alumina and iron (III) oxide. This is a result of the complete oxidation of the iron (II) oxide to iron (III) oxide.

As a function of temperature, the dielectric constant and the dielectric loss factor display similar trends for all of the gels examined. The decrease in the dielectric loss from 25°C to 500°C is associated with the removal of free and structural water. The ensuing increase in the loss factor is due to the typical behavior of a dielectric material with increasing temperature. Figure 6-2 is a qualitative graph of the typical loss factor versus temperature for a dielectric material. The figure illustrates the effect of increasing temperature on the effective loss factor. During the microwave heating of dielectric materials, an increase in the effective loss factor results in an increase in the materials ability to absorb energy. This leads to a rise in temperature and subsequently, an increase in the effective loss factor. These related increases in the effective loss factor and temperature often lead to a condition known as thermal runaway. Thermal runaway is defined by Metaxas and Meredith⁵ as the uncontrolled temperature rise in a material heated by high frequency energy due to a positive rate of change of the effective loss factor with temperature. As the materials are heated further, the loss factor experiences another decrease from 1000°C to 1200°C. This is probably caused by the ordering that the materials undergo during crystallization. Key features of the loss factor, figure 5-11, take place at temperatures similar to those seen in the DSC traces, figure 5-6. In the present investigation, thermal runaway was prevented by controlling the duty cycle of the microwave generator through the use of a setpoint controller.

Summary of Phase One

The two gel-derived materials that were for use in the joining experiments were the gel containing 50 mol% nickel oxide and the gel made with 4 mol% chromium salt. The gel containing iron (II) oxide heated well but was eliminated from consideration due to its

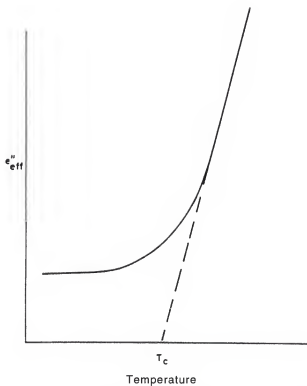


Figure 6-2. Qualitative representation of the effect of temperature on the dielectric loss factor of a typical dielectric material. T_c refers to the critical temperature at which the efficiency of the absorption of microwaves increases dramatically⁵.

unstable oxidation characteristics. Silicon carbide was discounted as a potential additive for two reasons. First of all, the silicon carbide addition did not provide a significant increase in heating ability during stand alone heating. Secondly, silicon carbide did not form any intermediate phases with alumina that could contribute to the joining process.

Phase Two

In the second phase of the research, microwave susceptors were developed in order to provide the energy necessary to attain joining temperatures on a consistent basis. The design, construction and implementation of a microwave joining apparatus was also a major topic of phase two of the study. The gel containing 50 mol% nickel oxide and the gel made with 4 mol% chromium salt were the interlayer materials used in this portion of the investigation.

Microwave Susceptors

The temperature of all of the susceptors increased monotonically for the entire heating experiment. The susceptor made with 5 vol% silicon carbide maintained a higher temperature than the susceptor made entirely of cement. The difference, however, was not proportional to the temperature differences attained by the susceptors made with more silicon carbide. The dielectric constants for all of the susceptor compositions were almost linear with respect to temperature. The dielectric loss factor for the 0, 5, and 10 vol% susceptors had values that were similar to each other. When the volume percent of silicon carbide was increased to 20%, the value of the dielectric loss factor increased two-fold. All four of these compositions exhibited dielectric loss factors that were not significantly influenced by changes in temperature. The dielectric properties of these susceptors are governed by the alumina cement. In the susceptor made with 30 vol% silicon carbide, there was a sufficient quantity of silicon carbide present to influence the dielectric loss factor and the heating behavior. The increase in the dielectric loss factor above 600°C is reflected in a rapid increase in temperature of the susceptor near 800°C, figure 5-14. The

plot of temperature as a function of silicon carbide for several times, figure 5-18, provided some unanticipated results that are more easily understood when viewed in conjunction with the dielectric properties of the susceptors. Small additions of silicon carbide, 5 vol%, did not significantly improve the ability of the susceptor to heat. The superimposed dielectric loss factor curves for the 0 vol% and 5 vol% silicon carbide susceptors suggest that this behavior can be expected.

Microwave Joining Apparatus

The description and photograph of the microwave joining apparatus described in Chapter 3 is the current version of a piece of equipment that has been evolving since this study began. Significant challenges were involved in the modification of the microwave oven. The greatest challenge was to provide as uniform a microwave field as possible so that consistent joining results could be obtained.

The joining experiments performed in phase two of the research accomplished two tasks. First, they demonstrated the viability of producing specimens joined using microwave energy (one of the original objectives). The second accomplishment of the joining experiments in phase two was to dismiss gel-derived materials as potential interlayers. This decision was made partly because the measured flexure strengths were not in the range of the as-received material. More importantly, as seen in figure 5-23, the shrinkage that occurs in the gel interlayer during heating markedly decreases the area available for joining. The temperatures and times used in these experiments did not induce sufficient creep to provide the contact necessary to develop a complete joint. Additionally, the relative thinness of the gel interlayer does not take full advantage of the potential for volumetric heating in the microwave joining experiments.

Summary of Phase Two

The development and characterization of the silicon carbide/cement susceptors contribute to the resources available for researchers working with microwave hybrid

heating. The microwave joining apparatus has proved to be a reliable piece of equipment capable of attaining temperatures upwards of 1550°C and applying forces of 2 kN.

The elimination of gel-derived materials led to the introduction of densified materials as potential interlayers. Nickel oxide was retained as an interlayer material for its reactivity with alumina. Near dense (80% theoretical) disks are used in phase three of the research effort. The second material used as an interlayer for phase three was 94% pure alumina. The significant amount of impurities present in this alumina should provide an increase in microwave absorption over the high-purity alumina used as a base gel. The increase in absorption is ascribed to the high dielectric loss factor of the glassy grain boundary phase by Binner⁷⁴.

Phase Three

In phase three of the study, a statistical analysis was performed on the results gathered from a course of joining experiments designed to evaluate the influence of processing parameters on the flexure strength of alumina butt joints. The fracture surfaces and joint areas were evaluated using SEM, WDS and image analysis.

Experimental Design

The purpose of an experimental design is to provide an organized set of experiments that will aid in the interpretation of the results. The use of the experimental design requires advance consideration of the goal of the experiments and the steps needed to achieve that goal. The subsequent statistical analysis of the experimental observations affords an unbiased interpretation of the results. A factorial design allows for evaluation of several factors that are varied throughout the experiments. This design method also affords the use of a minimum number of experiments. This is desirable when the cost of the experiments becomes prohibitive. This can occur through expenses stemming from either materials, machining or equipment usage.

In this research, a one-half factorial experimental design was used to determine the effect of the processing parameters in question on the flexure strength of the joined alumina. The five processing parameters considered to be the most influential on the flexure strength were identified. Two levels of each parameter were chosen based on conventions gleaned from the literature.

Joining Experiments and Flexure Tests

During the microwave joining experiments, the temperature of the specimen increased steadily until it reached the temperature used for joining. Based on the information in figure 6-2, there should be a temperature at which the efficiency of the workpiece to absorb microwaves increases drastically. At this point, the temperature of the workpiece should increase commensurately with the microwave absorption. This was not the situation recorded in figure 5-20. The dielectric loss factor of the AD995 alumina remains low even up to the temperatures used for joining in this study. If this is the case, the majority of the heat in the microwave joining experiments was generated in the susceptor and transferred to the workpiece via radiation and convection. The similarity in the temperature of the AD995 alumina end member and the interlayer materials that were supposedly more absorptive, is evidence that this is probably the circumstance.

The only confirmation that a reaction occurred between the nickel oxide interlayer and the end members of the two specimens that did not join at all during the experiment was the coloration of the contact surfaces. The blue surfaces are indicative of the formation of nickel oxide/alumina spinel, NiAl_2O_4 . In the specimens that failed during handling that were joined with nickel oxide, figures 5-21 and 5-22, the residual nickel oxide that was exposed suggests that in addition to a debonding at the interface, failure also occurred through the bulk of the interlayer. From an examination of the figures, it is evident that the relative roughness of the fracture surface increases with increasing fracture strength. The specimens joined with nickel oxide that were strong enough to tolerate the applied

machining stresses then were tested in four-point bending. Figure 5-35, a bar that failed prior to testing, debonded at the nickel oxide-alumina interface. All of the bars joined with a nickel oxide interlayer failed through the bulk of the nickel oxide. Nickel oxide is not considered a structural ceramic and no strength data is available in the current literature. The difficulty in producing dense nickel oxide contributes to the likelihood that the specimen will fail through the interlayer. Figures 5-36 and 5-37 are typical fracture surfaces observed in specimens with nickel oxide interlayers. The fracture surfaces are highly textured but do not provide any insight into the fracture strength of the specimens. The reaction layer was consistently eight to ten microns thick for all of the flexure bars examined. Any spinel formation requires the solid state diffusion of either nickel or aluminum through the spinel layer. As the reaction layer forms, the reactants (Al_2O_3 and NiO) are separated by an ever increasing distance in the form of the spinel. At some time, the formation of the spinel phase is essentially halted. For experiments of the time durations evaluated in this research there exists a maximum spinel thickness that can be utilized for the range of processing conditions used in this study. Based on the reaction layer thickness at both end member-interlayer interfaces, this maximum usable thickness of nickel oxide is 15-20 μm . Any more nickel oxide present will go unreacted and ultimately lead to the failure of the specimen. The strength of the flexure bars is determined by the nickel oxide-spinel interface. The micrographs in figures 5-39 and 5-41 illustrate this point well. In both figures, the alumina-spinel interface was continuous. The nickel oxide-spinel interface was poorly formed on the other side of the reaction layer of the bar that failed before testing.

The fracture surfaces for specimens joined with AD94 alumina as the interlayer material had few features for discussion. In these specimens, an abrupt change in the microstructure and elongated porosity were characteristic features of the joint line. When the joint line was examined using higher magnification, grains from the end member and

the interlayer were separated by a glassy phase that extended the entire length of the joint line, figures 5-27 and 5-29. Binner et al.⁷⁴, joining low purity alumina under similar conditions, reported comparable findings and suggested that this is the grain boundary material that has been "squeezed" out of the lower purity alumina during processing. X-ray maps of the joint line, created using wavelength dispersive spectroscopy, indicated that silica is the predominant interface material. Silica is the major impurity in the AD94 interlayer material. This supports the statement by Binner et al.⁷⁴ that the interface material did indeed originate in the grain boundaries of the AD94 alumina. Some grain-to-grain contact between the end member and interface was observed, but the majority of the interface was filled with this silica rich phase. Failure along this interface seems likely and may be the reason there is no appreciable texture to the fracture surfaces. Another observation made by Binner et al.⁷⁴ was the appearance of this glassy phase on the outside surface of the joint. This phenomenon was not observed in this study. There are two contributing factors that would lead to this contrast in results. The first factor is the joining temperatures used. Although the temperatures used by Binner et al.⁷⁴ were in the same range as the temperatures used in this study, overall, those used by Binner were nominally higher, leading to a more fluid liquid phase. The second factor is the purity of the alumina used in the research. The alumina used by the authors in the experiments that provided contrary results was 85% pure alumina and contained more silica for liquid formation. This is in comparison to the 94% pure alumina used in this study.

The roughness measured from profiles of joined surfaces was influenced by the presence of the silica rich phase at the interface. Where the as-machined profile varied consistently across the length investigated, the profiles of both joined specimens have regions of small variations and regions of large variations. This can alter the interpretation of the reported profile roughnesses. The large variations experienced in both the

microwave and conventionally joined specimens were caused by reactions during processing and by artifacts introduced during sample preparation. The processing related variations are due to incursions of the silica rich phase around the surface grains of the end member. The sample preparation artifacts are caused by pullout of interface grains during polishing of the specimens for microscopic analysis.

Statistical Analysis

The mean strength of the bars microwave joined in trial #8 was 83% of the value reported for the unjoined material. These strengths are comparable with those reported for alumina by other authors. Not all of the bars failed at the joint area. A small number of microwave joined bars failed within an end member. This result suggests that some of the joints may have been as strong as the machined bulk material. This phenomenon may also have had an effect on the statistical analysis, leading to the assertion that there is no significant difference between the conventional and microwave heating methods.

For the processing conditions of time, temperature and pressure, the significance of the two levels is determined by the values chosen for each level. The heating method and the interlayer material cannot be influenced by the magnitude and difference between the two levels. This means that by adjusting the values of the levels of the experiment, the significance of a condition can be dictated. Joining experiments carried out with longer times, higher pressures or higher temperatures should eventually produce results that would be considered significant. This reasoning initially appears sound. However, when the effect of time and pressure on strength is examined, figures 2-14 and 2-15, the benefit of increasing the time and pressure decreases. The temperature range for joining is also limited. On the low end joining may not occur, and on the high end melting or creep can interfere with the joining process. For this materials system it then becomes uncertain whether a statistical significance for any of these parameters can be introduced.

The processing parameter that had a significant effect on the flexure strength of the bars was the interlayer material. The low strengths measured for the bars made with nickel oxide signified that further analysis should be done without the nickel oxide data. This treatment, called blocking, permits the removal of all data associated with one level of a processing parameter. In this case the nickel oxide level of the interlayer parameter was removed and the statistical analysis was performed only on the specimens joined using AD94 alumina as the interlayer material. In the blocked analysis, as in the complete one, no significance between the levels of any of the processing parameters was observed at a 95% confidence level. When the data were evaluated at a 90% confidence level, there was a significant difference in the mean flexure strength of specimens joined using different heating methods. Overall, the specimens joined using microwave energy had a flexure strength higher than those joined by the conventional heating method.

One of the touted benefits of microwave processing is volumetric heating. That is, uniform distribution of energy throughout the volume of the workpiece leading to relatively uniform temperature profiles. The statistical analysis, performed to determine the effect of position of the bar on flexure strength, divided the joined specimens into four sections. No significant differences in strength were observed when the heating method was compared for a certain position at the 95% confidence level. This was true for all four of the positions evaluated. Flexure strength also was compared among positions within a heating method. Again, no significant differences in the strength were noticed. However, the bars from the center position of the microwave heated specimen were stronger the bars from the center position of conventionally joined specimens. These results suggest that there may be some volumetric heating occurring, but in the case of the low dielectric loss AD995 alumina, not a sufficient amount to provide a statistical difference at the 95% confidence level.

Summary of Phase Three

The experimental design developed in phase three facilitated an organized approach to produce an unbiased evaluation of the effect of several processing parameters on the joining of high-purity alumina. The parameters investigated were those most commonly varied in joining experiments: time, temperature and pressure. In addition, the effects of heating method and interlayer material were observed.

Under certain conditions, adequate flexure strengths were achieved in specimens joined by both microwave and conventional heating. However, the only processing parameter that produced significant variation in flexure strength was the interlayer material. The small number of bars from each trial available for flexure testing limit the conclusiveness of the statistical analysis. There is little evidence provided to support the concept that volumetric heating by the direct coupling of microwaves to the workpiece contributes to the overall temperature in the notably low dielectric loss AD995 alumina.

Phase Four

Phase four of this study was dedicated to developing a model that could be used to predict the heating behavior of materials in a microwave field. Laboratory heating experiments were performed in support of the modeling work to provide a basis for comparison of the temperatures calculated during the computer simulation.

Experimental Support

The experiments performed in support of the model development consisted of measuring the temperature of the workpiece and susceptor during the heating process. At temperatures near the point at which the optical pyrometer becomes functional ($>600^{\circ}\text{C}$), the pyrometer recorded higher temperatures than did the thermocouple. This is probably an artifact of the way temperature is measured with an optical pyrometer. Unlike thermocouples, which convert the energy of the material they are in contact with into a voltage, optical pyrometers convert the intensity of light emitted or reflected from a surface

into a voltage. In the joining experiments, the thermocouple is always measuring the temperature of the surface of the workpiece. Due to the fact that the susceptor initially heats much faster than the workpiece, the pyrometer is measuring the temperature of the reflection of the susceptor off the face of the workpiece. The temperature measured by the thermocouple eventually exceeds that measured by the pyrometer. This is caused by the measuring techniques and properties of the materials. The thermocouple accesses the workpiece through a small hole in the insulation and the susceptor. The optical pyrometer needs a larger hole in both the exterior insulation and the susceptor to view the workpiece. The absence of susceptor material apparently produces less heat in the area near the workpiece where the pyrometer is focused. In addition, there is an opening in the insulation that provides uninterrupted access between the workpiece and the much cooler environment. As presented in figure 4-12, the emissivity of alumina decreases considerably with increasing temperature. Modern pyrometers are equipped to compensate for variations in the emissivity of the material. However, the low emissivities associated with a very smooth alumina surface cannot be fully compensated for by the pyrometer.

In the experiments measuring the temperature of the susceptor, the rough surface of the cement and the imbedded silicon carbide granules provided an adequate surface for measuring the temperature accurately with the optical pyrometer. The differences here are attributed to the exposure of the outside of the susceptor to the environment.

Computer Simulations

The data input for the model used in the computer simulations was based on physical, thermodynamic and electromagnetic properties of the materials used. Data pertaining to the above mentioned properties were unavailable for some materials. In these instances, the properties of a material with a similar composition were substituted. In the situation where the composition of the material contains a nominal amount of a second element, the properties of the pure material are used. When the material contains porosity,

properties such as heat capacity and absorbed power were adjusted to reflect the smaller mass of material.

The heating profiles generated during the computer simulations have an S-shaped curve. This feature is more prominent in the simulations using nickel oxide as the interlayer material. This behavior can be related back to the shape of the power absorption curves corresponding to the materials in the model. These curves generally exhibit an increase in power absorption as a function of temperature. The effect of the power absorption on the heating behavior is counteracted in part by the heat transfer properties of the model. Energy is removed from the system in the form of heat in proportion to the fourth power of the temperature gradient between the surface of the model and the environment. This is the reason for the flattening out of the temperature profile as temperature is increased. This behavior also was present in the experimental heating curves. Only small differences in temperature were calculated between the interlayer material and the end member. Even though the interlayer material in the simulation, either AD94 alumina or nickel oxide, absorbed a great deal more power per unit volume than the AD995 end member material, there was not enough interlayer material to significantly affect the temperature of the workpiece. The heating behavior in the simulation conducted with a five millimeter nickel oxide interlayer suggests that this is the case. A five millimeter thick nickel oxide interlayer for joining may provide improved heating near the joint. However, the mechanical properties of such a joint would be poor. Characteristically poor mechanical properties were measured in joints made with nickel oxide interlayers 150 μm thick.

The greatest disparity between the calculated and measured temperatures occurs in the first few minutes of heating when the temperature of the workpiece increases rapidly. In this temperature range, the calculated temperature lags and requires several minutes to reach the same value as the measured temperature. This may be due to the platinum thermocouple sheath acting as an antenna, concentrating the microwave field near the tip.

This is more likely to happen at lower temperatures where the efficiency of the absorption of microwaves by the workpiece, insulation and susceptor is at its lowest. As these materials begin to absorb more of the microwaves, there is less of a tendency for the thermocouple tip to interfere with the microwave field.

Summary of Phase Four

Temperature profiles calculated using the model assembled in Chapter 4 were compared to experimentally measured temperatures. Nodes where the temperatures were calculated in the model were carefully selected to correspond to the position where the experimental temperature measurements were made. Simulations were performed to compare the effect of interlayers of differing composition and thickness on the heating of the workpiece. Interlayers 500 μm thick of nickel oxide and AD94 alumina contributed little to the overall calculated values. When the interlayer thickness of nickel oxide was increased to five millimeters, a noticeable change was observed in the heating behavior of the interlayer.

Comparisons made between calculated and measured temperatures indicated that the model used can provide qualitative information pertaining to the heating behavior of materials in a microwave field. The ability to qualitatively predict the heating behavior in a system of materials in a microwave field can be applied to experimental designs. Simple experiments can be used to gauge the temperature profiles that can be expected during the experiment. Such experiments would include estimations of the electric field in a microwave cavity, the electromagnetic and thermophysical properties of the materials along with the geometric configuration of the assembled materials to be heated. The implementation of a microwave heating model can assist in eliminating the trial and error experimentation that has been associated with microwave processing of materials.

CHAPTER 7

SUMMARY AND CONCLUSIONS

The goal of this study as introduced in Chapter 1 was to provide experimental data coupled with numerical models that serve to further the understanding of the interactions between microwave energy and alumina ceramics, as well as how these interactions influence the mechanical behavior of joined materials.

The literature survey in Chapter 2 provided background information on microwave interactions with materials. Additional reviews of papers covered the fundamentals of materials joining and summaries of joining experiments performed using conventional or microwave heating were provided.

Chapter 3 discussed the experimental work required to accomplish the goal of this study. The issues that were addressed ranged from equipment development to experimental organization. The chapter also included a description of the analytical methods used to evaluate the joined specimens.

A numerical model for modeling heat flow was developed in Chapter 4 to simulate the heating profiles generated during the heating of ceramics using microwave energy. The use of models to simulate microwave heating can provide information regarding the probable heating behavior of ceramics prior to the actual experimentation. The temperature at nodes in the model corresponding to the position of the thermocouples in the laboratory experiments was monitored. These temperatures were later used to compare the simulated temperatures to the temperatures that were determined experimentally .

Chapter 5 provided the results of the experimental work described in Chapters 3 and 4. The outcome of the experimental work was presented in a series of graphs and tables. These were accompanied by a description of the data with an emphasis placed on the most significant issues.

In Chapter 6, a discussion of the results was presented. The materials system investigated consisted of materials that are generally considered microwave transparent. This is due to the low dielectric loss factor of alumina and the resulting large penetration depth. If the penetration depth remain sizeable at high temperatures, insufficient amounts of microwave energy will be absorbed and heating will not occur. The introduction of a strong microwave absorber as an interlayer material did not provide a sufficient volume of microwave absorbing material to influence the low dielectric loss alumina end members. Although the objective of demonstrating induced enhancements due to microwave processing remains a challenge, it is clear that joining other materials systems that interact with microwaves more vigorously than the high-purity alumina used in this study is possible.

Important points discussed in Chapter 3, 4 and 5 the study are listed below by chapter.

Chapter 3

- An apparatus for joining ceramics using microwave energy was designed and fabricated.
- Susceptors for microwave hybrid heating were developed and tailored to work at temperatures up to 1550°C.
- Processing temperatures in excess of 1500°C could be reached in less than 45 minutes (several minutes faster than a conventional furnace).
- Sample cooling can be controlled with ease to fit any temperature profile.

- Laboratory experiments were performed to provide comparable heating conditions to evaluate the effectiveness of the numerical model used.

Chapter 4

- A geometric model was constructed incorporating the physical dimensions, physical, electromagnetic and thermodynamic properties of the materials being investigated.
- Numerical modeling was employed to approximate heat flow during microwave hybrid heating.

Chapter 5

- X-ray diffraction analysis confirmed the validity of the gel preparation method and identified the reaction products formed with other materials during heating.
- Many features of the differential scanning calorimetry results of the gel-derived materials can be correlated to changes observed in the dielectric loss factors.
- Under all of the processing conditions investigated, the nickel aluminate spinel formed was eight to ten microns thick. When the nickel oxide/spinel interface was poorly formed, the specimen failed at the interface. Specimens failed through the bulk of the nickel oxide when the nickel oxide/ spinel interface was of better quality.
- A nickel oxide interlayer thickness of 15-20 μm is necessary for complete reaction of the interlayer to occur under the conditions evaluated in this work.
- Specimens joined using AD94 alumina as the interface material separated at the interlayer/end member interface. Only a few of the fracture surfaces examined contained markings such as fracture origin, mirror planes and hackle.
- In the specimens joined with an AD94 interlayer, the interface between the interlayer and the end member was composed of grain boundary material from the lower purity interlayer that had been forced out during joining.

- Some of the bars joined using AD94 as the interlayer failed in the bulk of the end member, away from the joint interface. This suggests that the joints had strengths comparable to the as-received material.
- The uniformity of joints within a specimen were evaluated by position based on flexure strength. Bar positions were monitored to determine if volumetric microwave heating contributed to the flexure strength of joined specimens.
- Statistical tools were used to qualitatively assess the joining parameters used in this study. For the five parameters investigated (time, temperature, pressure, interlayer material and heating method) only varying the interlayer material provided a statistically significant difference at the 95% confidence level in the mean flexure strength. A significant difference was noted between heating methods at the 90% confidence level with the microwave processed specimens having the higher flexure strengths.
- Temperature profile simulations were generated for several different joining conditions.
- Temperature profiles that were measured experimentally or generated numerically were analogous.
- Thicker interlayers of nickel oxide (five millimeters) generated higher temperatures numerically. However, the strength of a specimen joined with such an interlayer would be insufficient for most structural ceramic applications.

In conclusion, microwave joining can play an important role in the advancement of the use of microwave processing in industry. Even materials systems that do not demonstrate enhancements in measured properties due to interactions with a microwave field can benefit from microwave processing. The most significant findings are listed below:

- High-purity alumina specimens were joined using microwave energy with flexure

strengths approaching that of the original material (86% strength of as-received alumina in trial #8). The significance of this is that complex products can be manufactured from simple shapes without seriously compromising the strength of the original material.

- A difference in the mean strength was observed between bars from the center of the specimen was observed. This difference did not prove to be statistically significant at the 95% confidence level. However, the number of bars sampled at this position are insufficient to support a statistical conclusion.
- The addition of a 500 μm thick interlayer of a strong microwave absorber did not provide an increase in temperature in either the experimental or numerical temperature profiles. When the thickness of the interlayer was changed to 5 mm, however, a dramatic increase in the numerically generated temperature profile was observed. Microwave absorption by the interlayer material can result in higher temperatures in the joint region than in the end member material. This can reduce the temperature-related negative effects (such as secondary grain growth and creep) that can lead to unpredicted failure of the joined specimen.
- The majority of the heat in the end members was generated by the microwave susceptor and transferred to the specimens via radiation and convection. The low dielectric loss of the AD995 alumina precluded significant absorption of microwave energy in the end members. The minimal interaction of microwaves with high-purity alumina facilitates the maintenance of sub-joining temperatures in the end members (a short distance from the interface). The temperatures necessary for joining then can be limited to joint area through the use of a strong microwave absorbing interlayer material. This is yet another method of reducing the negative effects of the high temperatures associated with joining.
- Satisfactory joints could be produced from as-machined surfaces with a roughness

in the range of 1.0 μm to 3.0 μm . Thus, the mirror finish of the surface recommended in many joining experiments may not be necessary to achieve adequate results. This has the potential to reduce machining costs of ceramic products that contain a joining step in their manufacture.

CHAPTER 8

FUTURE WORK

Although this study resulted in many important findings, the topic of microwave joining of ceramics has not been exhausted. The microwave joining apparatus developed in the course of this research has the potential to open the door to many applications for multimode microwave ovens. Some issues that could provide interesting topics of research for future investigations are:

- Use the numerical model developed in this study to investigate systems prior to laboratory experimentation. Simulation results should not be used to eliminate potential materials systems but to assist the user in developing a heating configuration more conducive to microwave processing. The model also could be used to determine the minimum amount ofsuscepting material necessary to achieve the desired processing temperatures. Optimizing the susceptor will allow microwave interaction with the workpiece to be maximized.
- The numerical model also can be helpful in the identification of potential opportunities for microwave processing. By simulating the heating conditions to be used, there is the capability of avoiding potential experimental pitfalls such as thermal runaway or non-uniform temperature distributions.
- Employ the microwave joining apparatus to investigate a materials system that is significantly influenced by microwave radiation. In laboratory scale experiments, the penetration depth of extremely low dielectric loss factor materials is too large to contribute notable power generation in the material. In future microwave joiningexperiments, materials such as zirconia, silicon carbide and alumina (with at

least 6% impurities) can provide a system that is more interactive with microwaves than 99.5% pure alumina.

- Investigate both strong and weak microwave absorbers as die materials for the utilization of the equipment developed as a microwave hot press for the pressure sintering of powders. A strong microwave absorber and a strong material such as silicon carbide can provide a setting similar to the radio frequency induction furnaces that use graphite dies. In this situation, poor microwave absorbing materials could be pressure sintered. If, on the other hand the material to be pressure sintered has a high dielectric loss, a microwave transparent structural ceramic like the AD995 alumina in this study could be used as the die material.
- Use high strength, low dielectric loss, high-purity alumina as a die material for performing self propagating high temperature synthesis of materials under an applied pressure. The benefits of microwave ignited combustion synthesis has been demonstrated¹⁰¹. By performing the synthesis under an applied pressure, there is the potential for increasing the density of the combusted products.

APPENDIX A

SAMPLE CALCULATIONS OF THE PENETRATION DEPTH AND CRITICAL THICKNESS FOR AI-66 CEMENT

Penetration depth at 25°C for AI-66 cement:

From equation 2-4,

$$D_p = \frac{\lambda_o'(\epsilon')^{\frac{1}{4}}}{2\pi\epsilon''}$$

Dielectric Properties of AI-66 Cement

Temperature (°C)	dielectric constant (ϵ')	effective loss factor (ϵ'')
25	4.34	0.032
1000	4.82	0.151

the wavelength of free space, λ_o' , is assumed to be that of the incident microwave, 2.45 GHz.

$$c = \lambda f$$

where

c = the speed of light, 2.998×10^{10} cm/s

f = frequency of microwaves, 2.45×10^9 s⁻¹

λ = wavelength = 12.24 cm.

at 1000°C,

$$D_p = \frac{(12.24 \text{ cm})(4.82)^{\frac{1}{4}}}{(2)(\pi)(0.151)} = 28.32 \text{ cm.}$$

Critical thickness at 1000°C for Al-66 cement

To calculate the critical thickness, L_{crit} , recall equation 2-9,

$$L_{crit} = 2.7\beta^{-1} - 0.08$$

where β is the penetration depth.

$$L_{crit} = 2.7 \times (28.32)^{-1} - 0.08 = 0.0153 \text{ cm}$$

APPENDIX B

SUMMARY OF INPUT DATA FOR HEATING 7.2

XGRID

RG (1) Smallest x or r gross grid line	RG (1) Next larger x or r gross grid line	RG (1) Next larger x or r gross grid line	RG (N) Largest x or r gross grid line	X1
RG (1) Number of divisions between first and second gross grid lines.	RG (2) Number of divisions between first and second gross grid lines.	RG (3) Number of divisions between first and second gross grid lines.	RG (N) Number of divisions between gross grid lines n-1 and n.	X2

YGRID

TRG (1) Smallest y or r gross grid line	TRG (1) Next larger y or r gross grid line	TRG (1) Next larger y or r gross grid line	TRG (N) Largest y or r gross grid line	Y1
TRG (1) Number of divisions between first and second gross grid lines.	TRG (2) Number of divisions between first and second gross grid lines.	TRG (3) Number of divisions between first and second gross grid lines.	TRG (N) Number of divisions between gross grid lines n-1 and n.	Y2

ZGRID

ZG (1) Smallest z or r gross grid line	ZG (1) Next larger z or r gross grid line	ZG (1) Next larger z or r gross grid line	ZG (N) Largest z or r gross grid line	Z1
ZG (1) Number of divisions between first and second gross grid lines.	ZG (2) Number of divisions between first and second gross grid lines.	ZG (3) Number of divisions between first and second gross grid lines.	ZG (N) Number of divisions between gross grid lines n-1 and n.	Z2

ANALYTICAL FUNCTIONS

ANALYT Analytical function number							A1
ANALYT Coefficient index, I	ANALYT Coefficient value, A _I	ANALYT Coefficient index, I	ANALYT Coefficient value, A _I	***	***	***	A2

NOTE: Entries on A2 Card define an analytical function of the following form. Only those terms having non-zero values need to be entered.

$$F(V) = A_1 + A_2V + A_3V^2 + A_4\cos(A_5V) + A_6\sin(A_5V) + A_7\exp(A_8V) + A_8\ln(A_9V)$$

TABULAR FUNCTIONS

TABUL Tabular function number							T1
ARG (1) First independent value	VAL (1) First dependent value	ARG (2) Second independent value	VAL (2) Second dependent value	***	***	***	T2

PRINTOUT TIMES

PRTIME (1) First period time	PRTIME (2) Second period time	PRTIME (3) Third period time	PRTIME (4) Fourth period time	***			Q
---------------------------------	-------------------------------------	---------------------------------	----------------------------------	-----	--	--	---

NODES MONITORED

NTS Number of sensors for which data is monitored between output	NDS (1) First node monitored	NDS (2) Second node monitored					S
--	------------------------------------	-------------------------------------	--	--	--	--	---

APPENDIX C

SAMPLE CALCULATIONS FOR STATISTICAL ANALYSIS

For a half-factorial experimental design it is possible to evaluate five factors in sixteen observations. The letters A, B, C, D, and E represent five variables than can be adjusted during some manufacturing process or treatment such as temperature, amount of mixing, purity of material or some other parameter. Each of these variables can be investigated at two different levels designated as low (-) and high (+). After the trials have been performed the resulting sixteen observations are tabulated.

Trial/effect	A	B	C	D	E	observation
1	+	+	-	+	+	166
2	+	+	-	+	+	166
3	+	+	-	+	+	197
3	+	+	-	+	+	201
5	+	+	-	+	+	166
6	+	+	+	+	+	166
7	+	+	-	+	+	215
8	+	+	-	+	+	229
9	+	+	-	+	+	205
10	+	+	-	+	+	184
11	-	+	-	+	-	168
12	+	+	-	+	+	172
13	-	-	+	+	-	210
14	+	-	+	+	+	219
15	-	+	+	+	+	252
16	+	+	+	+	-	200

To begin the analysis, the sum of the observations are taken two at a time and placed in a third column. This fills one-half of the new column. The second half of the column is filled by the difference of the observations taken two at a time. This method, developed by Yates¹²¹, is a more organized approach to the bookkeeping involved in determining the mean effect and the sum of squares of the observations. This method provides the same results as if the observations were added and subtracted in the standard order set out by the signs in the table above. The table then looks like

trial	observation	(1)
1	155	$155 + 184 = 339$
2	184	$197 + 201 = 398$
3	197	$166 + 156 = 322$
4	201	$215 + 229 = 444$
5	166	$205 + 184 = 389$
6	156	$168 + 172 = 340$
7	215	$210 + 219 = 429$
8	229	$252 + 200 = 452$
9	205	$184 - 155 = 29$
10	184	$201 - 197 = 4$
11	168	$156 - 166 = -10$
12	172	$229 - 215 = 14$
13	210	$184 - 205 = -21$
14	219	$172 - 168 = 4$
15	252	$219 - 210 = 9$
16	200	$200 - 252 = -52$

This process of addition and subtraction is repeated in three more instances with the

finished table containing four columns of calculations in addition to the original observations. The mean square for each variable is calculated by dividing the square of column (4) by sixteen, the number of trials in the experiment.

trial	observation	(4)	(2)	(4)	(4)	mean square (4) ² /16
1 (-)	155	339	737	1503	3113	-
2 A	184	398	766	1610	-3	0.56
3 B	197	322	429	57	155	1501.56
4 C	201	444	881	-60	-57	203.06
5 D	184	398	33	181	181	2047.56
6 E	155	390	24	-26	-36	76.56
7 AB	215	429	-17	-21	135	1139.06
8 CE	229	452	-43	-36	-57	203.06
9 CD	205	29	59	29	107	715.56
10 DE	184	4	122	152	-117	855.56
11 AC	168	10	-49	-9	-207	2678.06
12 AD	172	14	23	-26	-15	14.06
13 AE	210	-21	-25	63	123	945.56
14 BC	219	4	4	72	-17	18.06
15 BD	252	9	25	29	9	5.06
16BE	200	-52	-61	-86	-115	826.56

The confidence values for an F-distribution for one degree of freedom are

probability point	for one degree of freedom
0.1	39.9
0.05	161
0.01	4052

The results indicate that observations A, AD, BC and BD have no significant effect on the process. Observation E is significant in the $5\% < P < 10\%$ confidence level. All other observations are significant in the $1\% < P < 5\%$ confidence interval. This includes second order interactions between two variables in the experimental design.

REFERENCES

1. Sutton, W.H., Am. Ceram. Soc. Bull., Vol. 68 [2], pp.376-386 (1989).
2. Bruce, R.W., in Microwave Processing of Materials, edited by W.H. Sutton, M.H. Brooks and I.J. Chabinsky (Mater. Res. Soc. Proc., Vol. 124, Pittsburgh, PA), pp. 3-15 (1988).
3. Meek, T.T. and Blake, R.D., U.S. Patent No. 4 529 857, July (1985).
4. Meek, T.T., J. Mat. Sci. Let., Vol. 6 pp. 638-640 (1987).
5. Metaxas, R.C. and Meredith, R.J., Industrial Microwave Heating, pp. 70-102 Peter Peregrinus Ltd., London (1983).
6. Fathi, Z., Ph.D. Dissertation, University of Florida, 59-110 (1993).
7. Hutcheon, R.M., DeJong, M.S., Adams, F.P., Hunt, L., Iglesias, F., Wood, G.W. and Parkinson, G., Electromagnetic Energy Reviews, Vol. 2 [4] part 2 pp. 46-50 (1989).
8. Hutcheon, R.M., DeJong, M.S., Adams, F.P., Lucuta, P.G., McGregor, J.E. and Bahen, L., in Microwave Processing of Materials III, (eds. R.L. Beatty, W.H. Sutton and M.F. Iskander) Proceeding of the Materials Research Society Symposium, Vol. 269, pp. 541-551 (1992).
9. Graziani, T., Baxter, D. and Nannetti, C.A., in Corrosion of Advanced Ceramics, (eds. R.J. Fordham, D.J. Baxter and T. Graziani) Proceedings of a Special Session as Part of the 4th European Ceramics Society Conference, Vol. 113pp. 153-164 (1996).
10. Cathey, Jr., W.T., IEEE Trans. on Elec. Comp., Vol. EMC-25 [3] pp. 339-345 (1983).
11. Katz, J.D. and Blake, R.D., Am. Ceram. Soc. Bull., Vol. 70 [8] pp. 1304-1308 (1991).
12. Holcombe, C.E., Am. Ceram. Soc. Bull., Vol. 62 [12] pp. 1388-1345 (1983).
13. Tian, Y.L., Brodwin, M.E. Dewan, H.S. and Johnson, D.L., in Microwave Processing of Materials, (eds. W.H. Sutton, M.H. Brooks and I.J. Chabinsky) Proceeding of the Materials Research Society Symposium, Vol. 124, pp. 213-218 (1988).
14. Katz, J.D., Blake, R.D. and Scherer, C.P., Ceram. Eng. Sci. Proc., Vol. 10 [7-8]

- pp. 857-867 (1989).
15. Dé, A., Masters Thesis, University of Florida, (1990).
 16. Moore, E.H., Clark, D.E and Hutcheon, R., in Microwaves: Theory and Application in Materials Processing II, (eds. D.E. Clark, W.R. Tinga and J.R. Laia Jr.) Ceramic Transactions Vol. 36, pp. 325-333 ACerS, Westerville (1993).
 17. Janney, M.A., Kimrey, H.D. and Kiggans, J.O., in Microwave Processing of Materials III, (eds. R.L. Beatty, W.H. Sutton and M.F. Iskander) Proceeding of the Materials Research Society Symposium, Vol. 269, pp. 173-185 (1992).
 18. Stein, D.F., Edgar, R.H., Iskander, M.F., Johnson, D.L., Johnson, S.M., Lob, C.G., Shaw, J.M., Sutton, W.H., Tien, P.K. and Munns, T.E., in Microwave Processing of Materials IV, (eds. M.F. Iskander, R.J. Lauf and W.H. Sutton) Proceeding of the Materials Research Society Symposium, Vol. 347, pp. 3-7 (1994).
 19. Krieger, B., in Microwave Processing of Materials IV, (eds. M.F. Iskander, R.J. Lauf and W.H. Sutton) Proceeding of the Materials Research Society Symposium, Vol. 347, pp. 57-69 (1994).
 20. Decareau, R.V., Microwaves in the Food Processing Industry, Academic Press, Orlando (1985).
 21. Yee, K.S., IEEE Trans. Antennas Propagation, Vol. AP-14, pp. 302-307 (1966).
 22. Richmond, J.H., IEEE Trans. On Antennas and Propagation, Vol. AP-13, pp. 334-341 (1965).
 23. Taflove, A. and Brodwin, M.E., IEEE Trans. On Microwave Theory and Techniques, Vol. MTT-23 [8] pp. 623-630 (1975).
 24. Hirsch, F.G. And Parker, J.T., Am. Med. Assoc. Arch. Ind. Hyg., Vol. 6 pp. 512-517 (1952).
 25. Taflove, A. and Brodwin, M.E., IEEE Trans. On Microwave Theory and Techniques, Vol. MTT-23 [11] pp. 888-896 (1975).
 26. Young, L.A. And Boehm, R.F., J. Biomechanical Engineering, Vol. 115 pp. 441-446 (1993).
 27. Datta, A.K., Chem. Eng. Progress, V.86 [6] pp. 47-53 (1990).
 28. Tong, C.H. and Lund, D.B., J. Food Engineering, Vol. 19 pp. 319-339 (1993).
 29. Pangrle, B.J., Ayappa, K.G., Davis, H.T., Davis, E.A. And Gordon, J., AIChE Journal, Vol. 37 [12] pp. 1789-1800 (1991).
 30. Pangrle, B.J., Ayappa, K.G., Sutanto, E., Davis, H.T., Davis, E.A. And Gordon, J., Chem. Eng. Comm., Vol. 112 pp. 39-53 (1992).

31. Ayappa, K.G., Davis, H.T., Davis, E.A. and Gordon, J., AIChE Journal, Vol. 37 [3] pp. 313-322 (1991).
32. Ayappa, K.G., Davis, H.T., Davis, E.A. and Gordon, J., AIChE Journal, Vol. 38 [10] pp. 1577-1592 (1992).
33. Watters, D.G., Brodwin, M.E. and Kriegsmann, G.A., in Microwave Processing of Materials, (eds. W.H. Sutton, M.H. Brooks and I.J. Chabinsky) Mat. Res. Symp. Proc., Vol. 124 pp. 129-134 Materials Research Society, Pittsburgh (1988).
34. Gupta, D. and Evans, J.W., J. Mater. Res., Vol. 6 [4] pp. 810-818 (1991).
35. Iskander, M.F., in Microwave Processing of Materials II, (eds. W.H. Sutton, M.H. Brooks and I.J. Chabinsky) Proceeding of the Materials Research Society Symposium, Vol. 189, pp. 149-171 (1991).
36. Gupta, D. and Evans, J.W., J. Am. Ceram. Soc., Vol. 76 [8] pp. 1915-1923 (1993).
37. Li, W., Ebadian, M.A., White, T.L., Grubb, R.G. and Foster, D., Int. J. Heat Mass Transfer, Vol. 37 [6] pp. 1013-1027 (1994).
38. Ferber, M.K., Kimrey, H.D. and Becher, P.F., Report # ORNL/TM-8718 (1983).
39. Booty, M.R. and Kriegsmann, G.A., Methods and Applications of Analysis, Vol. 1 [4] pp. 403-414 (1994).
40. Dibben, D.C., Wai, B.F. and Metaxas, R.A.C., in Microwave Processing of Materials IV, (eds. M.F. Iskander, R.J. Lauf and W.H. Sutton) Proceeding of the Materials Research Society Symposium, Vol. 347, pp. 305-310 (1994).
41. Tucker, J., Iskander, M.F. and Huang, Z., in Microwave Processing of Materials IV, (eds. M.F. Iskander, R.J. Lauf and W.H. Sutton) Proceeding of the Materials Research Society Symposium, Vol. 347, pp. 353-356 (1994).
42. Skamser, D.J. and Johnson, D.L., in Microwave Processing of Materials IV, (eds. M.F. Iskander, R.J. Lauf and W.H. Sutton) Proceeding of the Materials Research Society Symposium, Vol. 347, pp. 325-330 (1994).
43. Thomas, J.R., Katz, J.D. and Blake, R.D. in Microwave Processing of Materials IV, (eds. M.F. Iskander, R.J. Lauf and W.H. Sutton) Proceeding of the Materials Research Society Symposium, Vol. 347, pp. 311-316 (1994).
44. Kriegsmann, G.A., J. Appl. Phys., Vol. 71 [4] pp. 1960-1966 (1992).
45. Kriegsmann, G. A., in Microwave Processing of Materials IV, (eds. M.F. Iskander, R.J. Lauf and W.H. Sutton) Proceeding of the Materials Research Society Symposium, Vol. 347, pp. 473-478 (1994).

46. Spotz, M.S., Skamser, D.J. and Johnson, D.L., J. Am. Ceram. Soc., Vol. 78 [4] pp. 1041-1048 (1995).
47. Beale, G.O. and Arteaga, F.J., in Microwave Processing of Materials III, (eds. R.L. Beatty, W.H. Sutton and M.F. Iskander) Proceeding of the Materials Research Society Symposium, Vol. 269, pp. 265-270 (1992).
48. Ayappa, K.G., Davis, H.T., Crapiste, G., Davis, E.A. And Gordon, J., Chem. Eng. Sci., Vol. 46 [4] pp. 1005-1016 (1991).
49. Janney, M.A. and Kimrey, H.D., in Microwave Processing of Materials II, (eds. W.H. Sutton, M.H. Brooks and I.J. Chabinsky) Proceeding of the Materials Research Society Symposium, Vol. 189, pp. 215-227 (1991).
50. Fathi, Z., Clark, D.E. and Hutcheon, R.H., in Microwave Processing of Materials III, (eds. R.L. Beatty, W.H. Sutton and M.F. Iskander) Proceeding of the Materials Research Society Symposium, Vol. 269, pp. 347-352 (1992).
51. Ahmad, I., Ph.D. Dissertation, University of Florida (1992).
52. Fathi, Z., Clark, D.E. and Ahmad, I., Ceram. Eng. Sci. Proc., Vol. 14 [9-10] pp. 863-870 (1993).
53. Tiegs, T.N., Kiggans, J.O. and Kimrey, H.D., Ceram. Eng. Sci. Proc., Vol. 12 [9-10] pp. 1981-1992 (1991).
54. Ferber, M.K., Tiegs, T.N. and Jenkins, M.G., Ceram. Eng. Sci. Proc., Vol. 12 [9-10] pp. 1993-2004 (1991).
55. Schwartz, M. M., Composite Materials Handbook, 7.50-7.109 McGraw-Hill, Inc., New York (1992).
56. Kimura, O. and Kawashima, T., J. Appl. Mech., Vol. 56 pp. 707-710 (1989).
57. Kimura, O., J. Am. Ceram. Soc., Vol. 76 [3] 757-759 (1993).
58. Santella, M. L., Am. Ceram. Soc. Bull., Vol. 71 [6] pp. 947-954 (1992).
59. Henricke, H.W., High Tech Ceramics, 805-814 (1987).
60. Loehman, R. E. and Tomsia, A. P., Am. Ceram. Soc. Bull., 67, [2] 375-380 (1988).
61. Derby, B., in Joining of Ceramics, (ed. M.G. Nicholas) Chapman and Hall, London pp. 94-112 (1990).
62. Derby, B. and Wallach, E.R., Metal Science, 16, 49-56 (1982).
63. Smith, M. A. and Pope, D. P., Mat. Sci. and Eng., Vol. A145 pp. 79-86 (1991).
64. Villagio, P., J. Applied Mechanics, 56, 590-594 (1989).

65. Suganama, K., Okamoto, T., Koizumi, M. And Shimada, M., Adv. Ceram. Mater., Vol. 1 pp. 356 (1986).
66. Akselson, O.M., Journal Mat. Sci., Vol. 27 [3] pp. 569-578 (1992).
67. Nicholas, M. G., and Crispin, R. M, J. Mater. Sci., Vol. 17 pp 3347-3360 (1982).
68. Allen, R. V. and Borbidge, W. E., J. Mater. Sci., vol. 18 pp. 2835-2842 (1983).
69. Calow, C. A., Bayer, P. D. and Porter, I. T., J. Mater. Sci., Vol. 6 pp. 150-155 (1971).
70. Kingery, W. D., Bowen, H. K. and Uhlmann, D. R., Introduction to Ceramics, pp. 38-46 John Wiley & Sons, New York (1976).
71. Ferrante, J., Bozzolo, G. H., Finley, C. W. and Banerjee, A., Adhesion in Solids, Materials Research Society Symposium Proceedings (eds. Mattox, D. M., Baglin, J. E. E., Gottschall, R. J. and Battich, C. D.), Vol. 119 pp. 3-16 Materials Research Society, Pittsburgh, (1988).
72. Clarke, D. R. and Wolf, D., Mater. Sci. Eng., Vol. 83 pp. 197-204 (1986).
73. Stoneham, A. M. and Tasker, P. W., in Ceramic Microstructures '86: Role of Interfaces, Materials Science Research (eds. Pask, J. A. and Evans, A. G.), Vol. 21 pp. 155-164 Plenum Press, New York (1986).
74. Binner, J. P. G., Davis, P. A., Cross, T. E. and Fernie, J. A., in Microwaves: Theory and Application in Materials Processing III, (eds. D.E. Clark, D.C. Folz, S.J. Odato and J.R. Laia Jr.) Ceramic Transactions Vol. 59 pp. 335-346 ACerS, Westerville, (1995).
75. Al-Assafi, S., Masters Thesis, University of Florida, (1992).
76. Fathi, Z., Cozzi, A. D. and Clark, D. E., Ceram. Eng. Sci. Proc., Proceedings of the 16th Annual Conference on Composites and Advanced Ceramic Materials, Vol. 13 [7-8] pp. 1066-1072 (1992).
77. Xian, A-P. and Si, Z-Y., J. Am. Ceram. Soc., Vol. 73 [11] pp. 3462-3465 (1990).
78. Amide, T., Satoh, M., Kohno, A. and Yokoi, K., J. Mater. Sci., Vol. 26 [10] pp. 2887-2892 (1991).
79. Nicholas, M.G. and Crispin, R.M., Proc. Brit. Ceram. Soc., Vol. 32 pp. 33-40 (1982).
80. Suga, T., Miyazawa, K. and Yamagata, Y., MRS Int. Med. Adv. Mats., Vol. 8 pp. 257 (1989).

81. Ishida, Y., Wang, J. and Suga, T., Acta Metall. Mater., Vol. 40 pp. S289-S293 (1992).
82. Serier, B. and Treheux, D., Acta Metall. Mater., Vol. 41 [2] pp. 369-374 (1993).
83. Hauth III, W.H., Am. Ceram. Soc. Bull., Vol. 58 [6] pp. 584-586 (1979).
84. Scott, C.E. and Brewer, J.A., J. Am. Ceram. Soc., Vol. 69 [8] pp. C-178 - C-179 (1986).
85. Scott, C. and Tran, V.B., Am. Ceram. Soc. Bull., Vol. 64 [8] pp. 1129-1131 (1985).
86. Zdaniewski, W.A. and Kirchner, H.P., J. Am. Ceram. Soc., Vol. 70 [1] pp. C-4-C-6 (1987).
87. DeLeeuw, D., J. Am. Ceram. Soc., Vol. 75 [3] pp. 725-727 (1992).
88. Kaba, T., Shimada, M. and Koizumi, M., J. Am. Ceram. Soc., Vol. 66 [8] pp. C-135-C-136 (1983).
89. Zimmer, C.E., Mechanical Engineering, Vol. 7 pp. 34-37 (1984).
90. Zdaniewski, W.A., Shah, P.M. and Kirchner, H.P., Adv. Ceram. Mat., Vol. 2 [3a] pp. 204-208 (1987).
91. Becher, P.F. and Halen, S.A., Am. Ceram. Soc. Bull., Vol. 58 [6] pp. 582-583 (1979).
92. Mecartney, M.L., Sinclair, R. and Loehman, R.E., J. Am. Ceram. Soc., Vol. 68 [9] pp. 472-478 (1985).
93. Johnson, S.M. and Rowcliffe, D.J., J. Am. Ceram. Soc., Vol. 68 [9] pp. 468-472 (1985).
94. Palaith, D., Silbergliitt, R., Wu, C.C.M., Kleiner, R. and Libelo, E.L., in Microwave Processing of Materials, (eds. W.H. Sutton, M.H. Brooks and I.J. Chabinsky) Mat. Res. Symp. Proc., Vol. 124 pp. 255-266 Materials Research Society, Pittsburgh (1988).
95. Fukushima, H., Yamanaka, T. and Matsui, M., in Microwave Processing of Materials, (eds. W.H. Sutton, M.H. Brooks and I.J. Chabinsky) Mat. Res. Symp. Proc., Vol. 124 pp. 267-272 Materials Research Society, Pittsburgh (1988).
96. Al-Assafi, S. and Clark, D. E., Ceram. Eng. Sci. Proc., Proceedings of the 16th Annual Conference on Composites and Advanced Ceramic Materials, Vol. 13 [7-8] pp. 1073-1080 (1992).
97. Palaith, D. and Silbergliitt, R., Am. Ceram. Soc. Bull., Vol. 68, [9] pp. 1601-1606 (1989).

98. Yu, X.D. Varadan, V.V. and Varadan, V.K., in Microwaves: Theory and Application in Materials Processing, (eds. D.E. Clark, F.D. Gac and W.H. Sutton) Ceramic Transactions Vol. 21, pp. 497-505 ACerS, Westerville (1991).
99. Ahmad, I., Silbergliitt, R., Black, R.M., Sa'Adaldin, S. and Katz, J.D., in Microwave Processing of Materials III, (eds. R. L. Beatty, W.H. Sutton, M.F. Iskander) Mat. Res. Symp. Proc., Vol. 269 pp. 271-276 Materials Research Society, Pittsburgh (1992).
100. Yin, T.Y., Varadan, V.V., Varadan, V.K. and Conway, J.C., in Microwaves: Theory and Application in Materials Processing, (eds. D.E. Clark, F.D. Gac and W.H. Sutton) Ceramic Transactions Vol. 21, pp. 507-514 ACerS, Westerville (1991).
101. Dalton, R.C., Ahmad, I. and Clark, D.E., Ceram. Eng. Sci. Proc., Vol. 11 [9-10], pp. 1729-1742 (1990).
102. Silbergliitt, R., Palaith, D., Black, R.M., Sa'Adaldin, H.S., Katz, J.D. and Blake, R.D., in Microwaves: Theory and Application in Materials Processing, (eds. D.E. Clark, F.D. Gac and W.H. Sutton) Ceramic Transactions Vol. 21, pp. 487-495 ACerS, Westerville (1991).
103. Loehman, R.E., in Microwaves: Theory and Application in Materials Processing II, (eds. D.E. Clark, W.R. Tinga and J.R. Laia Jr.) Ceramic Transactions Vol. 36, pp. 417-430 ACerS, Westerville (1993).
104. Das, S. and Curlee, T.R., Am. Ceram. Soc. Bull., Vol. 66 [7] pp. 1093-1094 (1987).
105. Sheppard, L.M., Am. Ceram. Soc. Bull., Vol. 67 [10] pp. 1656- 1661 (1987).
106. Katz, J.D., in Annu. Rev. Mater. Sci., (eds. R.A. Huggins, J.A. Giordmaine and J.B. Watchman, JR.) Vol. 22 pp. 153-170 Annual Review Inc. Palo Alto (1992).
107. Schulz, R.L., Folz, D.C., Clark, D.E., Schmidt, C.J. And Wicks, G.G., in Microwaves: Theory and Application in Materials Processing III, (eds. D.E. Clark, D.C. Folz, S.J. Oda and J.R. Laia Jr.) Ceramic Transactions Vol. 59 pp. 107-114 ACerS, Westerville (1995).
108. Schiffmann, R.F., in Microwaves: Theory and Application in Materials Processing, (eds. D.E. Clark, D.C. Folz, S.J. Oda and R. Silbergliitt) Ceramic Transactions Vol. 59, pp. 7-16 ACerS, Westerville, (1995).
109. Clark, D.E. Dalzell, W. J. and Adams, B. L., U.S. Patent Number 4,801,399, (1989).
110. Dalzell, W. J., Masters Thesis University of Florida, (1988).
111. McGill, S.L., Walkiewicz, J. and Smyres, G.A., in Microwave Processing of Materials, (eds. W.H. Sutton, M.H. Brooks and I.J. Chabinsky) Mat. Res. Symp. Proc., Vol. 11 pp. 247-252 Materials Research Society, Pittsburgh (1988).

112. Bunting, E.N., Bur. Standards J. Research, Vol. 6 [6] p. 948 (1931).
113. Muan, A., Amer. J. Sci., Vol 256 p. 420 (1958).
114. Dé, A., Masters Thesis, University of Florida, (1990).
115. Davies, O.L., The Design and Analysis of Industrial Experiments, pp. 440-494 Longman Inc., New York (1978).
116. Gitzen, W.H., Alumina as a Ceramic Material, pp. 63-97 American Ceramic Society, Columbus (1970).
117. Furukawa, G.T., Douglas, T.B., McCoskey, R.E. and Ginnings, D.C., Res. Natl. Bur. Stds., Vol. 57 [2] pp. 67-82 (1956).
118. Miyayama, M., Koumoto, K. and Yanagida, H., in Engineered Materials Handbook Volume 4 Ceramics and Glasses, pp. 748-749 ASM International, USA (1991).
119. Batelle Memorial Institute, Engineering Properties of Selected Ceramic Materials, 5.2 3-2 The American Ceramic Society, Columbus, (1966).
120. Fischer, W.A. and Hoffman, A., Arch. Eisenhüttenw., Vol 27 [5] p. 344 (1956).
121. Yates, F., Design and Analysis of Factorial Experiments, Imperial Bureau of Soil Science, London (1937).

BIOGRAPHICAL SKETCH

Alex Cozzi was born May 22, 1963 in Nyack, New York. He attended the New York State College of Ceramics at Alfred University in Alfred, New York. In May of 1985 he received his bachelor's degree in ceramic engineering. In May of 1986 he accepted a position as a laboratory engineer at American Marazzi Tile, Inc. in Sunnyvale, Texas. Cozzi enrolled in the graduate program in the Department of Materials Science and Engineering at the University of Florida in 1988. He earned his M.S. degree in materials science and engineering in 1991. He is a student member of the American Ceramic Society and the National Institute of Ceramic Engineers.

I certify that I have read this study and that in my opinion it conforms to acceptable standards of scholarly presentation and is fully adequate, in scope and quality, as a dissertation for the degree of Doctor of Philosophy.



David E. Clark, Chairman
Professor of Materials Science
and Engineering

I certify that I have read this study and that in my opinion it conforms to acceptable standards of scholarly presentation and is fully adequate, in scope and quality, as a dissertation for the degree of Doctor of Philosophy.



E. Dow Whitney
Professor of Materials Science
and Engineering

I certify that I have read this study and that in my opinion it conforms to acceptable standards of scholarly presentation and is fully adequate, in scope and quality, as a dissertation for the degree of Doctor of Philosophy.



John J. Mecholsky
Professor of Materials Science
and Engineering

I certify that I have read this study and that in my opinion it conforms to acceptable standards of scholarly presentation and is fully adequate, in scope and quality, as a dissertation for the degree of Doctor of Philosophy.



Rajiv K. Singh
Associate Professor of Materials
Science and Engineering

I certify that I have read this study and that in my opinion it conforms to acceptable standards of scholarly presentation and is fully adequate, in scope and quality, as a dissertation for the degree of Doctor of Philosophy.



Bhavani V. Sankar
Professor of Aerospace Engineering,
Mechanics and Engineering Science

I certify that I have read this study and that in my opinion it conforms to acceptable standards of scholarly presentation and is fully adequate, in scope and quality, as a dissertation for the degree of Doctor of Philosophy.



Mattison K. Ferber
High Temperature Materials
Laboratory at Oak Ridge National
Laboratory, Senior Research Staff

This dissertation was submitted to the Graduate Faculty of the College of Engineering and to the Graduate School and was accepted as partial fulfillment of the requirements for the degree of Doctor of Philosophy.

August 1996



Winfred M. Phillips
Dean, College of Engineering

Dean, Graduate School

LD
1780
199**b**
.C8821

SCIENCE
LIBRARY

